Universitat Autònoma de Barcelona

Development of integrated plasmomechanical sensors in microfluidic devices for live cell analysis

Verónica Iraís Solís Tinoco

ADVERTIMENT. L'accés als continguts d'aquesta tesi queda condicionat a l'acceptació de les condicions d'ús establertes per la següent llicència Creative Commons: http://cat.creativecommons.org/?page_id=184

ADVERTENCIA. El acceso a los contenidos de esta tesis queda condicionado a la aceptación de las condiciones de uso establecidas por la siguiente licencia Creative Commons: http://es.creativecommons.org/blog/licencias/

WARNING. The access to the contents of this doctoral thesis it is limited to the acceptance of the use conditions set by the following Creative Commons license: https://creativecommons.org/licenses/?lang=en

Universitat Autònoma
de Barcelona

Doctorat en Enginyeria Electrònica
Departament D'Enginyeria Electrònica

Development of integrated plasmomechanical sensors in microfluidic devices for live cell analysis

Doctoral Thesis – 2016

Verónica Iraís Solís Tinoco
Author

Prof. Laura M. Lechuga
Director

Dr. Borja Sepúlveda
Director

David Jiménez Jiménez
Tutor

CSIC
Consejo Superior de Investigaciones Científicas

ICN2
Institut Català
de Nanociència
i Nanotecnologia

EXCELENCIA
SEVERO
OCHOA

To my parents,

Abstract

This doctoral Thesis focuses on the design, study, and optimization of the controlled fabrication metodology of a flexible plasmo-mechanical sensor with microfluidics, as well as its optical and mechanical characterization. We are interested in the use of this sensor to study cell traction forces for its essential role in cell functions (*e.g.*, adhesion, survival, migration, proliferation, and differentiation) and tissue development. Nowadays, the monitoring and quantification of those traction forces are one of the challenges faced by cell biology.

We take advantage of the use of polymeric materials, and low-cost and large-scale nanofabrication techniques to create the new prototype sensor. The sensor is formed by a hexagonal array of polymeric nanopillars capped with plasmonic gold nanodisks into a microfluidic channel. The main strategy for the fabrication of the sensor is based on replica molding techniques. The diameter, height, and separation of the nanopillars are designed in order to replicate the structures using polymers with different Young's modulus, and to control their mechanical flexibility.The plasmonic gold nanodisks are deposited on top of the nanopillars by controlled metal evaporation. Finally, the building of the integrated microfluidic sensor is based on a permanent bonding strategy. The transduction is based on combining the mechanical flexibility of the nanopillars with the optical properties of the gold nanodisks that exhibit localized surface plasmon resonances (LSPR).

The results suggest that the combination of the mechanical flexibility of the polymer nanopillars with the optical properties of the gold nanodisks allow the monitoring of refractive index changes in the environment. The mechanical properties (*e.g.*, spring constant) can be used to control the mechanical stability of the polymer structures, and also to mimic the mechanical properties of soft or rigid tissues. A preliminary analysis of cell culture onto the nanopillar array was carried out as a proof-of-concept to know the advantages and the limits of the new sensor design and the optical detection system. The results showed that the living cells could adhere and interact with the Au-capped nanopillars with different rigidity, inducing detectable LSPR changes.

The work in this Thesis represents a significant step towards the implementation of novel and more efficient sensors for the study of cell biology, which could play a key role in the understanding of essential biological processes.

Resumen

Esta Tesis doctoral se centra en el diseño, estudio y optimización de una metodología controlada para la fabricación de un sensor flexible y plasmo-mecánico integrado con microfluídica, así como en su caracterización óptica y mecánica. Estamos interesados en el uso de este sensor para estudiar las fuerzas de tracción de las células por su papel esencial en las funciones celulares (por ejemplo, adhesión, supervivencia, migración, proliferación y diferenciación) y en el desarrollo de tejidos. Hoy en día, la monitorización y cuantificación de las fuerzas de tracción son uno de los desafíos que enfrenta la biología celular.

Utilizamos las ventajas de los materiales poliméricos y las técnicas de nano-fabricación para crear un nuevo prototipo de sensor flexible de bajo coste y a gran escala. El sensor está formado por un arreglo hexagonal de nanopilares de polímero con nanodiscos plasmónicos de oro en su parte superior, ubicados dentro de un canal microfluídico. La fabricación del sensor se basa en las técnicas de réplica de estructuras. El diámetro, la altura y separación de los nanopilares están diseñados para ser copiados utilizando polímeros con un módulo de Young diferente, y de esta forma controlar su flexibilidad. Los discos plasmónicos de oro son depositados sobre los nanopilares utilizando evaporación de metales. Finalmente, la construcción del sensor integrado con microfluídica se basa en una estrategia de sellado permanente. La transducción utiliza la combinación de la flexibilidad mecánica de los nanopilares de polímeros con las propiedades ópticas de los nanodiscos de oro que presentan una resonancia de plasmón superficial localizada (LSPR).

Los resultados obtenidos en esta Tesis sugieren que la combinación de la flexibilidad mecánica de los nanopilares de polímero con las propiedades ópticas de los nanodiscos de oro, permiten la monitorización de los cambios del índice de refracción del medio exterior. Las propiedades mecánicas (por ejemplo, la constante elástica) pueden utilizarse para controlar la estabilidad mecánica de las estructuras de polímero y para imitar las propiedades mecánicas de tejidos blandos o duros. Se llevó a cabo un análisis preliminar de un cultivo celular sobre los nanopilares como una prueba de concepto, para conocer las ventajas y los límites del nuevo sensor diseñado y del sistema de detección óptica.

Los resultados mostraron que las células vivas pudieron adherirse e interactuar con los nanodiscos plasmónicos de los nanopilares con diferente rigidez, induciendo cambios detectables en el LSPR.

El trabajo en esta Tesis representa un paso significativo hacia la implementación de nuevos sensores más eficaces para ser empleados en estudios básicos de biología celular, que podrían desempeñar un papel importante en la comprensión de procesos biológicos esenciales.

Agradecimientos

Quiero extender un cordial agradecimiento al Consejo Nacional de Ciencia y Tecnología (CONACyT-México) por haber sustentado mis estudios de Doctorado durante este periodo.

Deseo agradecer a la líder del grupo, Prof. Laura M. Lechuga por su asesoría y conocimiento que fueron invaluables para realizar mis estudios. Por todos los momentos compartidos, por las oportunidades brindadas y por las enseñanzas recibidas. Gracias por dar mil batallas juntas.

También agradezco al Dr. Sepúlveda por el brillante ingenio y puesta en marcha del proyecto, por compartir sus puntos de vista y conocimientos, que me ayudaron a realizar este trabajo.

Extiendo las gracias al Senior Antoni Homs por su importante colaboración y apoyo invaluable en la parte científica de este trabajo, por sus brillantes y acertados consejos que fueron y serán parte importante de mi formación profesional. Gracias por la inspiración para dar lo mejor en todo.

Quiero dar las gracias a todas las personas con las que tuve la oportunidad de compartir momentos de alegrías y de tristeza, ustedes hicieron que mis estudios de Doctorado fueran una etapa inolvidable. Quiero agradecer con mucho amor.

A Dios, que en todo momento me ha ayudado y ha hecho posible que lo que para mí era imposible.

A mis padres, Fidel y Leticia, que me apoyaron en está loca idea de seguir estudiando. Guardo en mi corazón los consejos y ánimos que me brindaron para seguir trabajando cuando más difícil era el camino. Su confianza en mí, me dio la fuerza para continuar a pesar de todos los obstáculos innecesarios que se me presentaban. Gracias papá y mamá. Mis amados hermanos Blanca, Fidel, Víctor, Ericka y traviesas sobrinas, que fueron una motivación para continuar cuando más obscuro fue el camino. Gracias por sus ánimos, compresión de tiempos y distancia. Israel, eres la mejor prueba de que Dios me ama, mi ángel, mi amigo, mi amor. Gracias por tus innumerables formas de ayudarme, para adaptarme a tantos cambios y disfrutar lo bueno y malo de vida. Gracias por entender mi trabajo. Isabel y Clarita, mi familia catalana, inicio y final de mi estancia en Barcelona, les doy las gracias por las risas, los divertidos momentos que pasamos, y por quedarse conmigo todas esas madrugadas trabajando, las quiero mucho y siempre tendrán en mí a una amiga.

Me gustaría agradecer de todo corazón a mis amigos, temo que la palabra se queda corta para describir lo que les quiero decir.

Melissa, Adrián y Mane, su llegada a BCN fue una de las mejores etapas que viví en el doctorado, su compañía y amistad hizo que el tiempo pasará rápido. Raquel gracias por tus charlas y consejos, para mí eres un ejemplo de una mujer alegre y trabajadora. Juliane nos faltó tiempo para disfrutar de nuestra amistad, pero fue lo necesario para conocer la mujer valiente y amable que eres, te doy las gracias por alentarme a seguir trabajando, y a enfrentar los obstáculos que se me presentaron en esta etapa. Gerardo gracias por ser mi amigo y compañero, tu sinceridad y sensibilidad es de unos 50,0000 nm/RIU. Gracias por tu tiempo y apoyo en el trabajo. Nuria, aunque nos tratamos en la parte final, te doy las gracias por compartir tu alegría y buena vibra, llegar al trabajo y ver una sonrisa amable es algo que aprendí valorar en el grupo. Daniel B., aun a pesar de la distancia te doy las gracias por estar atento a mis estudios, por darme ánimos y consejos para seguir adelante con el proyecto. Karla, nuestra amistad nació rápidamente, gracias por tu ayuda y apoyo en todo momento. Tu confianza y honestidad te hace una de mis mejores amigas.

Karolina thanks for your hospitality and sincere friendship, you're a very strong woman. Thank you for sharing the good times, but specially for the confidence of sharing the difficult stages of life with me. I will always be your friend no matter the distance. Sam mi muy viejo amigo y compañero de aventuras, tus recuerdos serán siempre parte de mi vida. Gracias por enseñarme que un amigo no sabe de límites para cuidar y apoyar. Compartir esta etapa nos mejoró mucho como personas, los dos sabemos claramente lo que no queremos ser en la vida.

Mi querido amigo César, no sé cuándo nuestra amistad surgió, pero lo que sé, es que con ella nacieron momentos inolvidables que guardo como un tesoro. Gracias por las aventuras que compartimos dentro y sobre todo fuera del trabajo. Conocer tu cariño y apoyo hizo que mi Doctorado y vivir en España fueran de las mejores historias que tengo para contar en mi vida. Maria la Nostra, mi asesora de tesis, compañera de trabajo y amiga. Muchas gracias por ser la mujer que eres, los buenos y malos momentos que he hemos compartido han sido de los mejores recuerdos que tengo para explicar lo que es la amistad. Te quiero mucho y doy gracias a la vida y a Dios por haber tenido el placer de conocerte. Gracias por enseñarme lo que es la coca y el agua de valencia!

Finalmente, quiero agradecer a mis compañeros, Marcos, David fariña, Santos, Ana, Sofía, Sonia, Adrián, M. Carmen, Paty, Blanca, Cristina, Jesús y Daniel. El tiempo que compartimos me enseñó a respetar las diferentes formas de ver la vida. Les doy sinceramente las gracias.

Quien obra puede equivocarse, pero quien no hace nada ya está equivocado.

Santa Teresa de Ávila

Table of Contents

Publications and Conference contributions

[1]V. Solis-Tinoco, S. Marquez, B. Sepulveda, and L. M. Lechuga, “Fabrication of well-ordered silicon nanopillars embedded in a microchannel via metal-assisted chemical etching: a route towards an opto-mechanical biosensor,” RSC Adv., vol. 6, no. 88, pp. 85666–85674, Sep. 2016.

[2]V. Solis-Tinoco, B. Sepulveda, and L. M. Lechuga, “Novel nanoplasmonic biosensor integrated in a microfluidic channel,” presented at the Proc. SPIE, Nanotechnology VII, 2015, p. 95190T–95190T–9.

[3]M. A. Otte, V. Solis-Tinoco, P. Prieto, X. Borrisé, L. M. Lechuga, M. U. González, and B. Sepulveda, “Tailored Height Gradients in Vertical Nanowire Arrays via Mechanical and Electronic Modulation of Metal-Assisted Chemical Etching,” Small, p. n/a-n/a, May 2015.

[4]V. Solis-Tinoco, B. Sepúlveda, and L.M. Lechuga, “Fabricación de un Biosensor Nano-Optomecánico para el Estudio del Comportamiento Celular,” presented at the IV simposio de Becarios CONACyt en Europa, Parlamento Europeo Estrasburgo, Francia, 2014.

Patent

Title: Nanopillar matriz with height gradients,Inventors: Sepúlveda Mártinez Borja, Solís Tinoco Verónica Iraís, Otte Ortiz Marinus Albertus, Gonzales Maria Ujue,Publication No.: P201430684; ES1641.904,Country: Spain,Priority date: May 9th, 2014,Owners: CSIC

Motivation and Objectives

Nanotechnology has been performing an important role in the development of new sensor platforms. The use of nanomaterials and the ability to build structures with nano-scale dimensions has enhanced the sensitivity and performance of these devices. Notably, in cell biology sophisticated sensors are needed not only to emulate more complex, *in vivo* like extracellular matrix environments, but also to monitor and quantify dynamic complex biological processes. For example, cellular adhesion is a complex and fundamental process with crucial implications in biology, like the immune response, the tissue nature and architecture, or even the appearance and spreading of tumor cells. However, the detection and evaluation of the traction forces exerted by cells and transmitted to the underlying substrate through focal adhesions (FAs) remain a challenging problem due to the small areas where the cells attach (~µm^2), the density of those zones, and the range of magnitude of the forces (pN-nN scale). Therefore, the development of new sensor platforms satisfying those demanding requirements will be of paramount importance to evaluate the traction forces. Ideally these sensors should dectect directly the position and magnitude of FAs in real time avoiding any external modification. Also, these platforms should be small, portable, easy to use, inexpensive, disposable and compatible with other complementary technologies.

To overcome these challenges, in this Thesis we describe an approach, using low-cost and large-scale nanofabrication tools, of a novel plasmo-mechanical sensor, which could be attractive for the field of biology, to enable rapid analysis *in vitro*. We have designed and fabricated a sensor compatible with plasmonics and microfluidics technologies. The sensor transduction will be based on combining the mechanical flexibility of polymer nanopillars with the optical properties of the gold nanodisks that exhibit localized surface plasmon resonances (LSPR). The detection will be based on the refractive index sensing and near field interaction sensing using the LSPR of gold nanodisks supported on the flexible nanopillars.

From the abovementioned, with this work, we intend to contribute to the design, study, fabrication, characterization and application of the novel sensor. To this end, the main objectives outlined for the Thesis include:

1. The development and fabrication of a plasmomechanical sensor integrated with microfluidics technology.

2. To perform a sensitivity assessment of the plasmomechanical sensors via LSPR refractive index sensing to characterize their optical and mechanical properties, and to determine the real potential of these novel sensors.

3. To perform a preliminary proof-of-concept of the capabilities of the sensor for detecting traction forces of living cells.

Chapter 1. General Introduction

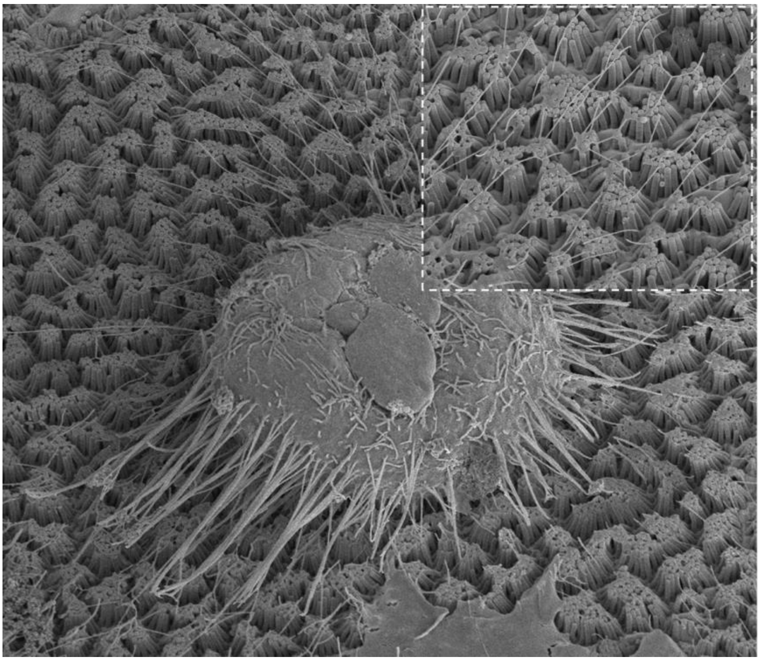

1.1 The cell: study and understanding

The cell is the elementary morphological and functional unit of all living organisms. The human body contains more than 10 trillion cells, either forming the tissues or circulating in the blood. In complex organisms, the cells adopt different morphologies and functions to meet the multiple needs required to live, grow, reproduce and even die. Over the years, researchers have been attracted to the study of the cell structure and composition, its basic functioning and the interactions between cells. The first observation of a cell is attributed to Robert Hooke in 1665 thanks to the invention of the microscope. Since then, cell biology and technology have been intimately related, as the development of more powerful and sophisticated instruments has allowed the deciphering of complex pathways and functions with a great detail. A better understanding of cell biology has motivated significant advances in disease diagnosis, the discovery of new drugs and therapies or the development of regenerative implants, among other examples. However, some cell functions, behaviors or processes are still a not completely resolved matter. The main limitations and challenges are related to the need of exploring the live cells either *in vivo* or in a biomimetic environment, avoiding any external modification while having a precision in the nanometer range.

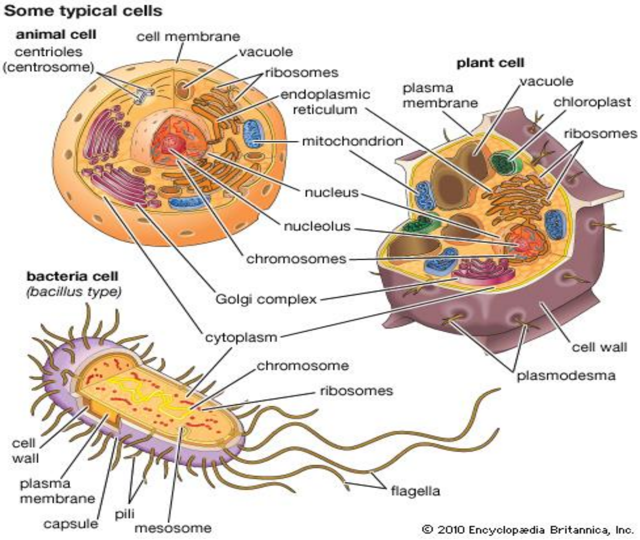

Figure 1.1. *Animal cells and plant cells contain membrane-bound organelles, including a distinct nucleus. In contrast, bacterial cells do not contain organelles. Encyclopædia Britannica, Inc.*

The cell is the smallest element that we consider alive, with dimensions ranging from 1 to 100 μm. It is primarily composed of the cell membrane and the cytoplasm, which contains biomolecules such as proteins or DNA, or more complex organelles. Based on their internal organization, the cells can be divided into two main types: prokaryotes and eukaryotes (see Fig. 1.1). Prokaryotes are small in size (1–10 μm) and simple in structure. The intracellular components (proteins, DNA, and metabolites) are directly placed in the cytoplasm, lacking membrane-bound compartments. Perhaps the most well-known prokaryote is the bacterium. Eukaryotes are larger than prokaryotes and more complex in structure and functioning. Animals, plants, and fungi are eukaryotic organisms. Internally, the eukaryotic cell is organized into various compartments or organelles enclosed by their membranes, and a cytoskeleton that defines their structure and morphology. Each organelle has a function, such as the storage of genetic information (nucleus), protein synthesis (ribosomes and Golgi apparatus) or energy production (mitochondria), among others. The cytoskeleton is mainly composed of protein filaments and microtubules that serve as a cellular scaffold, defining its shape and movements.

Externally, both prokaryotes and eukaryotes have a plasma membrane that encloses the

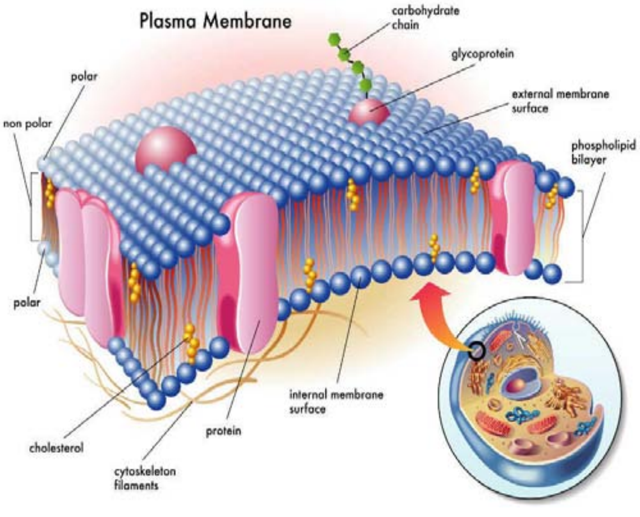

Figure 1.2. *Molecular view of the Plasma membrane. Plasma membrane can be defined as a biological membrane or an outer membrane of a cell, which is composed of two layers of phospholipids and embedded with proteins. It is a thin semi permeable membrane layer, which surrounds the cytoplasm and other constituents of the cell*[1].

cytoplasm and provides structural support and protection to the cell. It consists of a lipid bilayer with several embedded proteins and liposaccharides (i.e. lipid + polymeric carbohydrate), see Fig. 1.2[1]. The lipid bilayer is formed by a thin polar membrane with a hydrophilic outer part and hydrophobic inner part, acting as a barrier against external toxic agents[2].

Besides of the plasma membrane, the cells count on extracellular entities that help in external protection, structural support, and communication. In plants or fungi, the plasma membrane is covered by a rigid and porous cell wall mostly composed of cellulose that provides mechanical protection but facilitating the entrance of nutrients. In animals, the so-called extracellular matrix (ECM) is a complex biochemical entity consisting of a wide variety of proteins and other molecules secreted by the cells. Generally, we can find three types of molecules in the ECM: fibrous structural proteins (*e.g.* elastin, collagen), adhesion proteins (e.g. fibronectin, laminin) and a gel made of proteoglycans and hyaluronic acid[2,3].

The ECM composition varies depending on the cell type and tissue, regulating the dynamic behavior of the cells. For instance, the ECM can sequester and accumulate grow factors that facilitate cell proliferation or induce novel functions. Also, the ECM enables the cells to sense the mechanical properties of the surrounding. The elasticity and stiffness of the ECM have significant implications in several fundamental processes, such as cell adhesion or migration[3,2,4]

1.1.1 Cell Adhesion

Cell adhesion is an active process that cells undergo when they interact or attach to a substrate or other cells. These interactions can last few seconds as in immunological signaling, or they can be long-lived as in tissue formation. Cell adhesion is, therefore, a fundamental process with crucial implications in biology, like the immune response, the tissue nature and architecture, or even the appearance and spreading of tumor cells.

Cells do not only stick together; they form complex cellular structures that enable communication between them and the ECM through the generation and transduction of mechanical signals (i.e. mechanotransduction). In other words, they convert biophysical cues (*e.g.*, external forces, matrix stiffness, and topography) into biochemical responses[5]. Thereby, the cell adapts its activity and contractility to the mechanical environment[2]. In mammalians, the cell adhesion process is mainly governed by transmembrane proteins, such as integrins, selectins or cadherins. These proteins, known as cellular adhesion molecules (CAM), are composed of three domains: an intracellular domain in contact with the cytoskeleton, a transmembrane domain, and an extracellular domain in contact with the surface or other components of the ECM. Cellular adhesion starts with the interaction between the CAM extracellular domain and the surface (anchorage points), initiating the formation of a large protein complex called focal adhesion (FA), see Fig. 1.3[6]. FAs are sites or zones of tight adhesion to the underlying ECM developed by tissue cells in culture during their adhesion. Then, the FAs are multi-protein assemblies mostly composed of integrins that connect and transmit both mechanical and biochemical information from the ECM to the cytoplasm. FAs act as sensors that can detect external forces and send the information inside the cell. There, the intracellular domain of the integrins starts a signaling cascade through the cytoskeleton that allows the cell to react with the characteristics of their surface. This cell reaction includes not only a biochemical response (e.g. synthesis of proteins or gene expression) but also mechanical

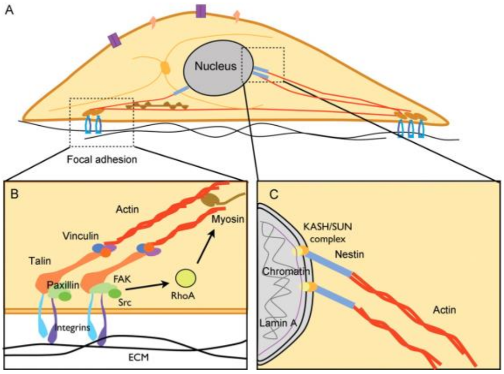

Figure 1.3. *Mechanotransduction from the ECM to the cell nucleus.* **(A)** *The actin cytoskeleton links focal adhesion at the cell membrane to the protein complexes located on the nuclear membrane.* **(B)** *Focal adhesions are sites of integrin clustering and adhesion to ECM.* **(C)** *Actin is bound to nestin proteins, which are directly connected to the KASP/SUN complex located on the nuclear membrane. Nuclear shape changes are associated with alterations in the structure of nuclear lamins and chromatin*[6].

responses (*e.g.* external forces due to the topography and the elastic properties of the ECM). Cells can react by exerting local forces against the substrate (i.e. focal adhesion forces) that influence its shape and movements. Thus, the overall process can induce changes in the morphology, signaling, proliferation, migration or even changes in the gene expression that lead to cellular differentiation (i.e. the process where cell changes from one cell type to another). For example, the neurons extend neurites only when they are on soft substrates. Smooth muscle cells, like fibroblasts, generate more traction force and develop a broader and flatter morphology on rigid surfaces[7]. This preference even induces cell migration, guiding them from soft substrates to harder ones[5,8].

1.1.2 Techniques for the detection of cell traction forces

Considerable attention has been paid to study and quantify the mechanical interactions of cells with the ECM. In particular, the design of tools able to measure traction forces remains a challenging problem due to their diversity, small areas where the cells attach (~μm^2) and range of magnitudes of these forces (at the pN-nN scale). Such tools should allow the detection of forces in the required range with a subcellular spatial resolution avoiding any external modification. They also should be designed to be biocompatible in order to allow conventional surface coating of ECM proteins to promote cell adhesion.

In the 1980s, Harris and co-workers were the first to visualize cellular traction forces qualitatively as visible wrinkles on deformable silicone rubber substrate, reflecting the strong traction forces exerted by fibroblast parallel to the direction of locomotion[9]. However, although it was an elegant approach, the method had several limitations such as the complicated relationship between the size of the wrinkles and the amplitude of the generated forces.

Based on the same principle, more advanced techniques have been developed to achieve a better spatial resolution, especially at individual adhesion sites. The method called traction force microscopy, is based on the use of elastic gels or membranes that avoid the formation of wrinkles[10]. Fluorescent beads are embedded into the gel and are used as markers to follow the deformation. Quantification of forces can be made through large-scale matrix computation that transforms maps of substrate deformation into maps of traction stress (force/unit area)[11,12].

Nevertheless, this technique requires high-resolution images and a high computational cost to follow the cell functions.

Alternative methods could be really useful in directly measuring traction forces exerted by individual FAs. Instead of using uniformly flexible substrate, an innovative approach has been to use of micromachined cantilevers as forces transducers [13]. Cells adhere and exert forces on micropads at one end of the cantilever, causing displacements that are detected with high precision under an optical microscope. The strains are confined to individual cantilevers and forces can be calculated by multiplying the distance of movement with the spring constant of the cantilever. However, the device is complicated to construct, and the surface topology can modify cell adhesive properties. Also, the detection area is limited by the number of cantilevers and the detection of forces is limited to one dimension perpendicular to the axis of the cantilever.

A similar approach has been developed using substrates composed of flexible arrays of micropillars[14].These devices are made of polydimethylsiloxane (PDMS) rubber formed from a microfabricated mold. In these cases, the deflection of each post gives a direct measurement of the local force exerted by the attached cells, independently of the forces acting on the neighboring posts. The pillars act as simple independent springs, and the linear theory of elasticity gives their deflection. For a cylinder of radius r and length L the bent by the application of a force F, it leads to the formula:

$$F = k \cdot \Delta x = \left(\frac{3}{4}\pi E \frac{r^4}{L^3}\right) \Delta x \tag{1.1}$$

Where E, k, and Δx are, respectively, the Young modulus, the spring constant and the deflection of the post. Thereby, these approaches have been applied to various situations including single cell mechanics[15], cell-cell interactions[16], stem cell differentiation [17]and multicellular systems[18]. However, the quantification of the forces is based on immunofluorescence imaging and also the microstructures do not mimic the rich nano-topography (*e.g.* collagen and fibrils) in which the *in vivo* cells are enveloped in the ECM.

Surface plasmon resonance imaging (SPRM) is other alternative technique which has been employed to investigate cell traction forces. This approach is based on the plasmonic evaluation of the local refractive index distribution. The sensor chips are glass coverslips coated with a thin film (~50 nm) of gold on a prism. This technique takes SPRM images of a single cell adhered on the Au film. The change in the cell-substrate interaction is monitored by recording the SPRM image over time. Then, the variation of intensity of the images reflected the local movement of the cell membrane in contact with the substrate. To analyze the local information quantitatively, the images are divided in 12 regions: R, reference, S1-S5 are the cellular areas, w1-w6, hole region. The SPR intensity *vs.* time in each region is observed. A relationship between the SPRM intensity and the cell substrate distance is purposed, and then, the local cell-substrate distance from the SPRM intensity is determined. Finally, it provides a spatial mapping of local cell-substrate adhesion (displacement image). Osmotic pressure was introduced to provide a controllable mechanical stimulation to the cell attached to substrate [19]. However, the images suffer distortions due to the coupling prism and the image analysis requires a high computational cost. Also, the technique is limited to a single cell, it does not quantify directly the traction forces and does not provide the rich nano-topography that the cells need.

The techniques at the state-of-the-art provide insights for the detection of traction forces of cells. However, those methods have limitations in fabrication design, detection and quantification of the forces. To overcome those challenges, a combination of the previous techniques could provide a new device based on the advantages of microfabricated pillars and the plasmonic detection and, thereby, this new tool could detect directly forces by plasmonic evaluation of the changes in the refractive index produced in the external medium and by the close near field interaction between flexible pillars. Also, the effective Young modulus (E) of array of nanopillars could be tuned to mimic soft and hard tissues. The spring constant k of the pillars could be tuned by changing the material composition and the nanopillars aspect ratio[20]. This new technology (plasmomecanical sensor) could be highly sensitive and compatible with other technologies (*e.g.* microfluidics) at the nanoscale.

1.2 Optical biosensors

When in a sensor a biological recognition element is built in (physically attached or confined) and is the primary selectivity element is named as biosensor[21]. A biosensor is formed by a recognition component that interacts with the target; a transducer that relates the interaction between the recognition component and the target to a piezoelectric, acoustic, electrochemical, or optical signal; and a read-out system to interface with this signal (see Fig. 1.4). For instance, biosensors can monitor biological interactions in real time allowing the evaluation of the affinity and kinetics of the interaction and, thereby, helping in elucidating the biochemical mechanisms involved in for example in a disease. Recent advances in nanofabrication further provide interesting opportunities for biosensor miniaturization, high-throughput, low-cost production and compatibility with other technologies. Biosensor platforms have shown exceptional capabilities to turn into portable and user-friendly devices which can be used at doctor's office or patient's home [22,23,24].In particular, optical biosensor devices are one of the most developed biosensor platforms. Optical sensing employs various methods, including refractive index change monitoring, absorption, or spectroscopic-based measurements. The optical sensors that are based on refractive index monitoring cover a range of technologies, including photonic crystal fibers, nano/microring resonator structures, interferometric devices, surface plasmon resonance (SPR) [25], and localized surface plasmon resonance[26]. The latter two are plasmonic-based technologies[27]. In this thesis, we have a special interest in LSPR sensors based on nanostructures. Firstly, the nanofabrication methodologies allow the realization of various designs of metal nanostructures such as nanoparticles (NPs), nanoholes[28], nanodisks[29], nanotriangles, nanostars, nanocones, among others, with precisely controlled shapes, sizes, and spacing[30]. Secondly, the nanofabrication techniques enable that the design of those nanostructures can be integrated with microfluidics. Thirdly, it is well known that the extremely intense and highly confined electromagnetic fields generated by the LSPR of the nanostructures

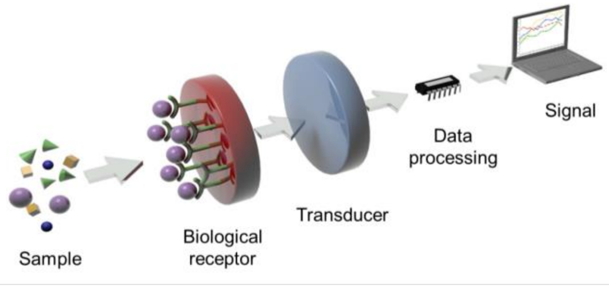

Figure 1.4. *Schematic representation of a biosensor including the heterogeneous sample, the specific biological receptor, the transducer, the data processing system and the final signal.*

can be employed as a highly sensitive probe to perceive small changes in the dielectric medium around the nanostructures[30].

Therefore, plasmonic nanostructures could be created on top of arrays of flexible nanopillars and their plasmonic response could be employed to detect both the presence of the cells and the pillar deflection caused by the near field interaction of the nanostructures. Also, the design of the array of the structures can be compatible with the microfluidic channels. Herein, the comprehension of the LSPR phenomenon is essential for the design, fabrication and operation of plasmonic nanostructures as sensors.

1.2.1 Localized Surface Plasmon Resonance

Fig. 1.5 shows the interaction between the electric field of an incident light and the free electrons of a gold sphere or nanoparticle whose size is smaller than the wavelength of light. The electric field can cause free electrons to move away from the metal particle in one direction, creating a dipole that can swap direction with the change of the electric field. When the frequency of the dipole plasmon is approximately the same as the incident light, a resonance condition is reached, then dipole plasmon is greatly amplified. Such a condition is referred to as Localized Surface Plasmon Resonance (LSPR) [31,32]. Only materials with a negative real and small positive imaginary dielectric constant are capable of supporting surface plasmons.

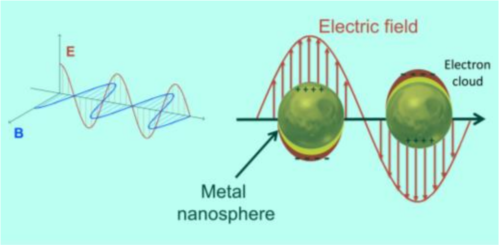

Figure 1.5. *Interation of an electromagnetic radiation with a gold nanosphere. A dipole is induced, which oscillates in phase with the electric field of the incoming light.*

Although Ag shows the sharpest and strongest LSPR, Au is preferred for biological applications due to its inert chemical nature and biocompatibility, and the well-known and established thiol-gold chemistry for immobilization of biomolecules[31,33].

The plasmon modes can extend up to a few tens of nanometers in LSPR nanostructures, allowing sensitive sensors[34]. Its spectral position and magnitude strongly depend on the composition, size, geometry, particle–particle separation distance of nanoparticles and the local dielectric environment, the latter being the factor on which the sensing capabilities of nanostructures rely[35]. For instance, when biomolecular binding events get close to the surface of a noble metal nanostructure, the refractive index of the immediate environment surrounding the nanostructure is increased. Thus, biomolecular interactions at the surface of the nanostructures directly lead to local refractive index changes, which can be monitored via the LSPR peak wavelength shift [30].

Typically, the LSPR energies and spectra of metal nanostructures are located in the visible or near-infrared regions of the electromagnetic spectrum, and their resonantly enhanced extinction cross sections are sufficiently high to allow imaging and optical characterization of single structures by means of dark field scattering spectroscopy, resulting in peak-shaped spectral responses. For the acquisition of spectral responses a white light source covering the visible spectrum is employed [36] and the scattered light of the plasmonic structures is collected with a spectrometer, thereby, the changes in the spectra are converted to interaction data. Interestingly, in LSPR the light is directly coupled to the plasmonic structures, therefore, the angle of incidence does not need to be precisely controlled[37]. LSPR measurements can be in the form of absorbance, reflection, transmission, scattering, or spectral shift observed in the extinction curves [37].

To evaluate the performance of a plasmonic sensor, we need to know their capability to detect changes in the monitored quantity (the refractive index), which ultimately determines the sensitivity of the sensor (S). The bulk sensitivity S_B is defined as the ratio of resonant wavelength shift $\partial\lambda_{res}$ to the variation of surrounding refractive index, ∂n_s:

$$S_B = \frac{\partial\lambda_{res}(nm)}{\partial n_s(RIU)} \tag{1.2}$$

Where RIU means Refractive Index Unit. A second factor affecting the sensing performance of the sensor is its resolving precision to detect changes of the monitored quantity. This parameter is typically represented by the full width at half-maximum (FWHM) of the resonance peak: a sharp peak facilitates the registration of a peak shift and viceversa. Therefore, when considering the performance of a sensor, it is necessary to evaluate both sensitivity and peak width[32,38,39]. The figure of merit (FOM) related both quantities and can be used to quantify the general performance of a sensor and to allow comparison with other sensing plaftorms. It is defined as:

$$FOM = \frac{S(nm \cdot RIU^{-1})}{\Delta\lambda(nm)} \qquad (1.3)$$

1.3 Microfluidic channels

In microfluidics, small and constant volumes of solvent, sample, and reagents are moved or mixed through microchannels embedded in a sensor. The new sensors includes a microfluidic system because it allows the small size of the *lab chip* offering to minimize the time and cost associated with the routine biological analysis and improving reproducibility[40]. In particular for the prototype of the sensor, we are interesting on the design and fabrication of a simple rectangular microchannel with a laminar flow.

In fluid mechanics, the Reynolds number (Re)[41] is a dimensionless quantity that is used to help predict similar flow patterns in different fluid flow situations. The flow can be laminar or turbulent giving different Re number. Turbulent flow is chaotic (i.e., it is impossible to predict the position of a particle in the fluid stream as a function of time). Laminar flow is a condition in which the velocity of a particle in a fluid stream is not a random function of time. Thus, the Reynolds number is a simple but important parameter. First, we need to know the flow rate, Q, (m^3/s) to calculate the Re number, it is given by,

$$Q = \Delta \mathrm{P}/\mathrm{R} \qquad (1.4)$$

Where ΔP is the pressure drop across the microchannel (Pa), R is the channel resistance. The pressure drop can be created: (a) by opening the inlet to atmospheric pressure and applying a vacuum at the outlet, or (b) by applying pressure at the inlet (e.g. via a syringe pump) and opening the outlet to atmospheric pressure. Also, the other determinant of flow rate is the channel resistance R, for a rectangular channel with high or low aspect ratio($\mathrm{w} \ll \mathrm{h}$ or $\mathrm{h} \ll \mathrm{w}$) it is given by

$$R = 12\mathrm{\mu l}/\mathrm{w}h^3 \tag{1.5}$$

Where μ is the fluid viscosity($\mathrm{Pa \cdot s}$), l is the length (m), h is the height (m), and w is the width of the channel (m), respectively. Also, the averaged fluid velocity for the flow is given by [42]:

$$v = \frac{h^2}{8\mathrm{\mu}}\frac{\Delta\mathrm{P}}{\mathrm{l}} \tag{1.6}$$

Finally, in fluid mechanics, Reynolds number is given by:

$$Re = v\, l\, \rho/\mu \tag{1.7}$$

Where v is the velocity of the fluid($\mathrm{m/s}$), l is the cross-sectional dimension(m), ρ is the density of the liquid (for water, $1000\ \mathrm{kg/m^3}$), and μ is the viscosity of the fluid (for water, $10^{-3}\ \mathrm{kg/(m \cdot s)}$). For aqueous solutions, ρ and μ are fixed parameters (characteristics of the fluid), and the rate of the fluid flow v and the channel dimension l are changeable[43]. Re <2300 as calculated by above formula, generally indicates a laminar flow. As Re approaches 2300, the fluid begins to show signs of turbulence, and as Re becomes greater than 2300 the flow is considered to be turbulent[41]. Then, the dimensions of microchannels can be designed by the previous formulas and can also be fabricated by the techniques such as photolithography.

1.4 Challenges and requirements

This Thesis has as main objective to fabricate a new prototype of a plasmo-mechanical sensor with integrated microfluidics to detect forces by the combination of nanofabricated structures with LSPR properties. The proposed sensor consists of a hexagonal array of polymer nanopillars within a microfluidic channel. The reasons to select this specific design are the following : i) The polymer nanopillars can support Au plasmonic nanodisks to use their high sensitivity not only to detect changes in the refractive index of the medium, but also to detect the deflection of the flexible nanopillars by a shear force, ii) the nanopillar deflection would not be limited to only one direction, iii) the array of polymer nanopillars can be fabricated in large scale (cm^2), iv) the array of polymer nanopillars can be created within a microfluidic channel to miniaturize the sensor, and to ensure the use of small volumes of samples and reagents.

To overcome the above discussed challenges in the Section 1.1.2, this sensor could be employed in a variety of applications such as in the detection of the traction forces by the LSPR response. The accurate control of the aspect ratio and material of the nanostructures could permit the tuning of the spring constant of the nanopillars to control their sensitivity to a shear stress by a force and to mimic different tissues for possible cellular applications. In particular, the sensor could be adapted to the cell dimension (μm^2) and density. It should satisfy the nano-topography that *in vivo* the cells are enveloped in the ECM.

Also, the sensor material should be biocompatible, and by using the microfluidic system, the structures could be easily functionalized to promote cell adhesion, if required.

The production of the sensor with the previous requirements is a demanding technological challenge. Its design and development requires the combination of several techniques which allow the integration of polymer nanopillars, plasmonic nanostructures and microfluidics in a concerted way without disrupting the properties of each other. The confluence of the three aspects of the proposed sensor can be achieved by the combination of appropriate nanofabrication techniques.

1.5 Nanofabrication Techniques for the sensor

In the next sections, we present the main nanofabrication techniques that we have employed to create the prototype of the plasmomechanical sensor.

In general nanofabrication involves processes and methods for constructing nanostructures and devices having minimum dimensions lower than 100 nm. The nanofabrication methods are divided into two major categories: top–down and bottom–up approaches according to the processes involved for creating nanoscale structures. Bottom–up approaches seek to have molecular or atomic components built up into more complex nanoscale assemblies or directed self-assemblies based on complex mechanisms and technologies. This area of nanofabrication uses atoms or molecules as the building blocks of multi-level structures and is extremely promising since it could lead to no waste or unused materials [44–47].

On the other hand, top–down approach uses nanofabrication tools to create soft and rigid micro/nanostructures or functional devices with the desired shapes and characteristics starting from larger dimensions and reducing them to the required values [45,46]. Also, these techniques operate at large scale, and are not very complicated, which makes them attractive for fabrication of the sensors.

1.5.1 Optical lithography

Optical lithography is one of the most employed technique mainly in the microelectronics field for patterning micro-nanoscale features, and is also used for microfluidics technology. Optical lithography employs standard procedures that allow the easy and reproducible creation of novel geometric patterns. In brief, conventional optical or photolithographic approaches use light that is collimated through a quartz plate supporting a chromium coating to create smart patterns on a surface (e.g. a silicon wafer or glass). The quartz plate which serves as a mask is placed in contact with the resist-coated wafer. The photoresist is an organic, light-sensitive material that can coat on semiconductor wafers[46].This technique has a resolution of about 1 µm when using a wavelength of 400 nm. Photolithography is a simple and common method that can be used for the fabrication of the microfluidic channels of the sensor proposed in this work [11,13] [48].

1.5.2 Strategies for Fabrication of Silicon Nanopillars

For the manufacture of the prototype of the sensor, in this Thesis, we are interested in employing low-cost, and large-scale fabrication techniques to create silicon nanopillars integrated into microfluidic channel, which can be employed as a master mold for the manufacture of the flexible nanopillars. Besides the techniques need to be compatible with standard photolithography processes for the fabrication of the microfluidic integration.

In the literature, the fabrication of nano/micropillars has been achieved using a variety of techniques such as electron beam lithography [49], photolithography [50], focused ion beam chemical vapor deposition [51], vapor liquid solid mechanism[52], molecular beam epitaxy [53–55], laser ablation [56], pulsed laser deposition [57], thermal evaporation [58], reactive ion etching[59], colloidal lithography[60] and metal-assisted chemical etching [49,61]. The main materials for the fabrication of the nanopillars include silicon (Si), metals, metal oxide, ceramics, and polymers.

In this context, silicon nanopillars have become a popular configuration because of their unique optical and electronic properties, e.g. conductivity and resistivity[62].

We are interested in the combination of several nanofabrication techniques such as Nanosphere Lithography (NSL)[60] with reactive ion etching (RIE)[63], thermal evaporation and metal-assisted chemical etching[64,65] which have provided intriguing possibilities for fabricating Si nanopillar arrays[60] .The NSL technique has been widely used as an effective intermedium for the fabrication of Si nanopillar arrays because the sphere monolayers can cover large areas of up to 140 cm^2 at a low cost[60,66,67]. The spheres can be readily self-assembled into single layers to conform a high-quality hexagonal array over a polymer based microfluidic channels. By selecting the initial size of the nanospheres, it is possible to set the distance between the SiNPs, which is an important parameter for replica moulding of soft materials[68,69].

Secondly, the diameter of the nanospheres can be reduced to the desired diameter of the SiNPs by adjusting the RIE time and conditions. Thirdly, the catalytic gold mesh can be defined by depositing functional materials (Au, Ag, Pd, Pt) on top of the etched nanospheres, a process known as lithographic masking. Finally, by combining the mesh design of the nanostructures with the advantages of metal-assisted chemical etching, the length, shape, orientation, and morphology can be controlled[65,70]. Also, this strategy is compatible with photolithography to build well-ordered Si nanopillar arrays into a polymer-based SU-8 microfluidic channel.

1.5.3 Colloidal Self-Assembly Method

Self-assembly of colloidal micro-nanospheres is an effective strategy for fabrication of ordered nanostructures. By a combination of colloidal self-assembly with nanofabrication methods, two-dimensional (2D) colloidal crystals have been employed as masks for evaporation, deposition, etching, and imprinting, etc. These methods are defined by colloidal lithography or nanosphere lithography (NSL), which is a facile, inexpensive, and repeatable nanofabrication technique. Colloidal micro-nanospheres have been used because they range from micrometers to tens of nanometers, which is close to the limit of conventional patterning techniques.

Self-assembled 2D colloidal crystals are usually assembled on planar substrates or at air/water interface with ordered arrangement. Colloidal lithography is employed for both the ordered packing of self-assembled colloidal crystals and for fabrication of ordered nanostructure arrays. These nanostructures have the same period as that of the 2D colloidal crystals, which is determined by size of the nanospheres. Nanosphere diameters from 200 nm to 1 µm are usually used. The materials and shapes of the nanostructure are determined by nanofabrication methods such as spin-coating[71] or electrophoretic deposition[72]. Using 2D colloidal crystals as masks during evaporation of metals, triangular nanoparticles and thin film with nanohole arrays are obtained on the exposed substrate [28]. Also, using 2D colloidal crystals as masks for etching of substrates, nanodisks, nanotips or nanopillars have been fabricated in polymer, silica, silicon, and other semiconductor substrates[60].

Self-assembled 2D colloidal crystals are mostly hexagonal close-packed (hcp) because the hcp structure is the most stable thermodynamic position with minimum free energy. Colloidal nanospheres dispersed in various solvents are influenced by interactions including *van der Waals forces*, *steric repulsions***,** and *Coulombic repulsions*. Self-assembly of the colloidal nanospheres is governed by the balance of these interactions. Self-assembly conditions and parameters, such as temperature, air pressure, solvent, humidity and the contact line, are crucial to control of the morphology and to improve the quality of colloidal crystals.

Reactive ion etching

In a typical procedure, colloidal nanospheres are spread onto a liquid surface through a spreading agent. After evaporation of the solvent, the nanospheres form a highly ordered floating monolayer over a large area. The resulting floating monolayer is first compressed by a barrier to a close-packed monolayer and then deposited onto the receiving substrate. 2D colloidal crystals at the air-liquid interface can be transferred to many types of substrates, regardless of surface polarity, roughness, or curvature [73–75].

Therefore, many kinds of nanostructures arrays have been fabricated such as Ta nanocolumns with 200 nm wide and 600 nm height by glancing angle sputter deposition (GLAD) onto self-assembled close-packed arrays of 260 nm diameter silica spheres [76]. Hierarchical TiO_2 nanocolumn arrays (diameter 350 nm, height 870nm) has been fabricated by pulsed laser deposition (PLD) using polystyrene (PS) colloidal monolayer (350 nm diameter) as a template[77].

1.5.4 Reactive ion etching

Dry process technology includes both plasma and reactive ion etching (RIE). RIE is an ion-assisted reactive etching method which has excellent process control (homogeneity, etch-rate and selectivity). An important characteristic of RIE is its ability to achieve etch directionally and faithfully transfer lithographically defined photoresist patterns into underlying layers, and cleanliness. RIE is based on a combination of chemical and physical etching which allows isotropic and anisotropic (uni-directional) material removal. The etching process is realized in a chemically reactive plasma formed by negatively and positively charged ions produced from the gas that is pumped into the reaction chamber. Thus a mask is used on top of the substrate to protect certain areas from etching, exposing only the areas to be etched. The ions accelerate into the etching region, where they attack the substrate surface and react with it. This method uses ion-assisted processes, where heavy ion bombardment damages chemical bonds and the radicals chemically react with exposed surface atoms generating a volatile product. RIE provides excellent pattern-transfer results even for very fine structures significantly under 100 nm. [78,79,80]

Combining top-down methods with bottom–up methods (e.g. photolithography, e-beam evaporation, etc.) the realization of nanostructures and architectures, including nanopillars and Si nanowires, has been achieved. For instance, Chang and co-workers fabricated Si nanopillars arrays with diameters smaller than 200 nm by RIE technique and nickel masks[59]. Also, Ogawa et al. produced quartz nanopillars for DNA separation[81]. As mentioned above, the diameter of the polystyrene nanospheres can be reduced to the desired diameter of the Silicon nanopillars by adjusting the RIE time and conditions.

1.5.5 Thermal evaporation

Thermal evaporation method is a simple process in which condensed or power source material is vaporized at an elevated temperature and the resultant vapor phase condenses under certain conditions to form the desired thickness or product. The morphology and phase structure of product depend on not only the parameters adopted but also on the source material employed. There are several parameters such as temperature, pressure, carrier gas (including gas species and its flow rate), substrate, and evaporation period, which can be controlled and need to be selected properly before and during the thermal evaporation. The choice of source temperature mainly depends on the volatility of the material. Usually, it is slightly lower than the melting point of the material.

There are two ways of heating the material. One method often referred to as filament evaporation, is a simple electrical resistive heat element, or filament. The other heat source is an electron beam, and this is known as E-beam evaporation [82]. Umar and co-workers reported the protocol to synthesize aligned hexagonal coaxial-shaped ZnO nanocolumns on steel alloy by thermal evaporation, the diameters and heights of the nanocolumns are in the range of 700-900 nm and 8-10 µm[58], respectively . This technique allows depositing thin films of metals (e.g. gold and titanium) to form nanodisks on soft and rigid substrates which makes it attractive for our purposes of fabrication of the sensor.

1.5.6 Metal-Assisted Chemical Etching

Metal-assisted chemical etching is an efficient and low-cost top-down approach that permits a highly controlled and precise fabrication of Si and Si/Ge nanostructures at large scale. It is a simple method with the ability to tailor diverse nanopillars parameters like length, orientation, doping level, doping type, and morphology. In a typical metal-assisted chemical etching procedure a Si substrate is covered by a lithographic noble metal film (e.g. Au and Ag) and etched in a solution containing hydrofluoric acid (HF) and an oxidant (typically H_2O_2). In general, the function of the metal is to catalyze the reduction of hydrogen peroxide (H_2O_2) which delivers electronic holes necessary for the oxidation and the subsequent dissolution of the Si oxide by HF. The Si beneath the noble metal is etched much faster than the Si without noble metal coverage. As a result, the noble metal sinks into the Si substrate [83], following the widely accepted overall reaction [70]:

$$Si + 6HF + \frac{n}{2}H_2O_2 \rightarrow H_2SiF_6 + nH_2O + \left[\frac{4-n}{2}\right]H_2 \qquad (1.8)$$

This technique involves two steps. First, a structured noble metal film is deposited on the substrate, e.g. via nanosphere lithography[60]. Subsequently, etching in HF and an oxidative agent like H_2O_2, $AgNO_3$, $KAuCl_4$ or $KMnO_4$ is performed [61]. This technique can be utilized to fabricate straight and well-defined pores or nanopillars with diameters ranging from 5 nm to 1 µm. A variety of studies has been performed to analyze the influence of the type, and the thickness of noble metals used as catalysts (Ag, Au, Pd, Pt). Also, the effect of doping level, doping element, the crystallographic orientation of Si substrates, as well as temperature, illumination, and the concentration of the etching solution[84,85].

1.5.7 Fabrication of polymer nanopillars

As mention above, an important component of the prototype of our optomechanical sensor is the array of flexible nanopillars that support the plasmonic nanodisks. In the previous sections, Silicon Nanopillars fabrication has been achieved by using a variety of techniques which have proved to be appropriate for the achievement of structures with a high aspect ratio. However, there is a strong challenge to fabricate high-aspect-ratio and high-density elastic nanopillars. Soft lithography represents an excellent strategy based on self-assembly and replica molding for carrying out micro and nanofabrication. In particular, it provides a convenient, efficient and low-cost method for the formation of polymer nanopillars. The polymers are favoured in many applications because many of them are transparent, and can be biocompatible and biodegradable. Moreover, polymer devices are inexpensive and disposable, which is highly desirable for the fabrication of our sensor.

1.5.8 Soft lithography

Soft lithography is a set of methods that uses organic (soft) materials to enable replication and pattern transfer on multiple length scales (from nanometers to centimeters). The term soft is used to refer to the mold when it is formed of soft matter (e.g., polymers or self-assembled monolayers). It provides an efficient and low-cost technique for the formation of micro-nanostructures. In soft lithography, an elastomeric mold with patterned relief structures on its surface is used to create patterns and structures with feature sizes ranging from ~30 nm to ~100 µm. Also, soft lithographic methods are low in cost, easy to apply, and accessible to a wide range of users. They can employ a wide variety of materials and surface chemistries. The pattern transfer consists of three steps: (a) fabricating a topographically patterned master mold, (b) molding this master to generate a patterned mold, and (c) generating a replica of the original template in a functional material.

One drawback of soft lithography is that it still requires the assistance of conventional tools to design and fabricate the masks or master molds[86,87]. But, soft lithographic techniques can produce numerous molds and replicas from the same master and thus provide good nanofabrication capabilities required for our purposes of fabrication of the sensor.

1.5.9 Replica Molding

Replica molding fabricates objects with a particular topography by solidifying a liquid polymer precursor against a topographically patterned mold. There are numerous approaches to replica molding using both rigid and soft topographic molds. We used a combination of the next techniques to create the optomechanical sensor with microfluidics.

Step-and-flash lithography

Step-and-flash lithography uses a rigid, transparent (usually quartz) master; the process proceeds by placing the rigid mold in contact with a low-viscosity, photocurable polymer (Fig 1.6 a). A fluorosilane is typically covalently linked to the surface of the master to lower its surface free energy and to make it easier to separate the master and the cured polymer [88]. Then, the liquid prepolymer conforms to the rigid mold and requires only slight pressure be applied to the mold to reduce the thickness of the residual film between isolated features. Exposing the prepolymer to UV light through the transparent mold initiates photo-induced cross-linking. Little mechanical stress is imposed on the system during molding, mostly from a decreasing volume of the polymer during cross-linking. This technique also is self-cleaning because particulate matter on the surface of the rigid mold is captured mechanically in the cross-linked polymer replica and thus removed from the mold. Step-and-flash lithography avoids thermal and pressure-induced deformations of nanostructures and can replicate features with lateral dimensions as small as ~30 nm. The limitations of this replica molding technique include the difficulty of patterning nanostructures on nonplanar surfaces and the presence of bubbles.

Replica molding using a soft mold

Replica molding is another efficient strategy for the duplication of the shape, morphology, and structure present on the surface of a mold [49]. UV or thermally curable prepolymers, as long as they do not contain a solvent, usually have shrinkage of less than ≈3 % on curing. The fidelity of this process is largely determined by van der Waals interactions, wetting, and kinetic factors such as filling of the mold. These physical interactions are short range and should allow more accurate replication of small (<100 nm) features than does photolithography [89].

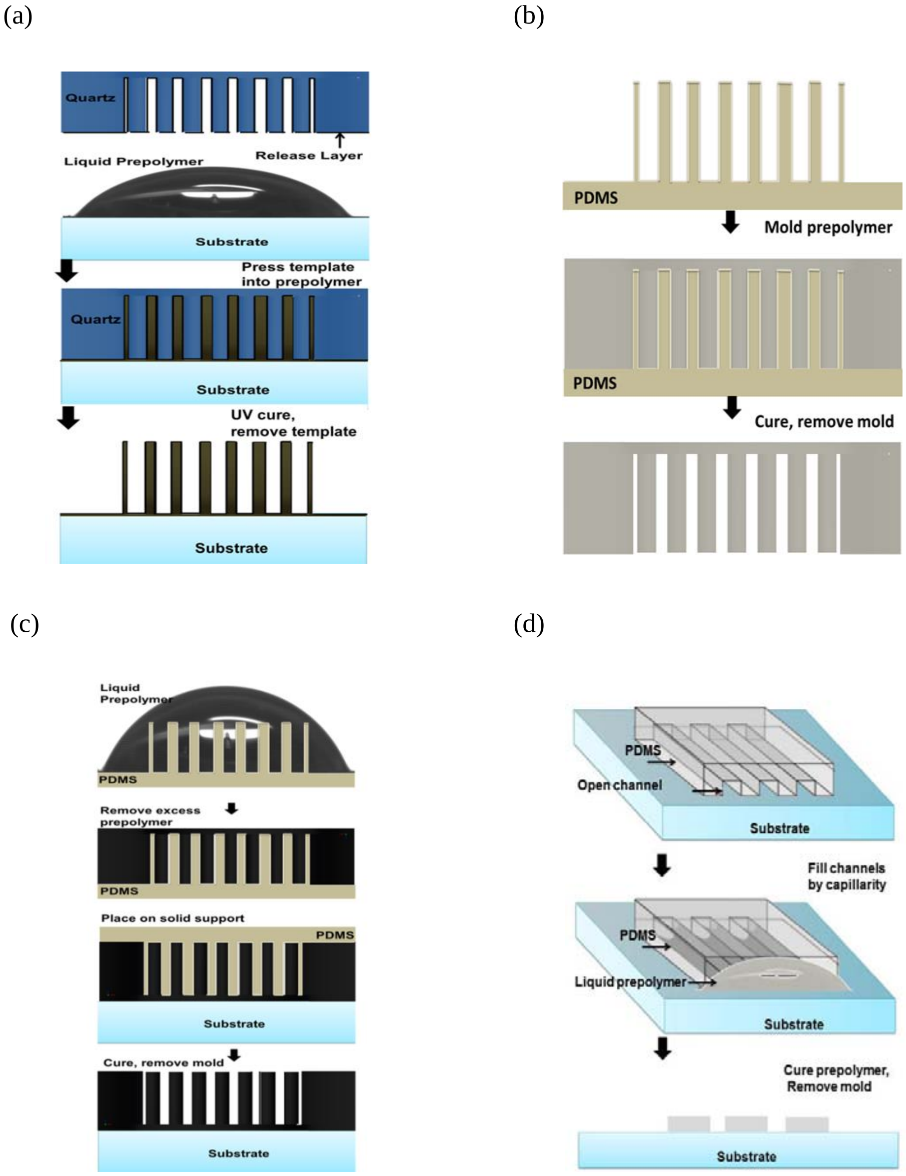

Figure 1.6. *Schematic diagrams of four approaches to replica molding:* (a) *Step-and-flash,* (b) *replica molding (RM),* (c) *micro-transfer molding (µTM), and* (d)*micro-molding in capillaries (MIMIC)* [86]

Replica Molding

Replica molding allows duplication of three-dimensional topologies in a single step, and it also enables faithful duplication of complex structures in the master in multiple copies with nanometer resolution in a simple, reliable, and inexpensive way. In replica molding, a rigid mold with an appropriate material (polymers) are used for the mass-production of a wide range of structured surfaces such as silicon nanopillars[69]. The capability of this procedure extends by molding against elastomeric molds rather than against rigid mold (Fig. 1.6b). The molds are prepared by casting against rigid masters using a procedure similar to that used in step-and-flash. Each elastomeric mold can be used for multiple replications (>25 times)[69]. The relief features on the elastomeric mold can, in turn, be faithfully replicated by using this structure as a mold for forming structures in a second UV-curable (or thermally curable) prepolymer. The relief structures on the replica are complementary to those on the mold and very similar to those on the original master[69].

A benefit of replica molding with polymer is the ability to mold against nonplanar, rigid, and soft topographic surfaces. Capacity to mold a range of materials and topographies, the potential for large area molding, and the ability to produce multiple elastomeric molds (dimensions <100 nm) [86] inexpensively from a single master, makes this technique potentially useful for fabrications requiring low costs.

Microtransfer molding (μTM)

In this technique, the liquid prepolymer fills the recessed regions of the mold, and the excess prepolymer is removed from the top surface using a flat edge or glass (Figure 1.6c). After, placing the mold in contact with a rigid substrate, the prepolymer is cured by appropriate protocols. Microtransfer molding has been used to pattern planar or curved surfaces. The patterned features are cured while in contact with a surface, and the elastomeric mold peeled away [90].

Micromolding in capillaries (MIMIC)

This technique uses capillarity to fill a series of channels in a topographically patterned elastomeric mold with a fluid, low-viscosity polymer or ceramic precursor; because the elastomeric mold is in contact with the substrate before the polymer is introduced, this method does not leave residues between the patterned features. A patterned elastomeric stamp placed in contact with flat surface forms a network of open micro (or nano) channels. A low-viscosity precursor placed at one end of the channels fills them by capillarity. The precursor material is cured within the channels, and the mold is peeled away to reveal a positive reproduction of the open network. The speed of filling is determined by the combined influence of precursor viscosity, channel radius, the interfacial free energy of the surfaces, and distance the precursor has traveled along the canal, Fig. 1.6d [91].

1.5.10 Embossing and Nanoimprinting

Embossing techniques have been extended to nanofabrication with resolution well below 50 nm[92]. Nanoimprint lithography is the term coined for a procedure that transfers a pattern from a rigid mold into a deformable material coated on a rigid surface. The material, typically a polymer, is heated above its glass-transition temperature (e.g., 90–200 ˚C), while pressure is applied to the rigid mold (e.g., 50–130 bar)[93,94]. The mold is removed after cooling the substrate to below the glass-transition temperature. Imprinting can replicate structures with aspect ratios up to 10:1 and as small as ≈10 nm [94]. Pattern transfer takes about 5 to 10 min (and sometimes longer) depending on the efficiency of heat transfer within the system. Solvent-assisted micro molding uses an elastomeric mold in combination with an appropriate solvent instead of a rigid mold and high temperatures and pressures to emboss the polymer film. The solvent, rather than temperature, softens the polymer. The solvent is either briefly applied to the elastomeric mold or retained in the polymer film before placing the two surfaces in contact[95]. The polymer is drawn into the crevices of the molds the solvent is removed from the mold polymer interface by transport and evaporation through the mold. The permeable mold prevents trapping of air pockets and non-uniform solvent evaporation. The mold is removed (after evaporation of the solvent) to reveal a relief structure complementary to the topography of the mold.

1.6 Objectives

The main objective of this Thesis is to study and take advantage of nanofabrication tools to design, develop and fabricate a versatile novel plasmo-mechanical sensor with microfluidics for the optical detection of forces, such as the one produced by cellular traction.

The proposed sensor consists of a hexagonal array of closely spaced, vertical, elastomeric nanopillars capped with plasmonic gold nanodisks embedded in a microfluidic channel. The polymer microfluidic channel aims to work with a laminar flow. The experimental design is divided into the following processes: 1) fabricating a Si master mold, 2) molding this master to generate a patterned stamp (PDMS mold), 3) generating a replica of the original template in a polymer material, 4) evaporation of plasmonic gold nanodisks on the polymer nanopillars and 5) sensor bonding, as shown in Fig. 1.7.

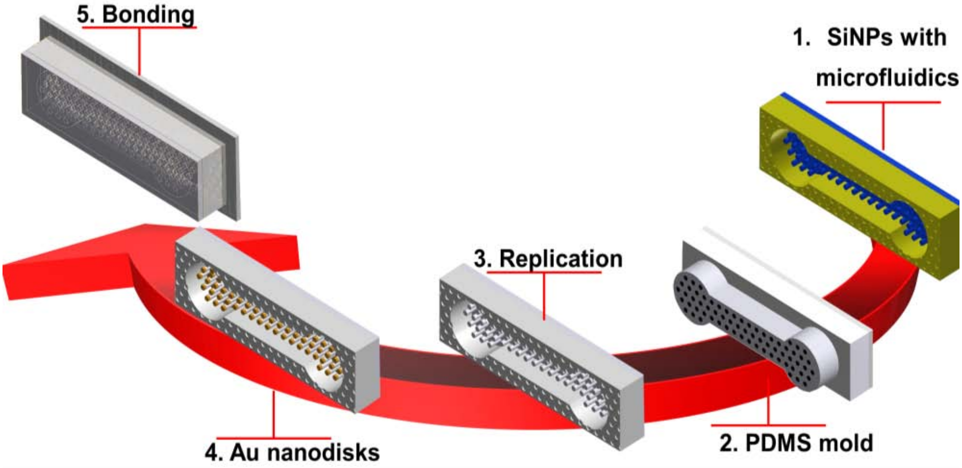

Figure 1.7. *Schematic diagram of fabrication process of the plasmo-mechanical sensor.*

We propose an optical detection system based on combining the mechanical flexibility of the polymer nanopillars with the optical properties of the plasmonic gold nanodisks that exhibit Localized Surface Plasmon Resonances (LSPR) with the motivation of detecting and identifying the traction forces of the living cells. We expect that two effects will happen when the cells are on the sensors:

Effect 1. We first take a spectrum of the LSPR without cells as a reference in the area to analyze. The cells will initially adhere to the nanopillars, thereby causing a local change in the refractive index around the plasmonic nanodisks (see Fig. 1.8a). We expect that the LSPR will be red-shifted a few nano-meters as a consequence of the refractive index increase, and this effect will be polarization insensitive, that is, the red-shift will be the same if the polarization of the light is parallel (transversal magnetic-TM) or perpendicular (transversal electric-TE) to the light incident plane, as shown in Fig. 1.8b.

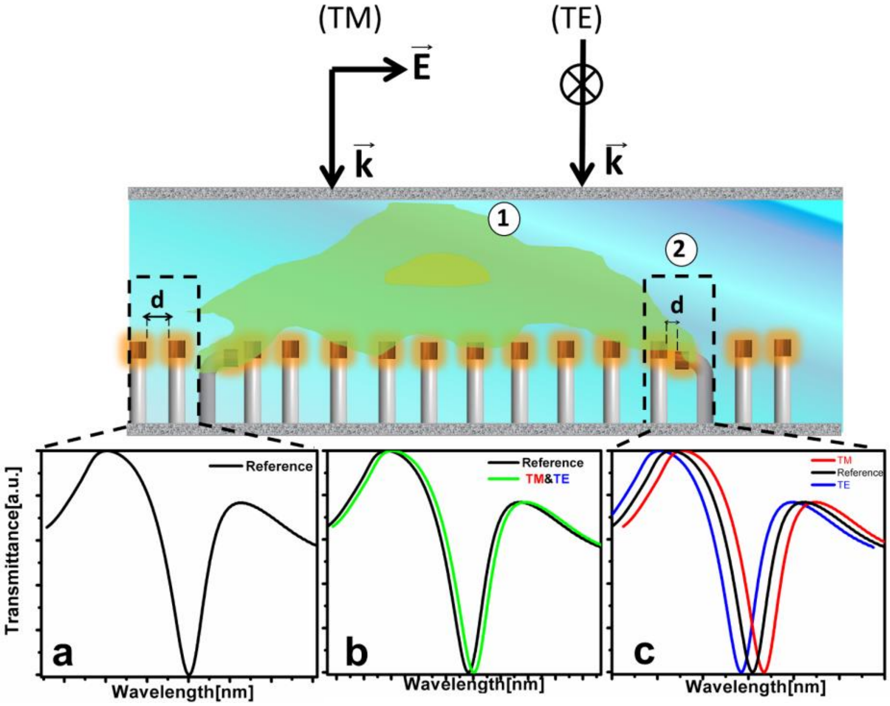

Figure 1.8. *Schematic diagram of the detection principle of the plasmo-mechanical sensor to study cells.* (*a*) *Representative LSPR spectrum without cells as a reference.* (*b*) *Representative LSPR spectrum (green curve) due to the refractive index of the cell by using both polarization of light TM and TE.*(c) *Representative LSPR spectra due to the cellular traction forces by using both polarization of light TE and TM.*

Effect 2. Once firmly adhered, the cells will exert shear forces in the Au-capped nanopillars, as reported in references [96–100], and thereby, the nanopillars will bend approaching the plasmonic gold nanodisks of the neighboring pillar, if the nanopillars design and material parameters are well chosen.

Thus, when the plasmonic gold nanodisks are approaching one another and they are at a distance shorter than its diameter they will begin to interact by near-field, that is, by dipole-dipole interaction. Depending on the polarization of light, the interaction will produce a red-shift or blue-shift, as shown in Fig 1.8c. If the polarization of light is parallel to the direction of the nanopillar deflection, a red-shift is expected. This is because the energy of the dipoles tends to decrease as they approach one another. In contrast, if the polarization of light is perpendicular, a blue-shift is expected. Therefore, the polarization of light can help to distinguish the LSPR spectra of vertical and bent nanopillars as well as the dielectric medium.

Specific objectives:

*To design, study, fabricate and characterize a well-controlled protocol for the creation of high-aspect-ratio silicon nanopillars integrated into a microfluidic channel (master mold), using top-down nanofabrication techniques in order to design sensors with suitable optical and mechanical characteristics.

*To design, study, fabricate and characterize a well-controlled protocol for the replica of the silicon master mold to produce flexible nanopillars, using replica molding techniques.

*To incorporate plasmonic gold nanodisks on top of the polymer nanopillars while preserving their plasmonic response.

*To calculate the spring constant the polymer nanopillars.

*To design and characterize the protocol for the bonding between the microfluidic channel containing the polymer nanopillars with the gold plasmonic nanodisks, and a PDMS lid.

*To perform FDTD simulations to study and understanding the LSPR scattering and transmission of the plasmonic gold nanodisks of the new sensor and perform an experimental characterisation to compare the results.

*To perform a proof the feasibility of the Au-capped polymer nanopillars for cell culture.

*To perform a preliminary proof of concept to know the capabilities of the sensor to a possible detection of cellular traction forces.

1.7 Dissertation Outline

The present Thesis "***Development of integrated plasmomechanical sensors in microfluidic devices for live cell analysis***" aims to contribute on the field of Bioengineering. This work presents a new versatile plasmomechanical sensor that could be attractive for the field of biological analysis. The Doctoral Thesis is divided into the following chapters:

In **Chapter 2**, we explain the nanofabrication methodology that integrates silicon nanopillars (SiNPs) in a microfluidic channel (Silicon master mold) to address the development of the plasmomechanical sensor. With the method, the area, position, height, diameter, and aspect ratio of the SiNPs is highly controlled within the microchannel domain. The nanofabrication strategy is based on a lithographic gold mask placed inside a SU-8 microfluidic channel that combines the nanosphere lithography method, reactive ion etching treatment and the e-beam technique to control the diameter of the structures. Meanwhile, the height of the SiNPs heavily depends on a well-controlled metal-assisted silicon etching protocol. We demonstrate experimentally the study and the evolution of the fabrication protocol.

In **Chapter 3**, we present: (i) the strategies for controlling the replication of Si master using thermal and photopolymers with different Young's modulus, to minimize the distortions and to obtain a reliable replica of the Si master. (ii) The mechanical characterization of the polymer nanopillars (spring constant). (iii) The polymer-based bonding strategies for microfluidic integration of the plasmomechanical sensor.

In **Chapter 4**, (i) the LSPR modes of hexagonal array of the Au-capped polymer nanopillars (with and without perforated gold film) are simulated using FDTD calculations, and the results are verified experimentally. (ii) The bulk sensitivity of the sensors is examined. (iii) The hydrophobicity of the sensors is evaluated.

In **Chapter 5**, a preliminary study about the feasibility of Au-capped polymer nanopillars for cell culture is discussed. The effect of culture media on the LSPR response is tested. Also, a preliminary proof of concept for the LSPR detection of fibroblasts on the sensors is described.

Finally, the general conclusions are presented, focus on the main contribution of this thesis and the future work.

In **Annex A**, elastic modulus of different tissues (spring constant, k_{tissue}) and the approximated values of aspect ratio of nanopillars required to match the stiffness of the tissues are described.

In **Annex B**, the script in Matlab that calculates the spectral LSPR dip position (λLSPR) is presented.

In **Annex C**, the protocol for fixing attached cells in paraformaldehyde employed by the Servei de Microscòpia Universitat Autònoma de Barcelona is described.

Chapter 2. Si master mold of the sensor

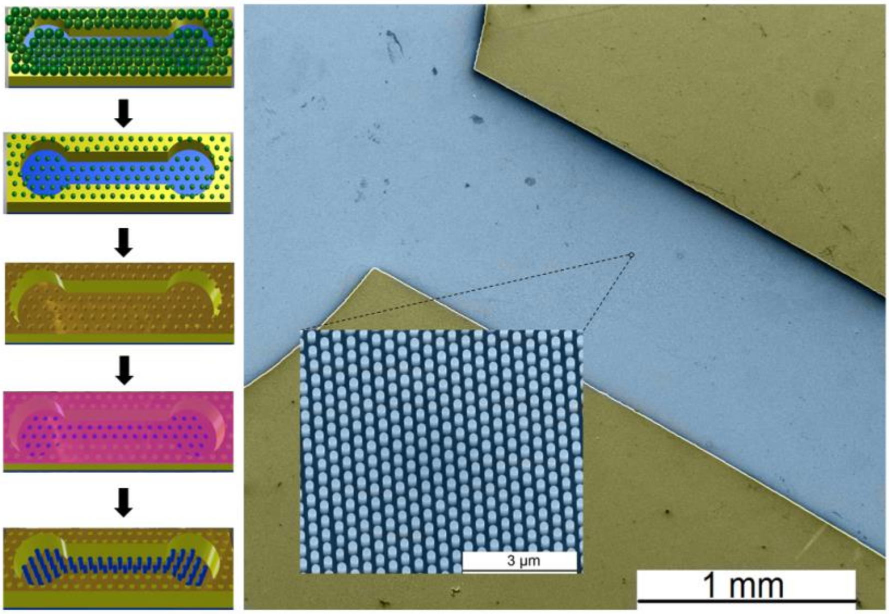

2.1 Introduction

Nanotechnology has been playing an increasingly important role in the development of new sensor platforms. The use of nanomaterials and the ability to build structures with nano-scale dimensions has enhanced the sensitivity and performance of these sensors. Recently, the use of vertically aligned nanopillars has been proved to be advantageous for developing new sensing devices[101–108]. Particularly, in the emerging field of plasmonics, the configuration of nanopillars has been explored for different applications. For instance, a simple strategy is used for reducing the substrate effect by lifting the enhanced electromagnetic fields of the nanostructures from the substrate by a dielectric pillar, thereby substantially enhancing the bulk refractive index sensitivity of the nanostructure LSPR [109,110]. Similarly, plasmonic metal particles on polymer nanopillars have shown to improve the refractive index sensitivity of LSPR sensors[111–114]. Additionally, the fascinating optical properties of metal nanopillars (e.g. Au and Ag) have been extensively investigated both experimentally and theoretically, providing new pathways for manipulating light at the subwavelength scale, for developing new plasmonic applications[115–119]. Also metal (Ag and Au) capped silicon nanopillars are studied to evaluate the impact of the overall geometry of the structures for use as surface-enhanced Raman scattering (SERS) sensors templates[120,121].

One of the challenges in the fabrication of plasmonic sensors based on nanostructures is to create reliable and controllable features with large-area patterns, and with subwavelength spatial-resolutions at low-cost and in a reproducible manner. It is widely recognized that the spectral position and magnitude of the LSPR strongly depends on the composition, size, geometry and separation distance of nanostructures as well as in the local dielectric properties of their surrounding environment[27,109,111,113,122,123]. Reliable techniques and reproducible nanofabrication protocols are needed to create new and cost-effective sensor platforms compatible with other technologies. These protocols must be flexible to identify the parameters, limits, and defects that influence the fabrication of the sensor. On the other hand, considerable efforts have been made to integrate nanostructures within microfluidic channels given the close interplay of microfluidics with the sensor technology.

For instance, the introduction of well-ordered nanopillar arrays into microfluidic channels has been employed to study the electroosmotic flow suppression during electrophoretic separation[124], or to control the fluid flow by modifying the wettability surface of microchannels[125]. Conventionally, bottom-up and top-down techniques have been employed to produce microfluidic devices[126] and silicon nanopillars (SiNPs) [50–58,60,63–65]. However, each fabrication technique provides specific characteristics, advantages, and limitations over the control of the fabrication process and over the ability to combine them. It is clear that the choice of the most suitable technique to fabricate a sensor is determined by several factors, such as available technologies and facilities, cost, time, available materials, and fabrication capabilities (e.g desired size of the micro-nanostructures).

Lately, the combination of several nanofabrication techniques such as the Shadow Nanosphere Lithography (SNSL)[60] with reactive ion etching (RIE)[63], thermal evaporation and metal-assisted chemical etching[64,65] has provided intriguing possibilities for fabricating Si nanopillar arrays[60] for several reasons. Firstly, the SNSL technique has been widely used as an effective intermedium for the fabrication of Si nanopillar arrays because the sphere monolayers can easily cover large areas of up to 140 cm^2 at a low cost[60,66,67]. The spheres can be readily self-assembled into single layers to conform a high-quality hexagonal array over polymer based microfluidic channels. By selecting the initial size of the nanospheres, it is possible to set the distance between the SiNPs, which is an important parameter for replica moulding of soft materials[68,69]. Secondly, the diameter of the nanospheres can be reduced to the desired diameter of the SiNPs by adjusting the RIE time and conditions. Thirdly, the catalytic gold mesh can be defined by depositing functional materials (Au) on top of the etched nanospheres, a process known as lithographic masking. Finally, by combining the mesh design of the nanostructures with the advantages of metal-assisted chemical etching, the length, shape, orientation, and morphology can be controlled[65,70].

In spite of the aforementioned advantages, the combination of these nanofabrication techniques has so far been subject to limitations and defects when producing SiNPs. For instance, an inappropriate change in the periodicity, the presence of some defects, as well as hydrocarbon contamination on the catalytic mesh can strongly influence the etching rate and morphology of SiNPs, producing unstable and inhomogeneous structures.

This can damage not only the reproducibility of the fabrication but also the properties of the final sensor device. A detailed study of the methodology to fabricate a sensor based on Si nanostructures is highly necessary.

To address the fabrication issues mentioned above and to extend the applicability of this strategy to integrate on-chip microfluidics, in this chapter, we provide a low-cost and high-throughput protocol to build well-ordered Si nanopillar arrays into a polymer-based SU-8 microfluidic channel. In this way, the advantages of the integration with the microfluidics in terms of reduced analysis time, reagent consumption, and decreasing cost can be exploited. We have performed a study and assessment of the main fabrication techniques used in this methodology which is critical for developing controllable processes to produce high-quality devices. Our nanofabrication strategy provides high flexibility to control specific features of the Si nanopillar arrays as is the diameter, height and separation of the nanostructures at the bottom of the microfluidic channel. In contrast to conventional fabrication methods that integrate microfluidic interconnections after the fabrication of nanostructures[127,128], we have exploited the inert properties of the SU-8 polymer (e.g. resistant to HF/H_2O_2 solution) to outline before a microfluidic channel.

With this protocol we avoid the need to further align the nanopillar structures with microfluidic channel, reducing the chances of damaging their topography and integrity.

In particular, we report a summary of the first experiments from Si nanoholes to Si nanopillars on Si wafer by colloidal lithography (CL). Next, we describe the controlled fabrication of a lithographic gold mask within the SU-8 microchannel and the creation of Si nanopillar arrays via metal-assisted silicon etching. Furthermore, we experimentally demonstrated the strong influence of the UV/ozone pretreatment of samples, the H_2O_2/HF concentration, and design of the lithographic mask to speed up the formation of large-surface-area Si nanopillar arrays. Our fabrication strategy was used for rapid design and fabrication of Si master mold for the plasmo-mechanical sensor with integrated microfluidics.

2.2 Design of the silicon master mold of sensor

The first objective of the fabrication of the sensor is to create the suitable silicon master mold that can be replicated using polymers to produce the flexible nanopillars. We tested two routes, silicon nanoholes and nanopillars to find the most appropriate strategy to create them.

Silicon nanoholes and nanopillars were fabricated by the combination of colloidal lithography (CL), RIE treatment, e-beam evaporation, and metal-assisted chemical etching, to find the suitable methodology for the production of Si master of sensor. Charged colloidal beads are utilized, and the size distribution of fabricated nanostructures is largely determined by size dispersions of the masking colloids [28]. Fig. 2.1 shows not only the processes to achieve nanodisks and nanoholes but also the additional step of metal-assisted-chemical etching to produce Si nanoholes and nanopillars, respectively.

2.3 Silicon Nanoholes

The silicon nanoholes are a fast and easy route towards the creation the polymer nanopillars for the sensor whose depth corresponds to the height of the polymer structures. Ordered arrays of Au nanodisks were fabricated by hole-mask colloidal lithography (HCL)[28]. Firstly, the Si wafer was immersed in boiling piranha solution [H_2O_2: H_2SO_4 1:3] for 1 hr at 80 °C in order to remove organic residues, rinsed several times with distilled water and dried with air. After drying the Si wafers with N_2, they were ready for the HCL process following for a metal-assisted chemical etching that result in the creation of Si nanoholes. The exact details of this lithography process are shown in Fig. 2.1a, and described in the following.

Materials

Si (100) wafer chips (p-type, 5-10 Ω-cm, Siegert wafer) with 279 µm thickness were employed. 4 wt % PMMA diluted in anisole, Mw=950000 from Microchem Corporation. Polydiallyldimethylammonium chloride (PDDA), Mw =400k-500k, Sigma-Aldrich, 0.2 wt % in Milli-Q water, poly(sodium-4-styrenesulfonate) (PSS) and diallyl-dimethyl-ammonium chloride (DDA, Sigma-Aldrich, 348279-1L) were drop-coated on top of the Si wafer in order to create an adhesive layer on top of the latter. Polystyrene beads (sulfate latex, Invitrogen, 0.2 wt % in Milli-Q water) were used to form the ordered polystyrene bead array. Hydrogen peroxide

(30%), hydrofluoric acid (49%), and distilled water were used for the etching solution. Teflon holders were designed to submerge the wafers into the chemical solution.

A UV-ozone TipCleaner (TM) device (Bioforce, United States) was used to remove contaminants and to make the surfaces hydrophilic. A plasmalab 80 plus (Oxford instruments, UK) was utilized to remove the PMMA, and an e-beam evaporator (ATC ORION deposition system, United States) was employed to deposit the metals onto the Si wafer.

Process

1. Polystyrene Bead Deposition

First, an approximately 200 nm thick layer of PMMA was spin-coated (4000 rpm, 1000 $r \cdot s^{-2}$, 4 min) onto the clean surface and next a soft baking (120 ˚C, 5 min on hot-plate). The PMMA covered Si wafers were subjected to ultraviolet (U/V) ozone for 15 minutes, in order to increase the hydrophilicity of PMMA. Then, oppositely charged polyelectrolyte was drop-coated on top of the PMMA layer, in order to create an adhesive layer on top. For this purpose, a positively charged PDDA was used (60 s incubation time), followed by careful rinsing with de-ionized water in order to remove excess PDDA, and dried with N_2. As the last step, a colloidal solution containing polystyrene beads (D≈ 100 or ≈200 nm) was deposited, by a similar drop coating process (60 s incubation time), subsequently rinsing and drying the Si wafers with de-ionized water and N_2, respectively. The electrostatic repulsion between the polystyrene beads, in combination with the attractive force that exists between these beads and the PDDA layer, define the short range order polystyrene bead array, as can be seen in Fig. 2.1a, Step 1.

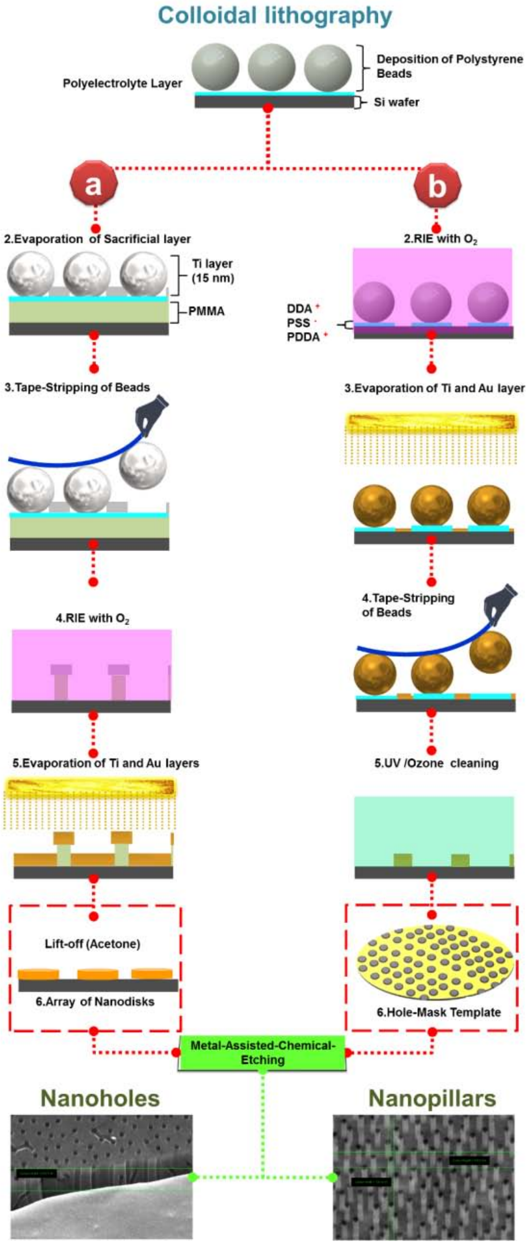

Figure 2.1. *Diagram illustrating the processes* **a** *and* **b***, and the resulting nanostructures produced by the combination of CL, RIE, E-beam evaporation and Metal-assisted Chemical Etching.* **a)** *nanodisks and nanoholes and* **b)** *nanoholes and nanopillars.*

2. Evaporation of the sacrificial layer

As a second step, the hole-mask template is created by depositing a sacrificial layer of Ti (15 nm) that is resistive to RIE with oxygen. After, the polystyrene beads are tape-stripped away, as shown in Fig. 2.1a, Step 2 and 3, resulting in a mask with holes arranged in a pattern determined by the self-assembled colloidal beads.

3. RIE treatment

Next, an RIE treatment (3 min, 75 W, 75 mTorr, at a flow rate of 21 sccm) is applied in order to remove the exposed polymer (PMMA/PDDA) underneath the holes that are perforated in the sacrificial Ti layer, see Fig. 2.1a, Step 4.

4.Disk evaporation and Lift-off

As a fourth step, using e-beam evaporation, first a metal adhesion layer was deposited (15 nm Ti). Next, a 19 nm thick Au film was evaporated at 1.0 $\text{Å}\cdot s^{-1}$, creating the resulting Au nanodisks, see Fig. 2.1a, Step 5. Subsequently, the remainder of the hole-mask was removed by a lift-off process, carried out in acetone at room temperature (Fig. 2.1a, Step 6). The Au nanodisks diameters, its corresponding diameter side distribution, and inter-disk separations are entirely governed by the properties of the colloidal polystyrene beads solution. Fig. 2.2 shows a SEM image with the random distribution of the Au nanodisks.

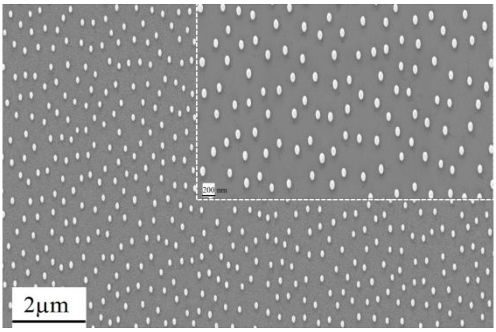

Figure 2.2. *SEM image of random distribution of fabricated nanodisks.*

5. Metal-Assisted Chemical Etching

As a final step, the Si wafers were immersed in an etching mixture consisting of 18 ml HF (49%): 5 ml H_2O_2 (30%): 77 ml H_2O, at room temperature in clean room facilities. The etching process was stopped by removing the Si wafers from the chemical solution and immersing them in distilled water for 20 minutes.

2.3.1 Results and Discussion

The concentration of H_2O_2 and HF, and the etching time were varied to study their influence on the etching rate and the morphology of the etched nanoholes. Fig. 2.3 shows focused ion beam (FIB-SEM) images of the structural changes observed in the Si nanoholes employing different etching times. As described in the section 1.4.3, in a typical metal-assisted chemical etching procedure, the Si beneath the noble metal is etched much faster than the Si without noble metal coverage. As a result, the noble metal (nanodisk) sinks into the Si substrate, generating pores in the Si substrate or Si nanoholes.

As observed in Fig. 2.3 the nanodisks not only sank into the Si substrate but also displaced, as a result, the original distribution of the nanoholes was altered. This disorder increased with respect to etching time. Cross-sections were done by FIB to characterize the nanoholes (e.g., depth, diameter). Unfortunately, this technique altered the nanoholes dimensions, providing misleading measurements. We could conclude that Si nanoholes were not the best option for our master mold for the projected sensor. Although the process is simple, the poor outcome in term of quality and the order of the nanoholes were not enough to ensure reproducibility over the fabrication; also the characterization of the nanostructures is very difficult by FIB see Fig. 2.3c.

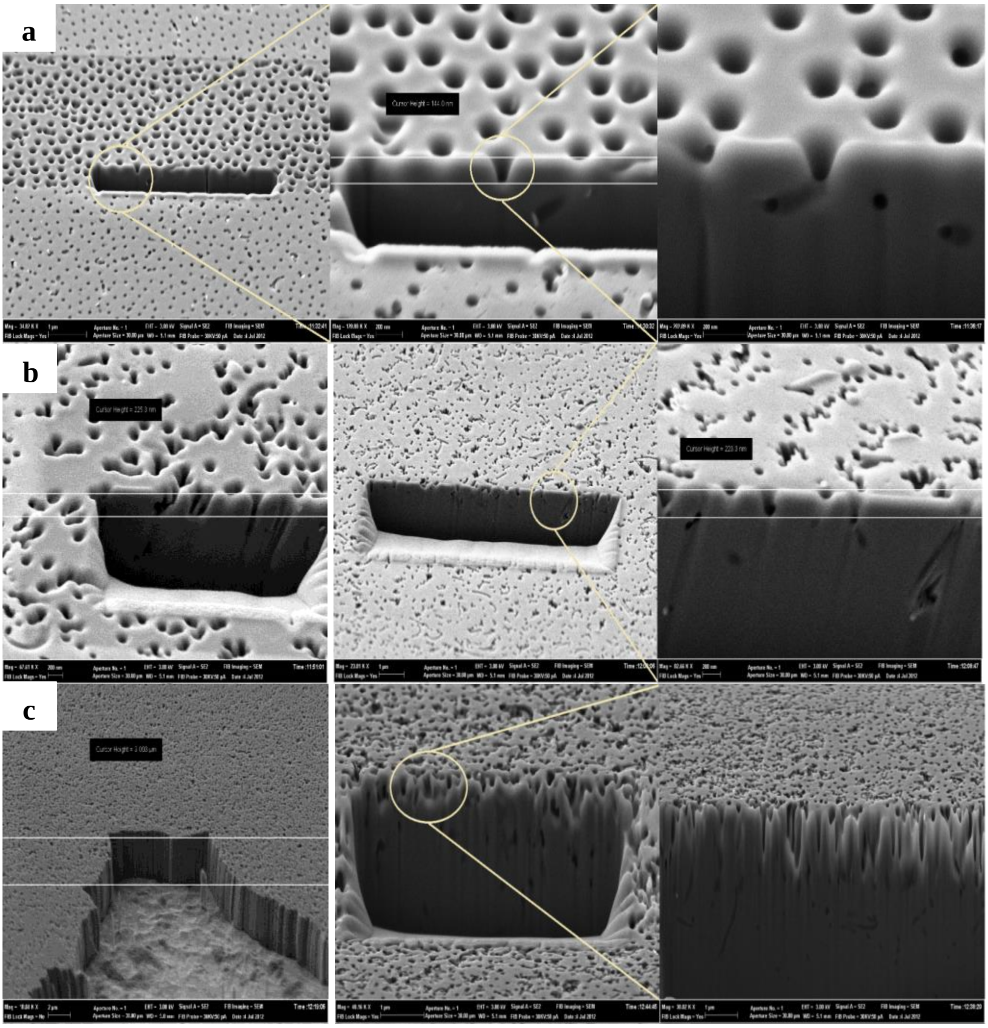

Figure 2.3. *FIB-SEM images of Si nanoholes. The nanoholes were created by an etching solution containing HF/*H_2O_2*/*H_2O*=18/5/77 ml, at different etching times,* **a)** *3 min,* **b)** *5 min and* **c)** *10 min, respectively.*

2.4 Silicon Nanopillars

Si nanopillars were fabricated by colloidal lithography[28] as a second route towards the creation of the silicon master mold. Firstly, the Si wafer was immersed in boiling piranha solution [H_2O_2: H_2SO_4 1:3] for 1 hr at 80 °C to remove organic residues, rinsed several times with distilled water and dried with air. After drying the Si wafers with N_2, they were ready for the CL process following a metal-assisted chemical etching that result in the creation of Si nanopillars. The exact details of this process are shown in Fig. 2.1b, and described in the following.

Process

1.Polystyrene Bead Deposition

First, polyelectrolytes (PDDA, PSS, DDA) were drop-coated on top of the Si wafer in order to create an adhesive layer on top (60 s, incubation time), followed by careful rinsing with de-ionized water in order to remove excess of them, and dried with N_2. As the last step, a colloidal solution containing polystyrene beads (D≈100 nm or ≈200 nm) was deposited, by a similar drop coating process (60 s incubation time), subsequently rinsing and drying the Si wafers with de-ionized water and N_2, respectively. See Fig. 2.1b, Step 1.

2. RIE treatment

Next, a RIE treatment (75 W, 75 mTorr, at a flow rate of 21 sccm) was applied in order to remove the adhesive layer of the zones exposed to UV/ozone, see Fig. 2.1b, Step 2.

3. Evaporation of Ti and Au

Using e-beam evaporation, the mask template is created by depositing a thin film of Ti and Au (Fig. 2.1b, Step 3). After, the polystyrene beads are tape-stripped away, as shown in Fig. 2.1b. Step 4, resulting in a gold mask with nanoholes arranged in a pattern determined by the self-assembled colloidal beads. Fig. 2.4 shows the SEM image of a gold mask with nanoholes.

4. UV/Ozone cleaning

The Au mask with nanoholes was then exposed to UV/ozone for 15 minutes to remove the contaminants from the mask surface (Fig. 2.1b, Step 5) and produce a clean, hydrophilic and oxidized gold mask with nanoholes.

5. Metal-Assisted Chemical Etching

As described in section 1.4.3, in a typical metal-assisted chemical etching procedure, the Si beneath the noble metal is etched much faster than the Si without noble metal coverage. As a result, the noble metal sinks into the Si substrate, generating Si nanopillars. Then, the Si wafers were immersed in an etching mixture consisting of HF (49%):H_2O_2 (30%):H_2O, at room temperature in clean room facilities. The etching process was stopped by removing the Si wafers from the chemical solution and immersing them in distilled water for 20 minutes.

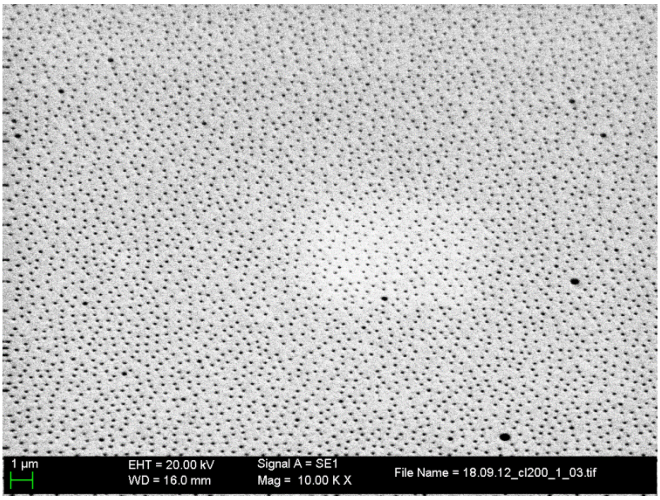

Figure 2.4. *SEM image of random distribution of nanoholes.*

2.4.1 Results and Discussion

To understand the influence of each parameter on the fabrication of the Si nanostructures, several experiments were performed. Then, the diameter distribution and inter-hole separations were adjusted. The properties of colloidal polystyrene bead solution and the polyelectrolytes; the time of reactive ion etching treatment, and the influence of the noble metal were tested. Also, the concentration of etchant (HF/H_2O_2) and the time of the etching process were varied. Table 2.1 shows the most representative experiments that were tested to create Si nanopillars, the structural results are shown in Fig. 2.5.

Figs. 2.5a,b, clearly show that the concentration of etching solution (H_2O_2/HF) affects not only the etching rate but also the morphologies of the nanopillars producing a tip-clumped shape with large bending (hooked) nanopillars. Also, the decrease of the polyelectrolyte layer results in short, highly tapered nanopillars (Fig. 2.5d) which are collapse towards the bottom surface when the concentration is high (Fig. 2.5c). The etching time and periodicity are key parameters which must be finely controlled; they are responsible of the height of vertical nanopillars. Fig. 2.5e shows how the simple modification of the periodicity and a long etching time can produce similarly hooked morphology whereas short periods of etching time can produce small and vertically nanopillars (Fig. 2.5f). Even with only an inappropriate changing of the periodicity of the Si nanoholes, it is sufficient to alter the manufacture of the nanopillars, producing unstable and inhomogeneous structures (Figs. 2.5 g,h).

In a typical metal-assisted chemical etching procedure, the function of the metal is to catalyze the reduction of hydrogen peroxide (H_2O_2) which delivers electronic holes necessary for the oxidation and the subsequent dissolution of the Si oxide by HF. Silver (Ag) is also frequently used as the noble metal. Fig. 2.5i shows the morphologies of etched structures with Ag, deposited under the same conditions that Au via e-beam evaporation. The results confirm that the morphologies of the etched structures vary with the type of noble metal, also that it influences the etching rate. According to our results, the rate of etching assisted by Ag was much faster than assisted by Au. Moreover, the structures on substrates etched in the presence of Ag were usually surrounded by a porous layer. Similar results were obtained even increasing the thickness of the Ag film (Fig. 2.5j).

Table 2.1. *Experiments focus on to understand and to control the Si nanopillar fabrication by Cl . See Fig. 2.5*

	1.Colloidal Lithography	2.RIE-Oxygen	3.Evaporation	5.Ozone	6.Attack HF	Time
a	D= 200 nm (0.2 %) DDA (2 %) PSS (2 %) PDDA (2 %)	15s	1 nm Ti,19 nm Au	15 min	H_2O_2 = **10** ml HF=20 ml H_2O=70 ml	2
b	D= 200 nm (0.2 %) DDA (2 %) PSS (2 %) PDDA (2 %)	15s	1 nm Ti,19 nm Au	15 min	H_2O_2 = 5 ml HF=20 ml H_2O=75 ml	2
c	D= 200 nm (0.2 %) DDA (2 %)	**30s**	1 nm Ti,19 nm Au	15 min	H_2O_2 = 10 ml HF=20 ml H_2O=70 ml	2
d	D= 200 nm (**.2** %) DDA (2.0 %)	**30s**	1 nm Ti,19 nm Au	15 min	H_2O_2 = 5 ml HF=20 ml H_2O=75 ml	2
e	D= 200 nm (**.04** %) DDA (2.0 %)	**30s**	**0.5 nm Ti**,19 nm Au	15 min	H_2O_2 = 2 ml HF=18 ml H_2O=80 ml	20
f	D= 200 nm (**.04** %) DDA (2.0 %)	**30s**	**0.5 nm Ti**,19 nm Au	15 min	H_2O_2 = 2 ml HF=18 ml H_2O=80 ml	10
g	D= 100 nm (**.02** %) DDA (2.0 %)	**30s**	**0.5 nm Ti**,19 nm Au	15 min	H_2O_2 = 2 ml HF=18 ml H_2O=80 ml	20
h	D= 100 nm (**.02** %) DDA (2.0 %)	**30s**	**0.5 nm Ti**,19 nm Au	15 min	H_2O_2 = 2 ml HF=18 ml H_2O=80 ml	10
i	D= 200 nm (**.04** %) DDA (2.0 %)	**30s**	**0.5 nm Ti**,19 nm Ag	15 min	H_2O_2 = 2 ml HF=18 ml H_2O=80 ml`	20
j	D= 100 nm (**.2** %) DDA (2.0 %)	**15s**	**0.5 nm Ti,25 nm Ag**	15 min	H_2O_2 = 2 ml HF=18 ml H_2O=80 ml`	10
k	D= 100 nm (**.04** %) DDA (2.0 %)	**15s**	**0.5 nm Ti**,19 nm Au	15 min	H_2O_2 = 2 ml HF=18 ml H_2O=80 ml`	5
i	D= 100 nm (**.2** %) DDA (2.0 %)	**15s**	**0.5 nm Ti**,19 nm Au	15 min	H_2O_2 = 2 ml HF=18 ml H_2O=80 ml`	5

As expected, the shape and spacing of the nanoholes in the metal mask strongly influence the etching rate, then under appropriate conditions, the gold mask with well-ordered nanoholes results in well-defined Si nanopillars, as shown in the Fig. 2.5k. Nevertheless, this elegant technique of fabrication can be affected not only by inappropriate parameters of fabrication and defects of the lithography but also by contamination. Fig. 2.5l shows well-ordered Si nanopillars with a variation of height induced by a defect of the fabrication in the gold mask. Then, under correct parameters, the Si nanopillars with height gradients can be generated by an alteration on the catalytic mask as confirming the Figs. 6a,b[64]. According to the aforementioned results, the Si nanohole arrangement of the catalytic mask strongly effects on the etching rate and the morphology of the nanopillars. As above described, the nanoholes in the Au film, their corresponding diameter, distribution, and separations are entirely governed by the properties of the colloidal polystyrene beads solution. As a consequence, the Au nanohole arrangement is random and this complicates the reproducibility of the experiments. Also, the cleaning of the gold mask by UV/ozone (Fig.2.1b, Step 5) was not controlled, and several experiments failed in the etching process due to remains of polyelectrolytes.

We could conclude that Si nanopillars were the best option to fabricate the Si master mold of the sensor. However, the methodology had to be improved in order to control the arrangement of the Si nanopillars. According to our best results, under controlled conditions, low concentration of the etching solution (HF/H_2O_2), short etching times, and gold as the noble metal, it could be possible to produce vertically nanostructures. But an inappropriate variation of them, defects or contamination can result in inhomogeneous structures. Therefore, these parameters had to be deeply studied before stabilization of the fabrication procedure. An alternative approach is nanosphere lithography (NSL) which employs organized 2D colloidal crystals with a hexagonal close-packed array. This method enables the facile production of large areas (cm^2) of nanoscopic features like nanoholes in a thin film. To overcome the previous challenges, the new nanofabrication strategy was based on a lithographic gold mask with a hexagonal array, instead of a random distribution, that combines NSL, reactive ion etching treatment and e-beam evaporation technique to control the position and diameter of the nanopillars. Meanwhile, the height of the SiNPs heavily depends on a well-controlled metal-assisted silicon etching protocol.

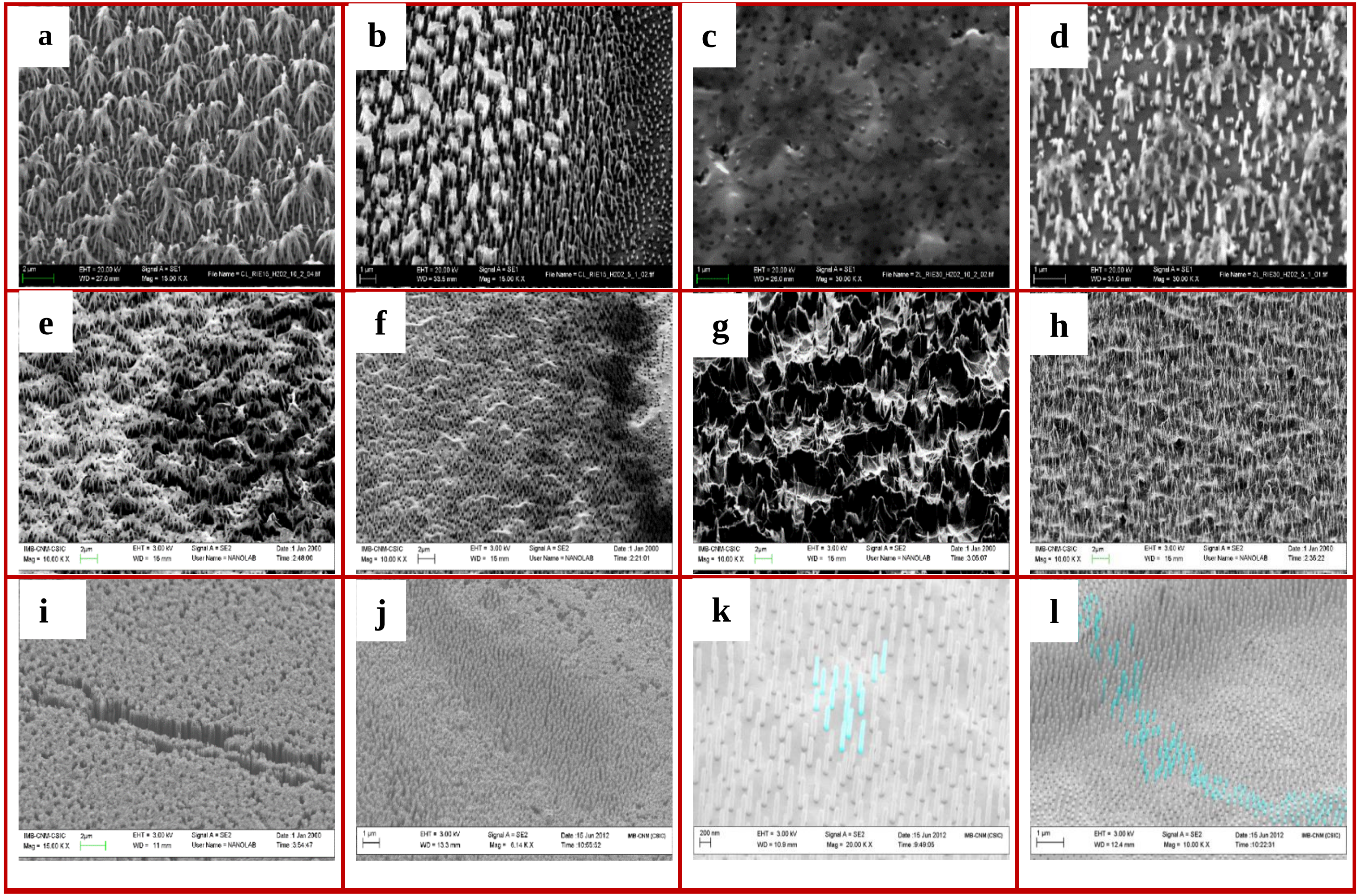

Figure 2.5. *SEM images of different Si nanopillar testing the parameters that influences in the fabrication process.*

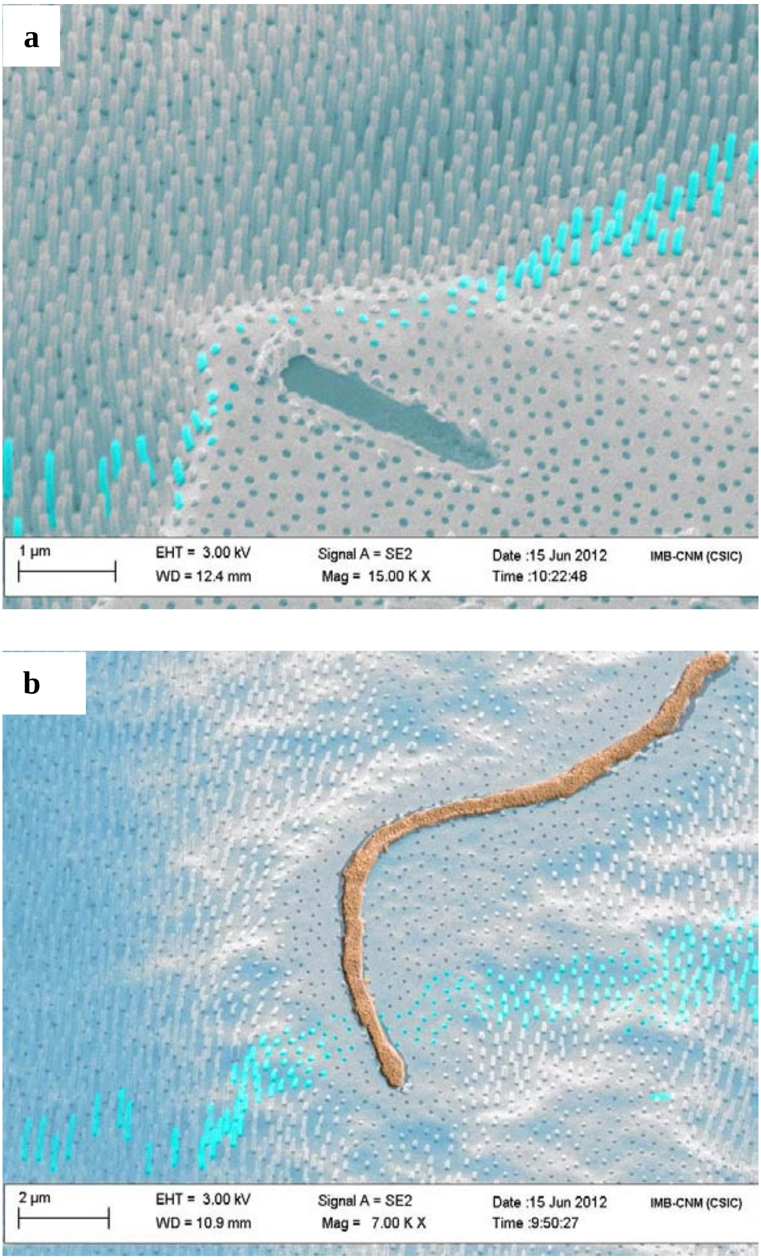

Figure 2.6. *SEM imagen of Si nanopillars with height gradient produced by defects of fabrication. a) Si nanopillars with different heights created by a scratch of tweezers. b) The variation of the height of Si nanopillars was produced by a fiber of cleanroom wipers.*

2.5 Well-Ordered Si Nanopillars Embedded in a Microchannel

Fabrication of the silicon master

The fabrication technique is based on the development of a SU-8 microfluidic channel using photolithography to place well-ordered, high-aspect-ratio silicon nanopillars (SiNPs) inside the microchannel. The fabrication flow includes three main steps: **(1)** fabrication of the microfluidic channel by photolithography, **(2)** preparation of a lithographic Au mask and **(3)** fabrication of SiNPs by metal-assisted-chemical etching of silicon. The steps are described in Fig. 2.7.

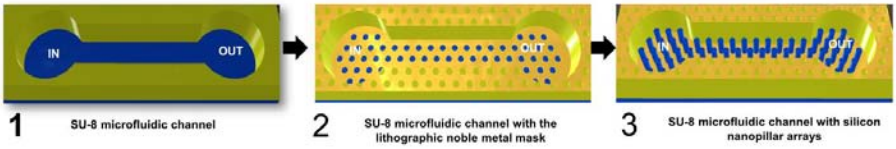

Figure 2.7. *Overview of the fabrication process of a silicon master mold to build the optical and mechanical nanosensor.*

2.5.1 Fabrication of microfluidic channels by photolithography

Materials

Commercially available SU-8 2025 negative epoxy photoresist and a methoxy-2-propanol acetate developer (Microchem Corp, United States) were used. Si (100) wafer chips (p-type, 5-10 Ω-cm, Siegert wafer) with 279 µm thickness were employed. The photomask was designed using CorelDRAW X5 and a Süss-Microtech MA 1006 Mask Aligner was used for the UV exposition. The thickness of the layer was measured by a Profilometer KLA-Tencor P15.

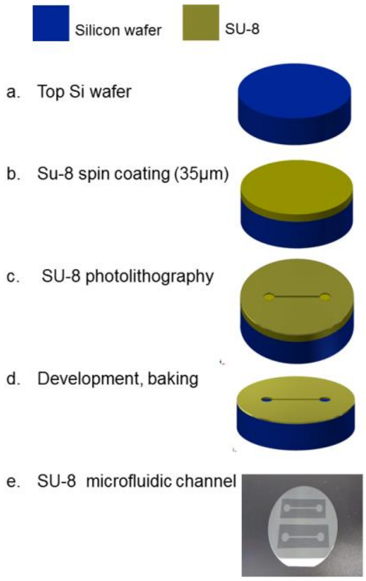

Figure 2.8. *Photolithograpic steps with the negative photoresist SU-8. The picture at the bottom shows SU-8 channels 20 mm long and 1mm wide, with reservoirs of 5 mm of diameter.*

Process

In order to remove any imperfections that can affect the quality of the spin coating process, the wafer was cleaned as follows. Firstly, the wafer was immersed in boiling piranha solution [H_2O_2: H_2SO_4 1:3] for 1 hr at 80 °C to remove organic residues, rinsed several times with distilled water and dried with air. The Si wafer was then dehydrated in an oven at 200 °C for 30 minutes to improve the adhesion of the SU-8 film (Fig. 2.8a). As follows, 2.5 ml of SU-8 were dispensed onto the center of the wafer using a syringe (Fig. 2.8b). To minimize the presence of bubbles, which is a common problem when depositing SU-8 onto a wafer, the resin was allowed to stand overnight inside the syringe. The wafer was spanned using the parameters shown in Table 2.2 to obtain a thin and uniform layer of about 35 µm. Afterward, a soft-baked of the wafer was done to remove solvents and to improve adhesion of layers. This process was performed in three different steps on a hot-plate to avoid film shrinkage: step 1 at 65 °C for 5 minutes, step 2 at 95 °C for 3 minutes and step 3 at 65 °C for 5 minutes.

Table 2.2.*Parameters of SU-8 spin coating process* (*~35 µm*)

Factor	**Level 1**	**Level 2**
Speed	600 rpm	3000rpm
Acceleration	600 rpm s^{-1}	600 rpm s^{-1}
Time	10 s	40s

In order to ensure good adhesion between the wafer and the SU-8 film, crosslinking control was required. The microchannel was patterned by soft contact photolithography with the photomask design and using an energy dosage of 150 - 215 (mJ/cm^2) for 40 s according to the thickness of the SU-8 film (~35 µm) (Fig. 2.8c). A post-exposure bake of the wafer improve the crosslinking degree and stabilized the irradiated areas for the development step. The SU-8 resin was developed by immersing the wafer in metroxy-2-propanol acetate for 5 minutes at room temperature, rinsed with isopropanol and dried with air. Finally, a hard bake step was performed at 150 °C for 10 minutes on a contact hot plate to harden the photoresist, see Fig. 2.8d. The final thickness of the microchannel was measured with a profilometer. Measurements of the resin thickness were taken from 20 samples at 5 different locations across the width of the channel in order to obtain the SU-8 average thickness and standard deviation value (StD). The average thickness was ~34.08 µm with StD of 1.59 (Fig. 2.8e). A schematic of the whole process is shown in Fig. 2.8.

2.5.2 Catalytic metal mesh preparation

Materials

Commercially available polystyrene spheres (carboxyl latex beads, 4% w/v) of 400 nm and 300 nm diameter and ethanol absolute were used to prepare a PS solution (1 ml) at 1:1. Surfactant Triton-100 was also used to compact the monolayer and a Gilson Minipuls 3 Peristaltic Pump was used to drain the water. A plasmalab 80 plus (Oxford instruments, UK) was utilized to reduce the diameter of the spheres and an e-beam evaporator (ATC ORION deposition system) was employed to deposit the gold on the Si wafer with the SU-8 microfluidic channel.

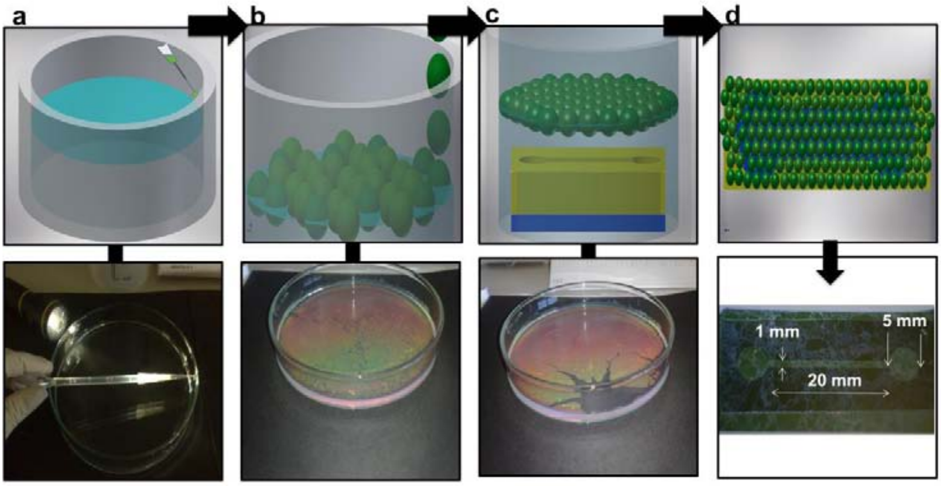

Figure 2.9. *Schematic illustration and photos describing the procedure of lithography.* **(a)** *Position of the Pasteur pipette on the wall of a Petri dish with 13.5 cm of diameter in order to slip the spheres into the water surface.* **(b)** *Nanopheres of 400 nm of diameter covering 90% of the water surface. The inset shows the diffraction pattern made upon the illumination of the mask with a lamp.* **(c)** *PS monolayer compacted and separated from the glass wall.* **(d)** *PS monolayer deposited and adjusted on the SU-8 microchannel.*

Process

In our study, a hydrophilic petri dish was filled with Mili-Q water and 0.25 ml of PS solution were taken using a Pasteur pipette to slip the spheres onto the water surface (Fig. 2.9a). The transfer of the spheres into the container was stopped when the monolayer covered about 90 % of the water surface (Fig. 2.9b). The monolayer was formed by recrystallization after 1.5 hr. Then, the monolayer was compacted and separated from the petri dish walls by inserting a wetted needle with triton X-100. Finally, the microfluidic channels were submerged into the water and aligned under a PS monolayer (Fig. 2.9c). The water was then drained slowly by the pump, until the monolayer was deposited on the Si wafer with the microchannels and the rest of the water evaporated overnight (Fig. 2.9d).

Among the advantages offered by the SNSL technique, besides the selection of the sphere size, is that the PS spheres can be further tailored by using annealing-induced deformation through temperature or by diameter reduction using RIE treatment. In our study, the PS monolayer was modified by a combination of the aforementioned processes. Thus, the spheres were heated at 100 °C for 15 s on a hot-plate to compact them (Figs. 2.10a,b). Meanwhile, the diameter of the spheres was reduced by RIE treatment (Fig. 2.10c). The source gas used in the RIE experiments was oxygen at a flow rate of 21 sccm, pressure of 150 mTorr and RF power of 75 W. The diameter of the PS spheres was reduced to the desired value by varying the duration of the etching time (Fig. 2.10d).

In metal-assisted chemical etching, gold is one of the most frequently employed noble metals due to its high stability during the chemical etching process, and because it can be easily deposited by e-beam evaporation[49,82]. Accordingly in our study, a titanium film of 0.5 nm thick, and a gold film of 19 nm thick were deposited onto the Si wafer surface that contained the microfluidic channels and the etched spheres (Figs. 2.10d,e) The titanium was used to improve the adhesion of the gold film to the silicon area. Finally, the PS spheres were removed using an ultrasonic bath with ethanol absolute for 1 min to generate the gold mesh inside the microfluidic channel (Figs. 2.10f,g).

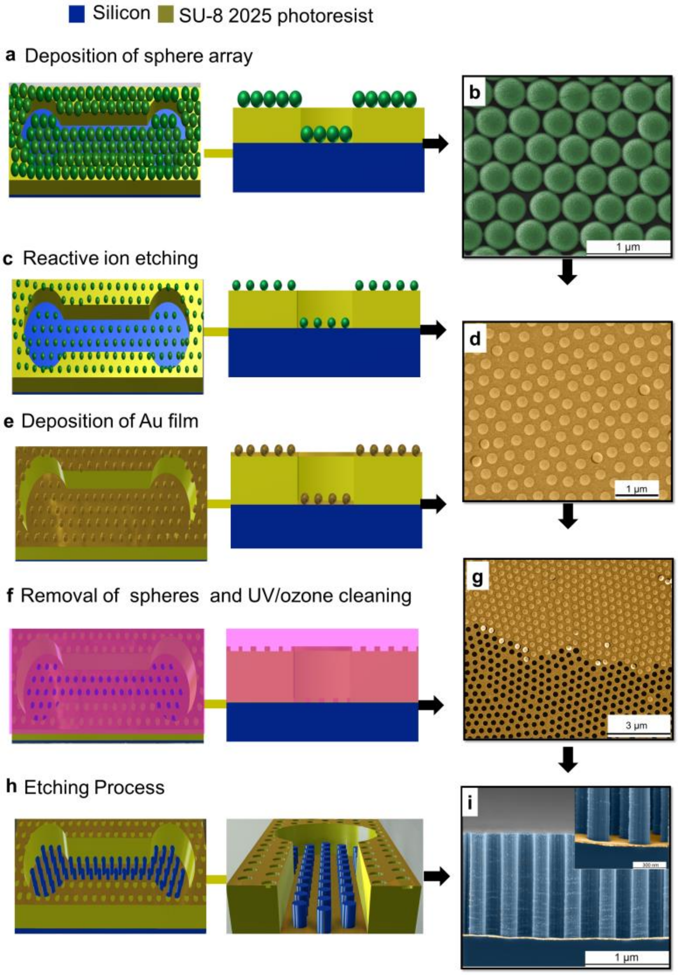

Figure 2.10. *Schematic illustration of the experimental procedure for fabricating large-area arrays of silicon nanopillars in microfluidic channels.* **(a)** *Deposition of PS sphere monolayer in the microfluidic channel.* **(b)** *SEM image of the PS sphere monolayer* (D = 400 nm) *on the microchannel.* **(c)** *Size reduction of the sphere by RIE.* **(d)** *SEM image of PS spheres etched by RIE at 150 mTorr and 75 W, with reduced diameter of 200 nm after an etching time of 100 s.* **(e)** *Deposition of Ti and Au layers on the microchannels with reduced spheres. The titanium was used to stick the gold film to the silicon area.* **(f)** *Removing the spheres by ultrasonication and UV/Ozone cleaning of the gold mask.* **(g)** *SEM image of the gold mesh produced in the microchannel when the spheres are removed.* **(h)** *Cross-sectional scheme of the formation of Si nanopillars in the SU-8 microfluidic channel by catalytic etching.* **(i)** *Cross-sectional SEM image of vertically aligned and ordered Si nanopillars in the microfluidic channel produced after 10 min of etching.*

2.5.3 Fabrication of SiNPs by metal-assisted chemical etching

Materials

A UV-ozone TipCleaner (TM) (Bioforce, United States) device was used to remove contaminants over the gold masks of the microchannels and to make the surface hydrophilic. Hydrogen peroxide (30%), hydrofluoric acid (49%) and distilled water were used as etchant solutions. Four Teflon holders were designed to submerge the microchannels into the chemical solution, and to remove the gold film using potassium iodide (KI).

Process

In order to remove any hydrocarbon contaminant from ambient air conditions, the microfluidic channels with the gold masks were cleaned by ultraviolet (U/V) ozone for 20 minutes to produce clean, hydrophilic and oxidized surfaces[129]. The microchannels were then rinsed with isopropanol for 15 minutes and dried under N_2 (Figs. 2.10f,g). Afterward, for the fabrication of SiNPs by metal-assisted chemical etching the microchannels were placed in Teflon holders and immersed simultaneously in an etching mixture consisting of ($HF(49\%):H_2O_2(30\%):H_2O=6:1:26$:v:v:v) at room temperature in Clean Room facilities. The etching duration was varied, depending on the required length of the SiNPs. The etching process was stopped by removing the microchannels from the chemical solution and immersing them in distilled water for 20 minutes (Figs. 2.10h,i). Thereafter, the microchannels were immersed in KI solution for 2 minutes to remove the gold film, and rinsed with distilled water (15 minutes) and isopropanol (15 minutes) to minimize capillary effects during N_2 drying. Experimental photos of the whole process are shown in Fig. 2.11

Figure 2.11. *Photos describing the procedure of metal-assisted chemical etching to create the Si nanopillars at Clean Room facilities.*

2.6 Results and discussion

2.6.1 Hexagonal arrays of Si Nanopillars: PS nanosphere monolayer

Figs. 2.12 a,b show the final monolayer formed by the recrystallization of spheres with ~400 nm in diameter. The monolayer was deposited and adjusted on the microfluidic channel covering it completely. The SEM image in Fig. 2.12c clearly shows the hexagonal array of PS spheres homogenously distributed. Defects in the monolayer, such as disorders in the hexagonal arrangement of PS spheres and overlapping were transferred into the Si nanopillars array. These defects could be reduced by improving the control of the sphere deposition to form the monolayer on the water surface and by compacting the spheres as best as possible. Moreover, other imperfections resulted from different initial sphere size. For instance, Fig. 2.12d shows the distribution of the diameters of the spheres of 400 nm. The mean diameter of the sphere was ~390.04 ± 26.16 nm which matched well with the size provided by the company (390 nm).

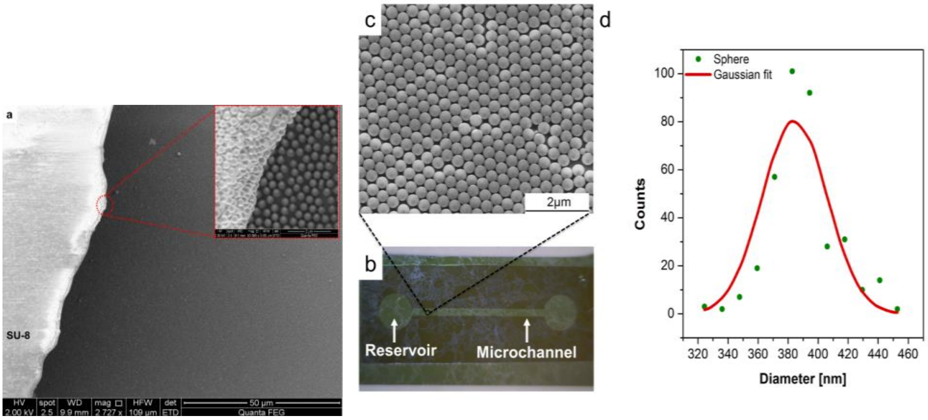

Figure 2.12. *PS 400 nm monolayer on a SU-8 microfluidic channel fabricated by SNSL.* **(a)** *SEM image of the monolayer deposited and adjusted on the microfluidic channel* **(b)** *Photo showing the PS mask covering the entire SU-8 microfluidic channel.* **(c)** *SEM image of the PS sphere array in the SU-8 microfluidic channel with some defects (top view, scale bar =2 µm).* **(d)** *Size distribution of spheres with diameters with a mean value of 390.04 ± 26.16 nm.*

2.6.2 Etched polystyrene masks within microchannel by RIE

It has been reported that the LSPR spectral position and magnitude strongly depend on the composition, local dielectric environment, geometry, size, and separation distance of nanostructures[32]. Therefore, we used RIE etching process to set the diameter of the Si nanopillars, and consequently to control the radius and position of the nanostructures. The spheres deposited on the microfluidic channel were etched by RIE with oxygen for a period of 30-120 s. The characterization of the results was performed by SEM images taken at 4 different locations left; right, up and down in order to obtain the average diameter and the StD value, see Figs.2.13 a,b. The graph in Fig. 2.13c shows the reduced diameter of the 300 nm and 400 nm PS spheres according to the RIE time. While the RIE of both PS 300 nm and PS 400 nm increased over time, the reduction of the PS 300 nm spheres was faster. At 100 s, the 300 nm spheres were completely etched, whereas the diameter of the 400 nm spheres was reduced to ~207.65 nm.

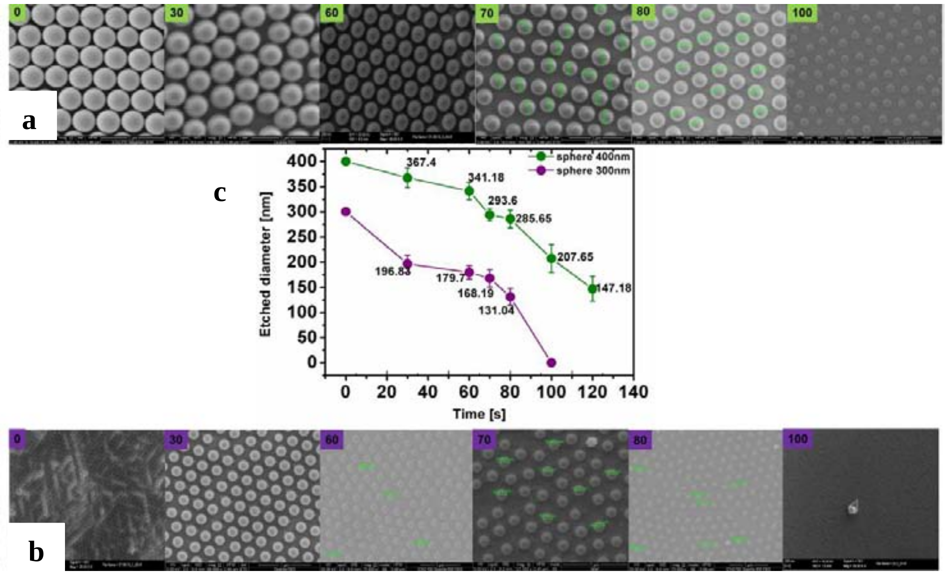

Figure 2.13. *PS spheres in microfluidic channels etched by RIE with a flow of 21%, 75 W and 150 mTorr.* (a) *and* (b) *SEM images of PS 300 and 400 nm masks exposed to RIE, respectively.* (c) *Data plotted on the basis of measurements acquired from SEM images of the reduced diameters of PS spheres of 300 nm and 400 nm of diameter during 120 s of RIE.*

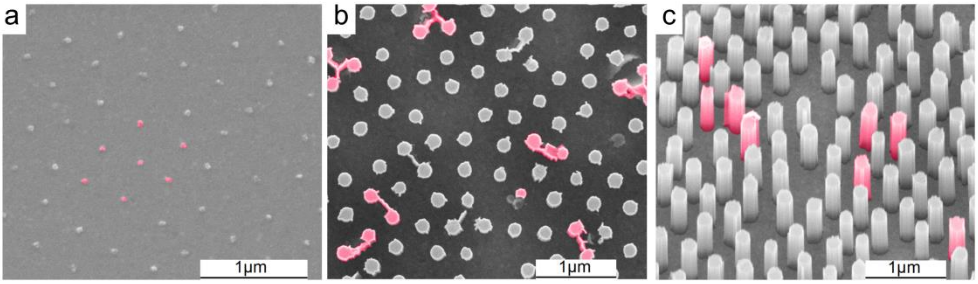

Figure 2.14. *Defects presented during the nanofabrication of SiNPs.* (a) *PS 400 nm monolayer in a SU-8 microfluidic channel is damaged by an excessive RIE time of 145 s where the nanospheres lost quality in the spherical shape and order (top view, scale bar= 1 µm).* (b, c) *Top view of deformed SiNPs produced by an excessive time of RIE of 120 s.* (c) *Imperfect hexagonal arrays of SiNPs caused by defects in the PS monolayer and by an inadequate RIE treatment (15° tilt view, scale bar= 1 µm).*

According to our experiments, excessive RIE time can affect the quality and arrangement of the reduced nanospheres producing imperfect SiNPs (Fig. 2.14). The differences in diameter values can be explained by the variations in size of the original spheres and by the quality of the equipment used in the RIE treatment.

2.6.3 Height of Silicon Nanopillars

2.6.3.1 Effect of HF/H_2O_2 ratio

For a better control of the size and spacing of the SiNPs placed inside the SU-8 microfluidic channel, we have employed the nanosphere lithography technique. Using this approach combined with reactive ion etching and e-beam, the density, position and diameter of the SiNPs are well defined, thus, we were able to overcome the main challenges described in Section 2.4.1, with respect to the periodicity, shape, and spacing of the Si nanoholes in the gold mask that strongly influenced on the etching rate. In this Section, the diameter (2r) is kept at ≈ 207.65±27.60 with a center-to-center distance (d_{cc}) of 400 nm, and the height is controlled by HF/H_2O_2 ratio and etching time.

Effect of HF/H2O2 ratio

Table 2.3. *Experimental conditions for fabricating SiNPs. Compositions of etching solutions used in this study with volume in mL (volumes of 49% HF and 30% H_2O_2) with a total volume of 100 ml*

	1.SNSL	2.RIE	3.Evaporation	5.Attack HF	Etching Time
a	500 µl PS spheres (400nm) 500 µl ethanol	100s	0.5 nm Ti,19 nm Au	H_2O_2 = 3ml HF=18ml, H_2O=79 ml	2.5 min
b	500 µl PS spheres (400nm) 500 µl ethanol	100s	0.5 nm Ti,19 nm Au	H_2O_2 = 5 ml HF=18 ml H_2O=77 ml	2.5 min
c	500 µl PS spheres (400nm) 500 µl ethanol	100s	0.5 nm Ti,19 nm Au	H_2O_2 = 3 ml HF=18 ml H_2O=79 ml	5 min
d	500 µl PS spheres (400nm) 500 µl ethanol	100s	0.5 nm Ti,19 nm Au	H_2O_2 = 5 ml HF=18 ml H_2O=77 ml	5 min
e	500 µl PS spheres (400nm) 500 µl ethanol	100s	0.5 nm Ti,19 nm Au	H_2O_2 = 3 ml HF=18 ml H_2O=79 ml	7.5 min
f	500 µl PS spheres (400nm) 500 µl ethanol	100s	0.5 nm Ti,19 nm Au	H_2O_2 = 5 ml HF=18 ml H_2O=77ml	7.5 min
g	500 µl PS spheres (400nm) 500 µl ethanol	100s	0.5 nm Ti,19 nm Au	H_2O_2 = 3 ml HF=18 ml H_2O=79 ml	10 min
h	500 µl PS spheres (400nm) 500 µl ethanol	100s	0.5 nm Ti,19 nm Au	H_2O_2 = 5 ml HF=18 ml H_2O=77 ml	10 min

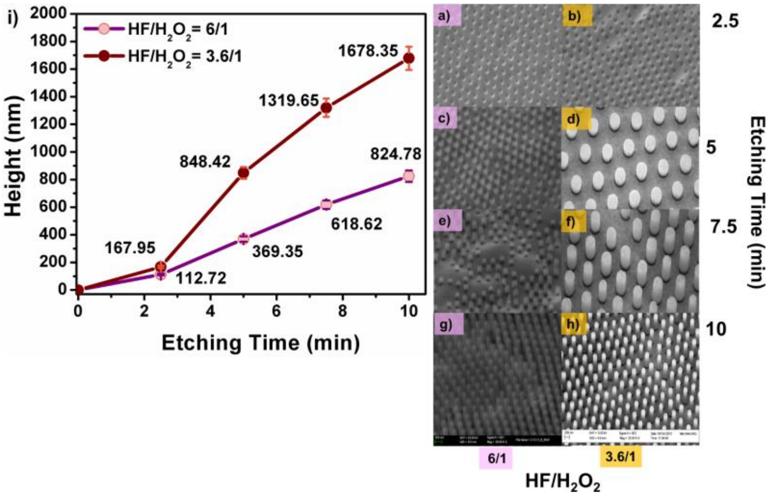

Figure 2.15. *Temporal evolution of SiNPs during the etching process for different HF/H_2O_2 ratios.* $HF/H_2O_2/H_2O$ =(a,c,e,g) *6/1/26 and* (b,d,f,h) *3.6/1/15.4. Each row indicates the etching time 2.5, 5 , 7.5 and 10 min respectively (43°tilt view, scale bar=200 nm).*

Table 2.3 shows the most representative experimental conditions that were tested to fabricate the SiNPs. It is important to note, that these experiments skip the step of UV/Ozone cleaning of the gold mesh (see Fig. 2.10). Figs. 2.15 a-h show the structural changes in SiNPs with respect to the HF/H_2O_2 ratio during the metal-assisted chemical etching. Based on the observed dependence of the Si nanopillar height on the relative ratio of HF and H_2O_2, the height results in the Figs. 2.15 a-h were plotted as shown in Fig. 2.15i. As shown in Fig. 2.15i, the height SiNPs are observed to be longer with increasing H_2O_2 concentration. It must be noted that the tip-clumped shape with large bending (hooked) SiNPs were not produced. Specifically, while there is not bending of pillars during formation under low H_2O_2 concentration (Fig. 2.15g), even higher SiNPs (<1678.35 nm) are vertical with increasing H_2O_2 concentration (Fig. 2.15h). It has been reported that in a typical metal-assisted chemical etching procedure, the function of the metal is to catalyze the reduction of hydrogen peroxide (H_2O_2) which delivers electronic holes necessary for the oxidation and the subsequent dissolution of the Si oxide by HF. Then, according with our results most of the injected holes are consumed by Si dissolution at the Au/Si interface, giving rise to the vertical shape (Figs. 2.15a-h). Increasing volumes of $H_2O_{2,}$ that is, increasing the hole injection can accelerate the etching rate and as a result the height SiNps are ≈50 % higher, see Fig. 2.15i.

2.6.3.2 Effect of UV/ozone on the etching process

In this fabrication protocol, we found that the cleaning of gold mesh in the microchannels by UV/ozone strongly influenced the etching process. In order to demonstrate this effect, a simple experiment was performed. Eight samples formed by a lithographic gold mesh placed in a hydrophobic SU-8 microchannel (contact angle ~102.2 ± 0.19) were used. Their diameters (2r) were kept at ~280 nm with a center-to-center distance (d_{cc}) of 400 nm. Four samples were then exposed to UV/ozone for 30 minutes to remove the contaminants from the wafer surface (Fig. 2.16a) and produce a clean, hydrophilic and oxidized gold mesh in the SU-8 microchannels (Fig. 2.16b). Afterward, the samples were immersed simultaneously in an etching mixture consisting of (HF(49%):H_2O_2(30%):H_2O=6:1:26:v:v:v) at room temperature in Clean Room facilities. The etching duration was varied from 2 to 8 minutes.

Effect of UV/ozone on the etching process

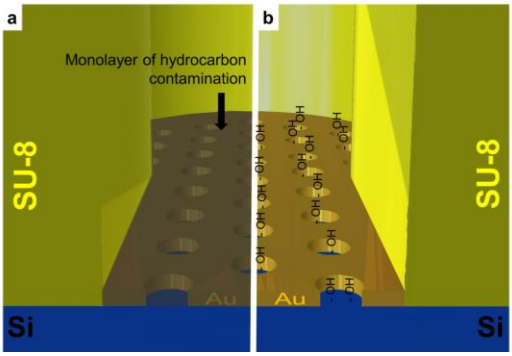

Figure 2.16. *UV/ozone cleaning* **(a)** *Schematic illustration of a sample formed by a gold mask and a monolayer of ambient hydrocarbon contamination placed in a SU-8 microchannel prior to exposure to UV/ ozone treatment.* **(b)** *Schematic illustration of a sample formed by a clean, hydrophilic and oxidized gold mask placed in a SU-8 microchannel after to UV/ ozone treatment* (*30 min*).

Fig. 2.17 shows the SEM images of structural changes in the SiNPs with and without UV/ozone treatment with respect to etching time. Particularly, Fig. 2.17a clearly shows that the etching process was slow in samples that were not cleaned with UV/ozone, and as a result, the heights of SiNPs were shorter than those samples subjected to UV/ozone (see Fig. 2.17b). This can be explained by considering contaminant residues on the gold mesh surface, which reduced its quality and delayed the etching reaction described by the equation (1.8). The UV/ozone treatment removed contaminants from sample surfaces and produced hydrophilic and oxidized gold mesh in the microchannels (see Fig. 2.16b) that resulted in an accelerated etching rate. Moreover, the SiO_2 monolayer formed in the Au holes of the mesh did not affect the reaction as it was dissolved by HF according to the chemical equation (1.8)[130]. Throughout the process, the morphology and quality of the SiNPs were not affected. Importantly, this simple cleaning step avoids the necessity to change the etchant concentration, the type of metal or to increase the temperature to accelerate the etching rate[70]. SEM images allowed a visual characterization of samples at different locations to obtain the average height and the StD value of the nanostructures. The temporal evolution of the SiNPs growth inside the SU-8 microfluidic channels is shown in Fig. 2.17c. According to the graph, an increase of the SiNP height with etching time was obtained in both conditions. It can also be observed that the heights of the SiNPs fabricated in the contaminated samples were 100%, 92%, 87% and 71% shorter than the heights of the SiNPs fabricated in the cleaned samples.

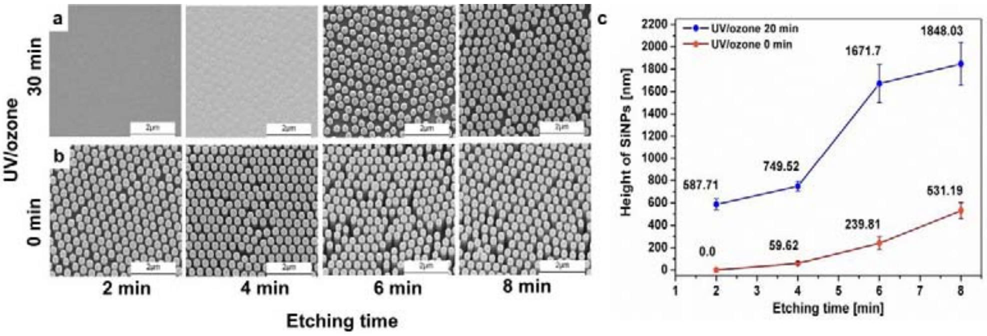

Figure 2.17. *Effect of UV/Ozone on the temporal evolution of SiNPs at different etching times. Their diameters were kept at ~280 nm with a center-to-center distance of 400 nm inside the microfluidic channel, during the metal-assisted chemical etching* (HF (49%): H_2O_2 (30%):H_2O=6:1:26:v:v:v). *Each row indicates the time that the samples were exposed to UV/ozone:* **(a)** *0 min and 30 minutes for* **(b)**. *Each column indicates the etching time of 2, 4, 6 and 8 minutes, respectively* (15° tilt view, scale bar=2 µm). **(c)** *In both graphs an approximately linear relationship between the heights and etching times was obtained when the etching rate increased with UV/ozone demonstrating its influence on the etching rate.*

Therefore, by controlling this factor, the successful fabrication of SiNPs with heights under and over 500 nm can be achieved at the same etching times, clearly demonstrating the influence of UV/ozone cleaning on the fabrication of the SiNPs. It is reasonable to think that a high H_2O_2/HF concentration, an excessive UV/ozone cleaning or etching time, with an inappropriate design of lithographic gold mesh, can produce SiNPs that are bent and collapsed towards the bottom gold surface, as summarized in the Fig. 2.18.

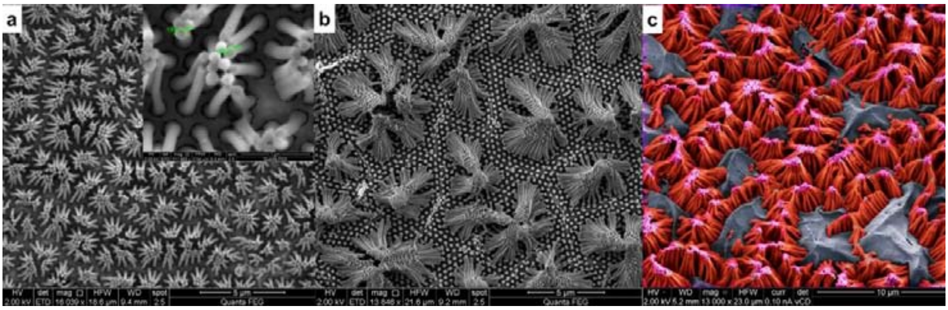

Figure 2.18. *SEM images of dramatic changes in the morphologies of SiNPs. Tip-clumped shape with bending SiNPs are produced by an inappropriate combination of fabrication parameters: UV/ozone cleaning=40 min, HF/H_2O_2/H_2O = 3.6/1/15.4,* **(a)** *etching time 5 min and* **(b)** *8 min.* **(c)** *without UV/ozone cleaning and an etching time of 15 min.*

2.6.3.3 Controlled fabrication of SiNPs within microchannels

To demonstrate the controllability and reproducibility of our nanofabrication method to create embedded nanostructures in polymer microfluidics, another series of experiments were performed. The characterization of three experiments was done with SEM images to calculate the average height and StD value of the SiNPs (see Fig. 2.19a).

Fig. 2.19b shows the temporal evolution of the SiNPs fabricated inside microfluidic domains using two different designs of the catalytic gold mesh, prepared with both PS 300 nm and PS 400 nm spheres, with a reduced diameter of ≈180 nm and ≈160 nm, respectively. The microchannels were etched in the same solution ((HF (49%): H_2O_2 (30%):H_2O=6:1:26: v: v: v)) for different times of 2, 4, 6 and 10 minutes, respectively. The results confirmed that in the two different catalytic meshes, the height of SiNPs increases as the etching time becomes longer. Additionally, the graph shows that the design of the catalytic Au mesh with respect to the diameter of the mesh holes, the periodicity (d_{cc}=300, d_{cc}=400) and the hexagonal array, influenced as well the etching rate.

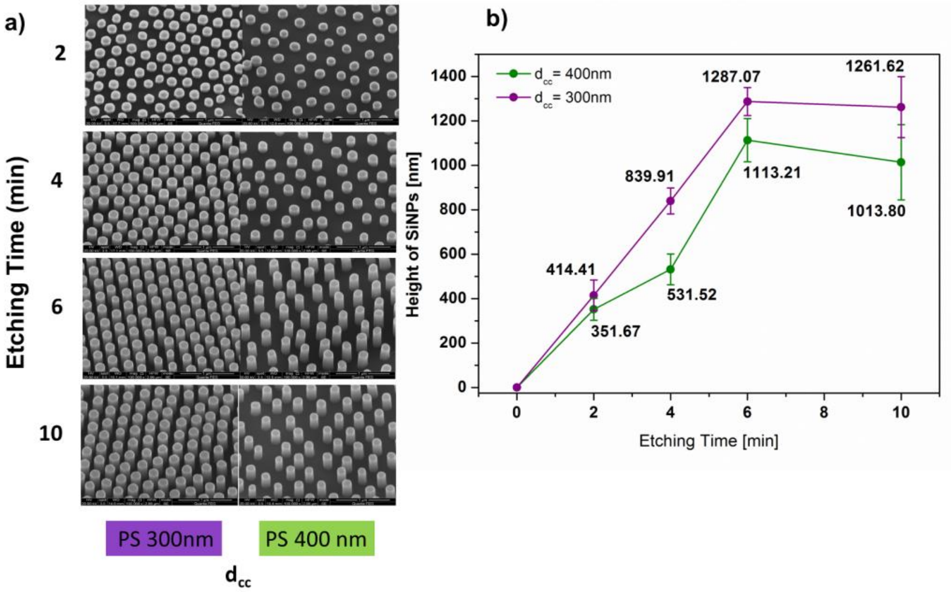

Figure 2.19. (a) *SEM images of temporal evolution of Si nanopillar heights in the SU-8 microfluidic channels during the etching process (15° tilt view, scale bar=1 µm).* ***(b)*** *Average heights of the SiNPs separated at a center-to-center distance (dcc) of 300 nm and 400 nm for 2, 4, 6 and 10 minutes, respectively.*

Table 2.4. *Characteristics of the SiNPs in SU-8 microfluidic channels*

Etching time [min]	d_r= 180 nm , d_{cc}=300 nm [a], Height [nm] [b]	Aspect ratio $(H/d_r)^c$	% StD [d]	d_r= 160 nm, d_{cc}=400nm [a] Height [nm] [b]	Aspect ratio $(H/dr)^c$	% StD [d]
2	414.41±68.99	2.30	16.64	351.67±49.47	2.19	14.06
4	839.91±58.44	4.66	6.95	531.52±69.37	3.32	13.05
6	1287.07±62.83	7.15	4.88	1113.21±96.93	6.95	8.70
10	1261.62±136.90	7.00	10.85	1013.80±169.08	6.33	16.67

[a] d_{cc}= center to center distance of nanopillars
[b] mean ± standard deviation of 3 replicates of the experiment
[c] H/d_r =Height / reduced diameter
[d] %StD represents the percentage of Std with respect to mean value

It can also be observed that the heights of the SiNPs (dr =180 nm) separated at a d_{cc} of 300 nm were higher than the heights of the SiNPs (dr =160 nm) separated at a d_{cc} of 400 nm. This can be explained by the fact that the area with the gold/silicon interface in the mesh with the dr=180 nm and d_{cc}=300 is smaller than in the mesh with the dr=160 nm and d_{cc}= 400 nm, then it sinks faster into the silicon following the reaction (1.8), thereby producing higher SiNPs. It demonstrates that the combination of dr and d_{cc} plays a key role to control the etching rate. Interestingly, after 6 minutes, the etching rate began to stabilize in both cases. To prove the high control of our protocol over the formation of SiNPs, three samples were etched during 1, 2 and 5 minutes, maintaining the same d_{cc} at 400 nm, but now with a dr=280 nm. Fig. 2.20 indicates the cross-sectional images of the SiNPs in the microchannel. The resulting heights

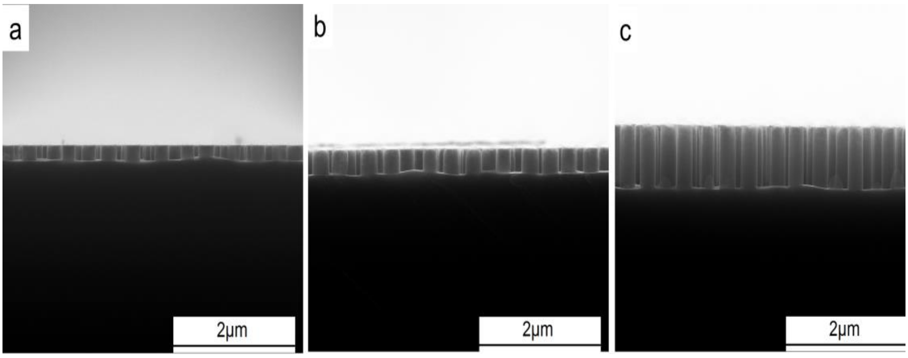

Figure 2.20. *Cross-sectional SEM images of SiNPs inside the SU-8 microfluidic channels using PS 400 nm spheres with a reduced diameter of 280 nm. The etching times were for* **(a)** *1,* **(b)** *2, and* **(c)** *5 minutes with heights of ~ 180 nm, ~300 nm and ~750 nm, respectively, according to the measurements obtained by SEM images.*

were ≈180 nm, ≈300 nm, and ≈ 750 nm, respectively, which were the expected values according to the results described in Fig. 2.19b. Finally, Table 2.4 shows the mean and StD values of the heights of the fabricated SiNPs. The column % StD represents the percentage of standard deviation with respect to the heights mean value. In both fabrications, there was a controlled and proportional increase in the aspect ratio, and the %StD did not exceed 17%, which was acceptable for our fabrication purposes.

2.7 Conclusions

In summary, we have described a simple and low-cost fabrication protocol of ordered arrays of silicon nanopillars with integrated polymer microfluidics. With our fabrication strategy, the area, hexagonal arrangement, diameter, and height of the SiNPs within the microchannel are well controlled. In this process, it was shown that the diameter of the PS spheres (300 nm and 400 nm of diameter) was reduced by RIE treatment and these results were used to control the diameter of the SiNPs. Explanation and advice were given on how to reduce defects and imperfections in the fabrication of the microchannel and the catalytic gold mesh. Our investigation confirmed that the height of SiNPs increases as the etching time becomes longer. Moreover, the simple cleaning of the microchannels by UV/Ozone clearly affects the etching rate. Importantly, this step avoids the necessity to change the etchant concentration, the type of metal or to increase the temperature to accelerate the etching rate. Through our results, we demonstrate that the combination of reduced diameter (dr), and periodicity (dcc) of the catalytic gold mesh plays a key role in order to control the etching rate. The results from our strategy offer a controlled tool for the creation of plasmo-mechanical sensors integrated with microfluidics.

Chapter 3 Building of the integrated microfluidic sensor

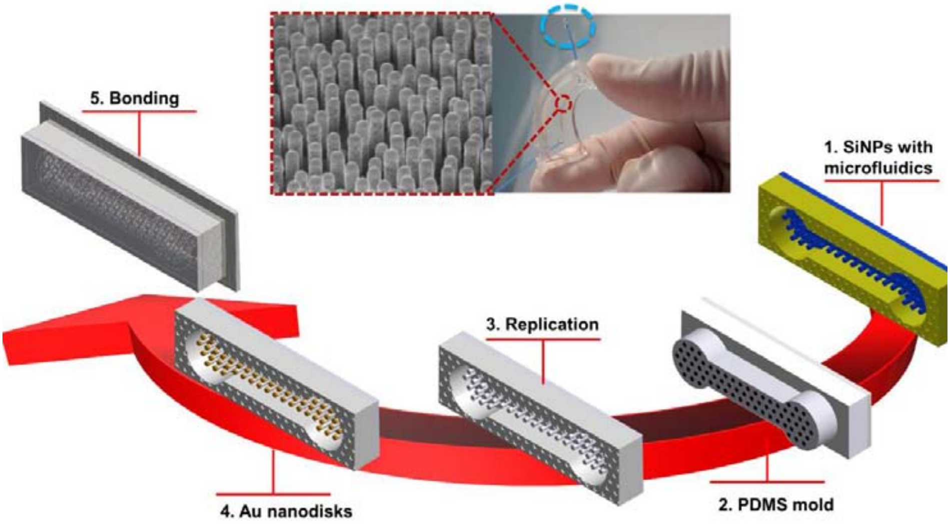

The plasmomechanical sensor consisting of a hexagonal array of vertically aligned polymers nanopillars capped with plasmonic gold nanodisks, within a microfluidic channel. Replica molding technique is our fabrication strategy to develop the sensor. Therefore, the fabrication consists of five steps: **1)** *fabricating a Si master mold,* **2)** *molding this master to generate a patterned stamp (PDMS mold),* **3)** *generating a replica of the original template in a polymer material,* **4)** *Evaporation of plasmonic gold nanodisks on the polymer nanopillars and* **5)** *the sensor bonding for the microfluidics.*

3.1 Introduction

As discussed in Chapter 2, with the implemented fabrication strategy, the area, hexagonal arrangement, diameter, and height of the silicon nanopillars within the fluidic microchannel are well controlled. In this chapter we describe the process for developing the flexible plasmomechanical sensor, consisting of an array of closely spaced, vertical, polymer nanopillars capped with plasmonic gold nanodisks and embedded in a microfluidic system. The fabrication of the sensor is based on a replica molding technique where the gold nanodisks are incorporated on the polymer nanopillars by e-beam evaporation. In this chapter, we provide: (i) the strategies for controlling the replication of Si master using thermal polymers and photopolymers with different Young´s modulus, in order to minimize the distortions in the process and to obtain a reliable replica of the Si master mold. The Si master molds of the sensor consist of a hexagonal array of SiNPs with diameters from ≈140 nm to ≈200 nm, and heights ranging from ≈200 nm to ≈1.3 µm, with center to center separations (d_{cc}) of 400 nm and 300 nm, integrated in a SU-8 microfluidic channel,(ii) the mechanical characterization of the polymer nanopillars. The elastic constant or spring constant k of the polymer nanopillars is evaluated and (iii) polymer-based bonding strategies for microfluidic integration of the sensor.

The fabrication process was divided into four steps: **1)** fabrication of polydimethylsiloxane (PDMS) mold, **2)** replication of Si master mold, **3)** evaporation of gold nanodisks on the polymer nanopillars (PNPs) by e-beam evaporation and **4)** bonding process (Fig. 3.1).

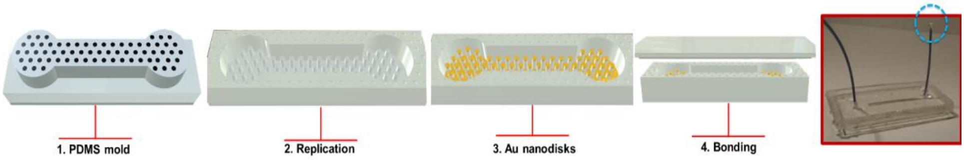

Figure 3.1.*Overview of the replica process of Si master mold and bonding process to create the plasmomechanical sensor.*

3.2 Fabrication of the Polydimethylsiloxane mold

Process

To create the polydimethylsiloxane (PDMS) mold, the surface of the silicon master was cleaned and oxidized by an oxygen plasma cleaner (Femto plasma cleaner, Electronic Diener Inc, Germany) at 75 W, with a flow rate of 15 % for 2 min. Then, it was treated with an aliquot (50 µl) of (tridecafluoro -,1,2,2-tetrahydrooctyl) trichlorosilane in a vacuum desiccator for 2 h at room temperature to deposit a monolayer on the Si nanopillars. This layer avoids that the polymers stick permanently and helps the unmolding step (see Figs. 3.2a,b). The PDMS prepolymer and curing agent (DOW Sylgard 184) were thoroughly mixed in a volume ratio of 10:1, followed by a first degassing for 20 min to remove the air bubbles. The degassed PDMS mixture was gently poured onto the silicon master (Figs.3.2 c,d) and a second degassing for 1 h was applied (Figs. 3.2e,f). The PDMS was then cured at ~100 °C for 1h on a hot-plate (KW-4AH, Chemat Technology Inc, United States). Finally, the cured PDMS was carefully removed from the Si master manually (Figs. 3.2g,h). UV curable polymers and epoxy resins were used to produce the replica of the Si master mold of sensor.

3.2.1 Results and Discussion

PDMS molds of nanoholes were fabricated from the silicon masters according to the controlled procedure described in the Fig. 3.2. Fig. 3.3 shows the SEM image of negative PDMS molds. The PDMS pattern (thickness 1mm) contains the hexagonal array of nanoholes whose depths correspond to the heights of the SiNPs. These results confirm the excellent combination of our protocol and the ability of the PDMS (Sylgard 184) to mold the Si nanostructures in the SU-8 channel to a large area. The use of PDMS molds is inexpensive and multiple copies can be replicated from the original master mold (around 25) without deformations, which make it attractive for effective and low cost sensor fabrication. The differences observed in the diameter values and the presence of defects can be explained by variations of the original master molds.

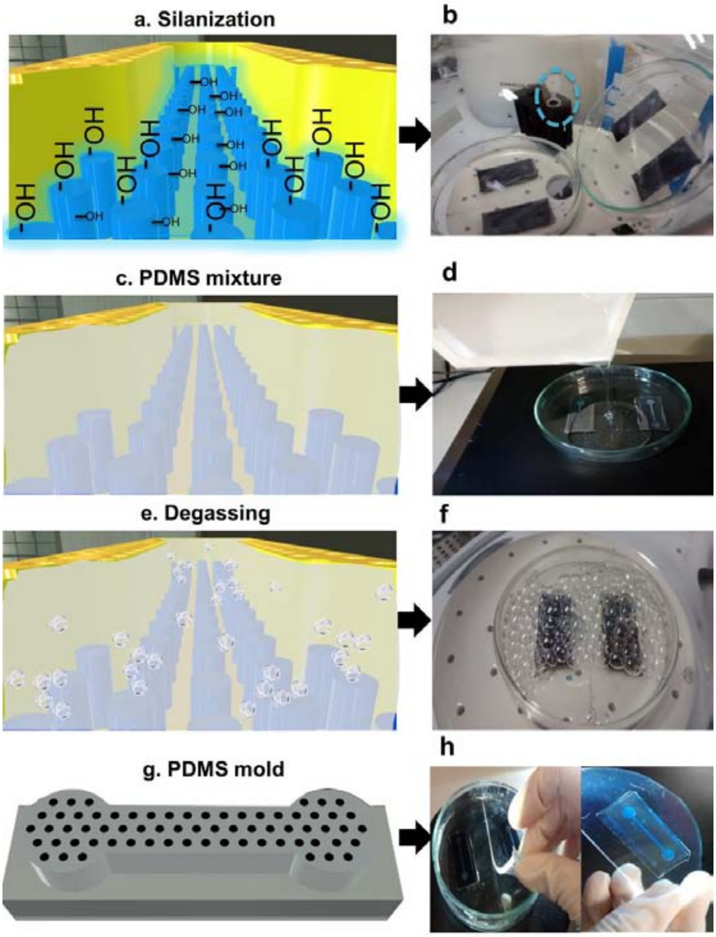

Figure 3.2. *Procedure of fabrication of the negative PDMS mold:* **a)** *Silanization of Si master.* **b)** *Silanization in a desiccator with an aliquot of silane (shown in dashed circle) and the Si masters.* **c)** *PDMS covering the silicon nanopillars in the SU-8 channel.* **d)** *Photo showing the pouring of the mixed PDMS prepolymer onto the silanized Si master molds.* **e)** *Bubbles rising from the PDMS.* **f)** *Photo showing the degassing of the PDMS prepolymer inside a vacuum at room temperature.* **g)** *PDMS mold of nanoholes whose depths correspond to the heights of the SiNPs.* **h)** *A picture showing the PDMS mold.*

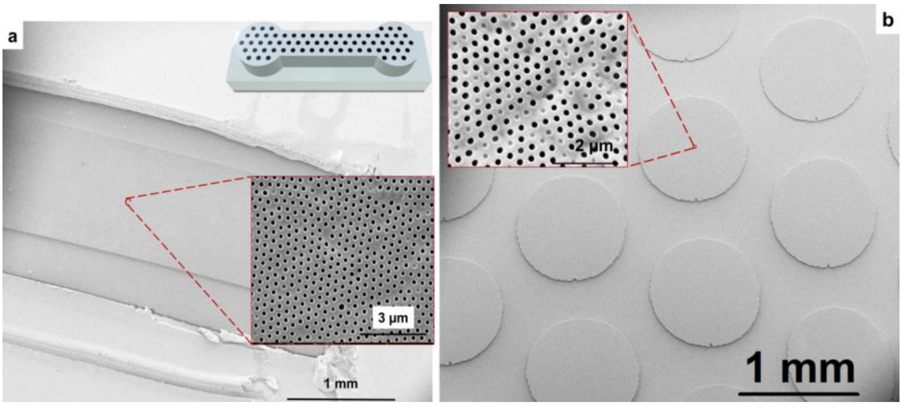

Figure 3.3. (a) *PDMS mold of nanoholes within a microchannel.* **(b)** *Area protruding from the plane surface, which shape corresponds to the shape of the silicon master mold of nanopillars.*

3.3 Replication of the Si master mold and evaporation of gold nanodisks

Process

UV curable polymers: The selected polymer (1.0 g) was poured on the PDMS and placed in a vacuum desiccator in order to remove the air bubbles and to fill the nanoholes (Figs. 3.4a,b). It was then covered with a precleaned glass slide or PDMS film (Fig. 3.4c). Next, the polymers were exposed to a UV light (≈190 mW at 365 nm, normalized intensity), see Fig.3.4 d. **Thermal polymers:** According to the data sheet, the mix ratio of epoxy resin was prepared (1.0 g) to cure the polymer in the shortest time possible, and thereby, poured on the PDMS. The mixture was placed in a vacuum desiccator to remove the air bubbles and to ensure complete filling of the PDMS nanoholes (Figs.3.4a,b).The polymer was covered with a precleaned glass slide or PDMS film (Fig.3.4c) and was then cured on a hot-plate (Fig. 3.4e). After curing, all polymer structures were carefully peeled off from the PDMS mold (Fig. 3.4f).

Finally, the gold nanodisks were incorporated on the polymer nanopillars by e-beam evaporation. Figs. 3.4g and h show a thin metallized polymer replica (thickness 279 ±25 µm) result by using the PDMS film as a support, and a polymer replica on a glass.

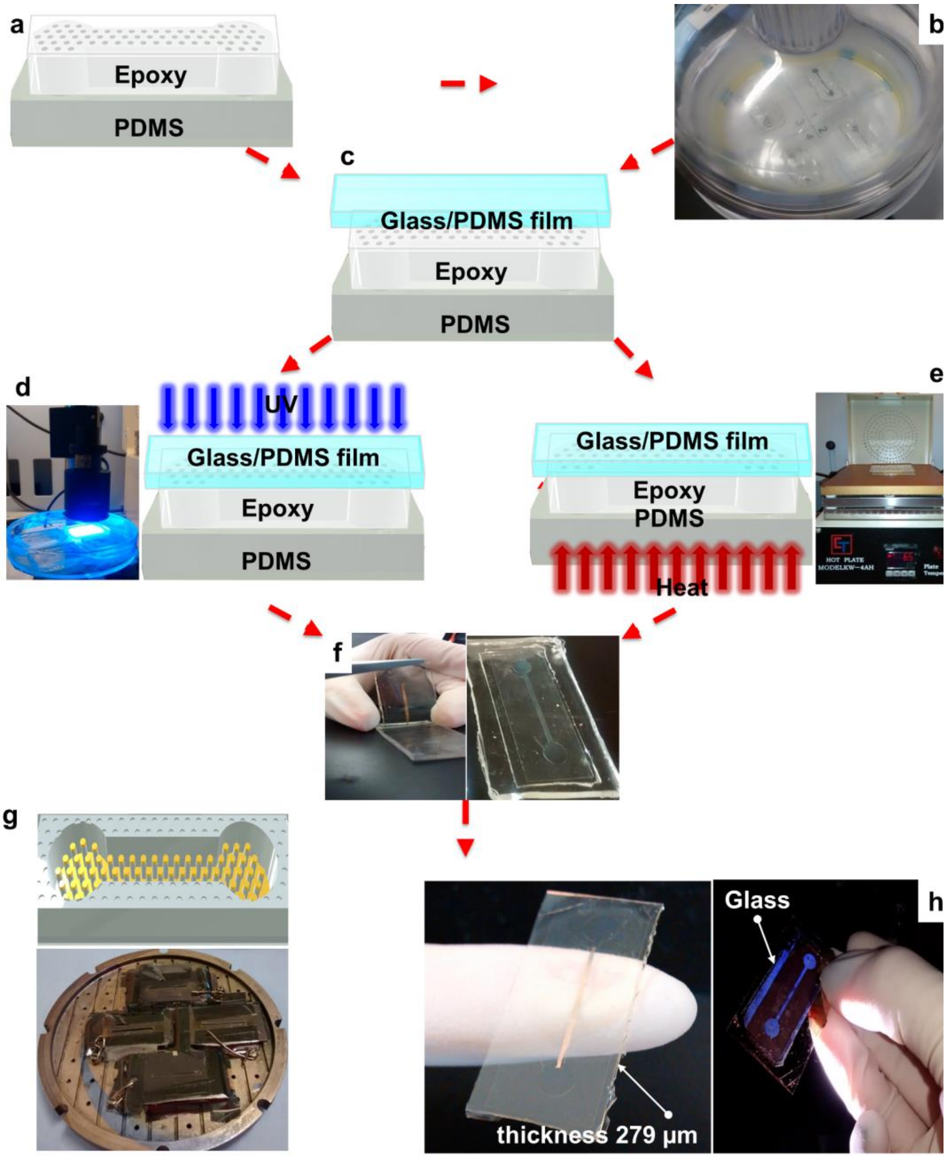

Figure 3.4. *Schematic illustration of the replica molding steps.* **(a-b)** *Removal of the air bubbles from the polymer by degasssing in a vacuum desiccator.* **(c)** *Glass slide covering the pre-polymer.* **(d)** *Curing of the polymer by a UV lamp.* **(e)** *Curing of the polymer by temperature.* **(f)** *Demolding by peeling the PDMS from the polymer replica.* **(g)** *Gold nanodisks on the polymer nanopillars in a channel.* **(h)** *Photo of a thin metallized polymer replica and other on a glass.*

3.3.1 Polymers for the replica of the Si master mold

In the molding process, filling of nanoholes with liquid precursor is capillary-force-controlled. The complete filling time can be a function of the viscosity of the liquid epoxy polymer, the radius of the nanohole, and the contact angle between the liquid and the surface of the capillar (θ). A lower contact angle (i.e., higher wettability) of the liquid on the PDMS mold with and without nanoholes, is preferred for a complete filling in a short period of time.

Table 3.1 *Plysical Properties of Polymers employed to replicate the Si master mold*

Polymer	Viscosity^a (23˚C)(cPs)	Young´s^a Modulus	Spectral Transmission^a	Degradation Temp^a(˚C)	Contact angle (θ) ^{b}	Contact angle (θ)^c
NOA 65^d	1200	.137 GPa	≥99% @ 450-1200 nm,IR=1.524	-	48.4 ± 0.79	57.7 ± 0.46
NOA 81^d	300	1.38 GPa	≥99% @ 400-1000 nm, IR=1.56	-	65.7 ± 0.06	71.4 ± 0.24
OG133-8	1000-1500	2.42MPa	≥95% @ 900 nm ,IR=1.5244@ 589 nm	353	26.3 ± 3.65	30.6 ± 3.97
UVO-114	350-550	1.56 GPa	≥94% @ 500-1400 nm, IR=1.5191@ 589 nm	361	118.2±3.27	92.5 ± 6.56
OG142-87	250-600	3.59 GPa	≥97% @ 580-1600 nm, IR=1.5058@ 589 nm	384	47.3 ± 0.30	66.8 ± 0.23
OG603	150-250	1.73 GPa	≥98% @ 420-1600 nm, IR=1.5037@ 589 nm	385	42.5 ± 0.13	57.6 ±0.74
Super Gel	3000-9000	62 MPa	≥99% @ 400-1000 nm, IR=1.5253	93	52.1 ± 0.13	55.9 ± 3.90
301-2FL	100-200	1 GPa	≥99% @ 400-1000 nm, IR=1.5115@ 589 nm	325	54.6 ± 0.24	64.7 ± 0.11
310M	450-850	4.16 MPa	≥97% @ 400-1300 nm, IR=1.5129@ 589 nm	397	58±0.12	53.4±0.29

a ,Data from vendor, Epoxy Technology, Inc.
b ,Contac angles between the liquid prepolymers and PDMS
c,Contac angles between the liquid prepolymers and PDMS mold of nanoholes
d ,Norland Optical Adhesives

Table 3.1 shows the physical properties of the polymers tested to replicate the Si master mold. It includes two kinds of polymers, photopolymer and thermal polymers, with different viscosity and Young's Modulus in order to create soft and hard nanopillars. Also, we can see that their contact angles on both, a planar surface of PDMS and a PDMS mold of nanoholes, are smaller than 90˚ and then are considered suitable for the replica process.

Table 3.2. *Protocols of functional Epoxy resins (1 g) to create the polymers nanopillars*

Polymer	Protocol	SiNPs (nm)	Polymer	Protocol	SiNPs (nm)
NOA 65	Precure= 5 s/UV Without UV=2 min Fullcure 40 min/ UV	$H_{SiNPs}=1113.21$ $D_{SiNPs}=207.6$ ratio=5.36	OG603	Degasssing=3 min Precure= 15 s/UV Without UV=1 min Fullcure 4 min/ UV Cure= 2h@150˚C	$H_{SiNPs}=940$ $D_{SiNPs}=150$ ratio=6.2
NOA 81	Precure= 15 s/UV Without UV=1 min Fullcure 3 min/ UV	$H_{SiNPs}=1678.3$ $D_{SiNPs}=207.6$ ratio=8	Super Gel	Fullcure= 12h@80˚C	$H_{SiNPs}=527.26$ $D_{SiNPs}=207.6$ ratio=2.53
OG133-8	Degassing=1 h Precure= 1 min/UV Without UV=1 min Fullcure 5 min/ UV	$H_{SiNPs}=764.37$ $D_{SiNPs}=200$ ratio=2.636	301-2FL	Degasssing=1 h Fullcure= 3h@80˚C	$H_{SiNPs}=764.37$ $D_{SiNPs}=200$ ratio=3.82
UVO-114	Degasssing=6 min Precure= 1 min/UV Without UV=1 min Fullcure 7 min/ UV	$H_{SiNPs}=1678.3$ $D_{SiNPs}=207.6$ ratio=8	310M	Degasssing=1.5 h Fullcure= 1 day +2h@65˚C	$H_{SiNPs}=493.56$ $D_{SiNPs}=154.27$ ratio=3.2
OG142-87	Degasssing=6 min Precure= 30 s/UV Without UV=1 min Fullcure 4 min/ UV Cure= 2h@150˚C	$H_{SiNPs}=940$ $D_{SiNPs}=150$ ratio=6.2			

Table 3.2 contains the protocols for the aforementioned polymers. It is important to point out that the protocols ignore possible air trapped by the introduction of the liquids. Nevertheless, we observed air bubbles in the nanopillars when the glass or PDMS film is placed over the polymer.

3.3.2 Results and Discussion

Polymer nanopillars replicated from the corresponding silicon master with different heights and diameters are exemplified in Fig. 3.5. It clearly shows that in spite of the mechanical characteristics of Super Gel, NOA 65 and NOA 81 they did not penetrate in the nanoholes. On the other hand, the photopolymers (OG133-8, UVO-144, OG142-87, OG603) and thermal polymers (301-2FL, 310M), could penetrate the nanoholes with diameters from 150 nm to 200 nm and different deeps. It is clearly shown that their viscosity and Young’s Modulus are important factors to fully penetrate the mold and to keep vertically the nanopillars. In order to know which polymer should be finally selected to create suitable soft and rigid polymers nanopillars, we performed a study to identify the limit of the aspect ratio of the structures that they can replicate.

Arrays of SiNPs with an increasing aspect-ratio integrated in the SU-8 channels (Figs. 3.6a-c) were replicated from the corresponding PDMS molds using polymers with different Young´s modulus (see Table 3.1), and gold nanodisks were placed on them by e-beam evaporation. As shown in Figs 3.6d-l epoxy nanopillars with an aspect ratio < 3.75 were found stable without any pattern collapse. However, Figs 3.6g,h,j and k clearly show that 301-2FL and

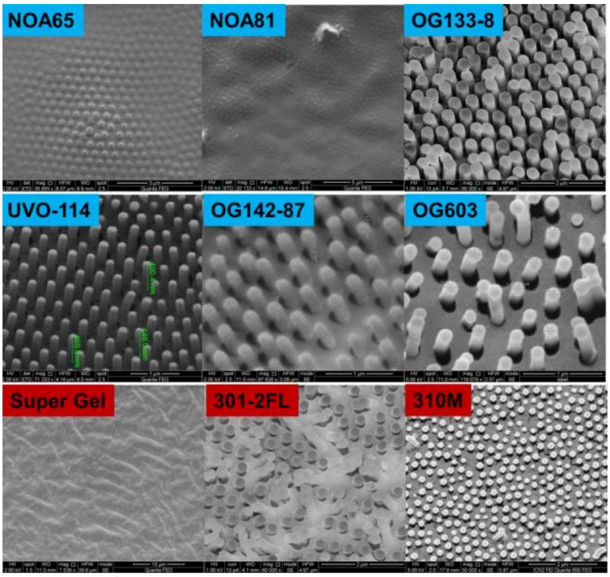

Figure 3.5. *SEM images of polymer nanopillars. Photo and thermal polymer were used to identify the optimal one for the replica molding process. Images from 1 to 6 are materials with a Young’s Modulus >1GPa for hard tissues. Images from 7 to 9 are materials with a Young´s Modulus< 1 GPa for soft tissues.*

OG133-8 nanopillars did not have the same height between them as the UVO-114 nanopillars show (Figs. 3.6d,e).

The fabrication of polymer nanopillars with an aspect ratio of 6.5 found that EPOTEK-UVO-114 completely filled the PDMS nanoholes, and its mechanical properties helped to avoid the collapse of the nanopillars (Figs.3.6.f,i,l). Fig 3.6.i and Fig 3.6.l show collapsed 301-2FL and OG133-8 nanopillars, which can be attributed to the surface adhesive forces between the PDMS and the replica during separation as well as to the influence of the material stiffness.

As above described, the diameter of the nanoholes strongly influences the stability of the polymer nanopillar arrays. Then, we reduced the diameter to replicate SiNPs with a high aspect ratio of 4.4 and 5.5 (see Fig. 3.7 a,b) with the polymers whose Young’s Modulus are 3.59 GPa (OG142-87) and 1.73 GPa (OG603). It is important to point out that a reduced diameter increased the difficult to fill the nanoholes but the separation helps in the unmold step. Figs. 3.7 e-h show the stable replication results without any pattern collapse.

On the other hand, 310M (4.16 MPa) and 310M-1 (32.39 MPa) were used to produce soft nanopillars with an aspect ratio of 1.49 and 2.15 (Fig. 3.7i-l). We can observe that the shape and height are the same as the original Si masters.

According to the experiments performed, we could conclude that the polymer OG142-87 and 310M were the best materials to create rigid and soft polymer nanopillars ensuring reproducibility and generating the suitable replication of original Si master of the sensor.

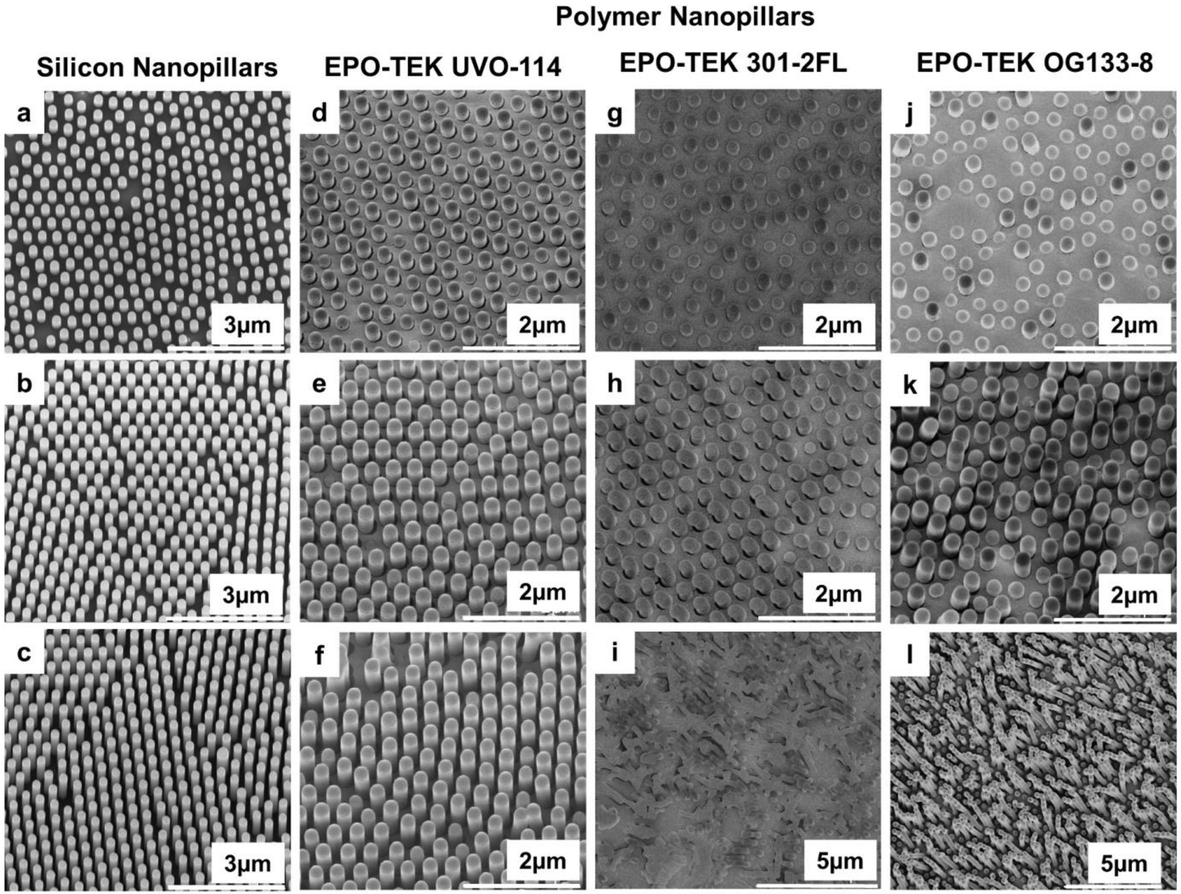

Figure 3.6. *SEM images of silicon and polymer nanopillars.* **(a-c)** *Silicon nanopillar arrays as master molds. Features dimensions dp =200 nm, dcc=400 nm, h=500 nm , 750 and 1.3µm, respectively*. **(d-f)** *Epotek-UVO-114 nanopillars*, (g-**i)** *Epotek- 301-2FL nanopillars and* **(j-l)** *Epotek- OG133-8 nanopillars*, (15º tilt view).

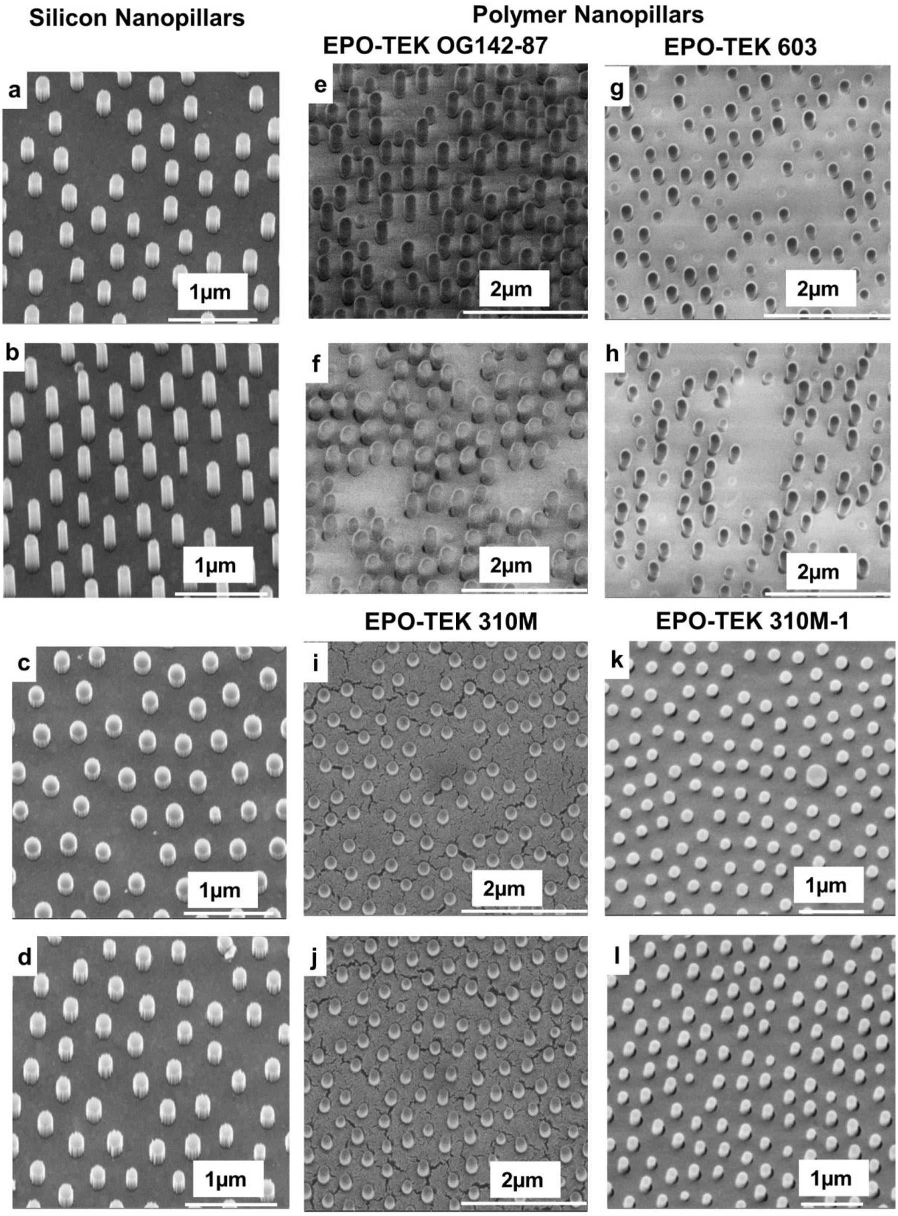

Figure 3.7. *SEM images of silicon and polymer nanopillars.* **(a-d)** *Silicon nanopillar arrays as master molds. Features dimensions dp =140 nm for a,b and 165 nm for c and d, dcc=400 nm, h=560 nm , 1040 nm, 264 nm and 410nm, respectively.* **(e-f)** *Epotek-OG142-87nanopillars,* **(g-h)** *Epotek-603 nanopillars,* (**i-j)** *Epotek-310M nanopillars, and* **(k-l)***Epotek-310M-1 nanopillars* (*15º tilt view*).

3.3.3 Spring constant of polymer nanopillars: mimicking tissues

Table 3.3 compares the experimental aspect ratio of the polymer nanopillars capped with gold nanodisks (thickness= 25 nm) with the corresponding values of silicon master. The results showed an increase in almost all the diameters of the polymer nanopillars (d_p) and a decrease in the heights, as a result, the aspect ratios of the polymer nanopillars were smaller than the Si masters. A possible explanation for this might be that the temperature at which the different polymer nanostructures were exposed during the deposition of the gold nanodisks by e-beam evaporation, caused these distortions which are consistent with the results of other processes of replica molding [131,132]. Other distortions are due to unmold step, as we observed that the polymer nanopillars adopt the orientation at which were separated from the PDMS mold.

Moreover, Table 3.3 shows the spring constant (k) that the polymer nanopillars produce according to their aspect ratio, and the Young's Modulus of the material. The calculation of the k is extracted from the formula 1.1[98], the aspect ratio, and Young Modulus are substituted in $k = \left(\frac{3}{4}\pi E\frac{r^4}{L^3}\right)$, and then the results are compared with experimental data of elastic moduli of real tissues[133] to identify the mimicked tissue (See Annex A). Also, the k indicates the mechanical sensibility (stiffness) of the sensors to a shear stress.

We can conclude that using OG142-87 and 310M polymers, SiNPs with diameters from 140 nm to 170 nm and heights ranging from 260 nm to 1µm can be replicated by our protocol. Also, the spring constant of those gold capped polymer nanopillars can not only be designed to create polymer structures with different mechanical sensitivity to a shear stress but also to mimic soft tissues such as muscle and rigid tissues such as bone.

Table 3.3. *Comparison of experimental results of aspect-ratios of polymer nanopillars*

SiNPs dimension			EPOTEK-UVO-114 (1.56 GPa)				EPOTEK-301-2FL (1 GPa)				EPOTEK-OG133-8 (2.42 MPa)			
dr (nm)	h (nm)	aspect-ratio	d_{pnp}[a] (nm)	h (nm)	aspect-ratio	Spring constan [N/m]	d_{pnp}[a] (nm)	h (nm)	aspect-ratio	Spring constan [N/m]	d_{pnp}[a] (nm)	h (nm)	aspect-ratio	Spring constan [N/m]
200	500	2.5	260	410	1.57	1.56E+01 **bone**	220	260	1.18	2.07E+01 **bone**	220	400	1.81	1.48E-02 **muscle**
200	750	3.75	270	780	2.88	2.74E+00 **bone**	220	560	2.54	2.53E+00 **bone**	270	620	2.29	9.20E-03 **liver**
200	1300	6.5	260	1350	5.19	3.66E-01 **cartilage**								
			EPOTEK-OG142-87 (3.59 GPa)			Spring constan [N/m]	EPOTEK-OG603 (1.73GPa)			Spring constan [N/m]				
141	560	3.97	201	883	4.4	1.37E+00 **bone**	156.	468	3	1.75E+00 **bone**				
141	1040	7.37	193	1014	5.25	7.70E-01 **cartilage**	165.	719	4.35	5.81E-01 **cartilage**				
			EPOTEK-310M(4.16MPa)			Spring constan [N/m]	EPOTEK-310M-1(32.39MPa)			Spring constan [N/m]				
165	264	1.6	174.9	261	1.49	3.61E-02 **muscle**	160.	260	1.62	2.20E-01 **cartilage**				
165	410	2.64	171.2	368	2.15	1.19E-02 **muscle**	169.	428	2.52	5.73E-02 **muscle**				

[a] Botton diameter is used for calculation.
d_r ,reduced diamter of silicon nanopillar
$d_{pnp,}$ diameter of polymer nanopillar
dcc, distance center to center =400 nm

3.4 Gold film on the sensor

Fig. 3.8a shows a schematic representation of the nanopillars integrated in the polymer microchannel with the Au nanodisks deposited by e-beam evaporation. Importantly, with this technique not only the nanodisks are formed, but also an array of nanoholes in a thin film, due to the Au film that is deposited at the bottom of the polymer surface. The nanoholes are also nanostructures that generate LSPR, then for this reason we performed several experiments to remove the gold film and to obtain a configuration without Au film as shown in Fig. 3.8b.

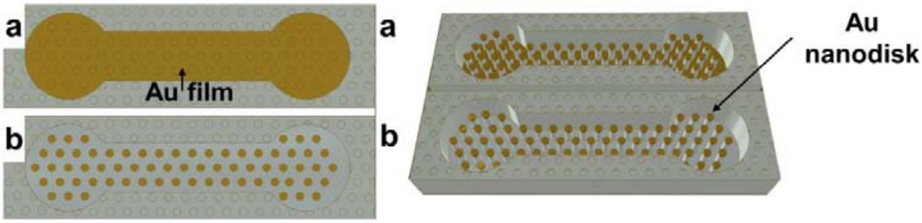

Figure 3.8. (a) *Schematic representation of the plasmomechanical nanosensor showing the Au film (25 nm) and the Au nanodisks deposited on the polymer nanopillars.* **(b)** *Au nanodisks on top of the polymer nanopillars*

Removing of the gold film by silanization of SiNPs and transfer of Au nanodisks to the PDMS mold and to polymer replica

The strategy is to take off the Au nanodisks from the SiNPs to the bottom of the nanoholes of PDMS mold, and next to dissolve the Au film deposited on the top of PDMS mold by KI solution. Once done, UV curable polymers and epoxy resins were used to produce the replica of the Si master and try to adhere the Au nanodisk at the bottom of the PDMS holes.

Process

First, Si nanopillars (SiNPs) with a diameter of ≈207 nm and height of ≈640 nm were cleaned and oxidized by an oxygen plasma cleaner (Femto plasma cleaner Electronic Diener Inc, Germany) at 75 W, with a flow rate of 15 % for 2 min. Then it was treated with an aliquot (50 µl) of (tridecafluoro -,1,2,2-tetrahydrooctyl) trichlorosilane in a vacuum desiccator for 2 h at room temperature to deposit a monolayer on the Si nanopillars. This layer avoids that the pdms stick permanently and helps the unmold step. Next, 25 nm of gold were deposited on the SiNPs by e-beam as is shown in Fig. 3.9a. Then, the degassed PDMS (10:1) mixture was gently poured onto the silicon master and a second degassing for 1 h was applied. The PDMS was then cured at 100 °C for 1h on a hot-plate (KW-4AH, Chemat Technology Inc). Finally, the cured PDMS was carefully removed from the Si master manually.

Results

Fig. 3.9b shows the SiNPs after unmolding the PDMS. It clearly shows the gold film deposited on the ground of SiNPs, also, it is observed that SiNPs do not have the Au nanodisks, which means that they were unglued and placed on the bottom of PDMS nanoholes. Unfortunately, there were zones where the Au film was elevated and then the Si nanopillars were harmed (see Fig. 3.9c). Also, the PDMS penetrated under Au film damaging the Si master and leaving residues of PDMS between the SiNPs, (see Fig 3.9d). Moreover, the polymer nanopillars fabricated with these PDMS molds did not have any Au nanodisks, they were trapped in the bottom of the PDMS mold. Therefore, this tactic was unsuccessful.

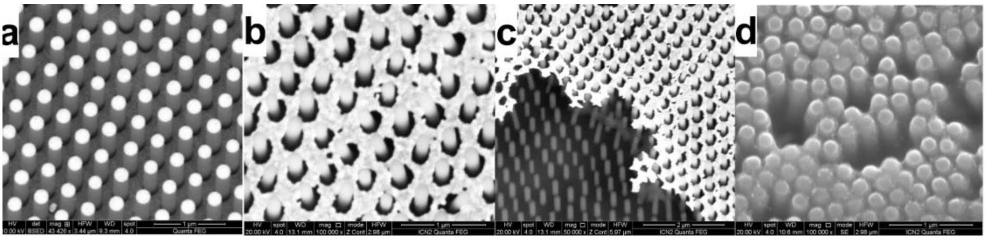

Figure 3.9. **(a)** *SiNPs with Au nanodisks and the film deposited by e-beam.* **(b)** *and* **(c)** *SEM image of SiNPs without Au nanodisks after unmolding the PDMS. The gold film is elevated from the ground.* **(d)** *SiNPs covered with PDMS remains.*

Removing of the gold film by Au evaporation on PDMS molds

The PDMS mold was fabricated according to the procedure described in Section 3.2 and the Au layer were deposited by e-beam. Then, the Au film deposited on top of the PDMS mold was removed by using a blue tape. Next, the PDMS mold was subject to the process of replica described in Section 3.3. Regardless of the aspect ratio of the SiNPs, the PDMS mold of nanoholes was distorted due to the high temperatures and vacuum of the e-beam evaporator, also by the porosity of PDMS mold (ATC ORION deposition system, United States).

Result.

Fig. 3.10 shows the PDMS mold expanded by the effect of the temperature and vacuum of the evaporator, and PDMS porosity, and as a result, the nanoholes closed avoiding that the Au nanodisks were deposited at the bottom. As were not able to control the temperature of the system, the process of replica could not be carried out, and this strategy was unsuccessful. We can conclude that the final configuration of the plasmomechanical sensor is formed by a hexagonal array of polymer nanopillars within a microfluidic channel. Gold plasmonic nanodisks are on top of the polymer structures with a gold film on the ground of the sensor as shown in Fig. 3.8a.

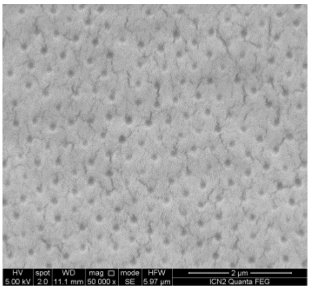

Figure 3.10. *(a) SiNPs with Au nanodisks and the film deposited by e-beam. (b) and (c) SEM image of SiNPs without Au nanodisks after unmolding the PDMS*

3.5 PDMS based Bonding Strategy of the microfluidic channels

The next step is the building of the integrated microfluidic sensor, for that, we need to seal the different microfluidic channels with the Au-capped polymer nanopillars. Polydimethysiloxane (PDMS) is widely used for fabricating chip-based microfluidic devices using mainly lithography and replica molding processes. The ease of fabrication, low cost, biocompatibility, elastomeric property, and optical transparency are attractive reasons for its wide usage for rapid prototyping. A number of PDMS bonding techniques have been reported in the literature over PDMS microfluidic devices. Also, oxygen plasma bonding is a method widely used due to its cost, fabrication time and excellent bonding results. This technique is used for getting irreversible seals by exposing the surfaces to oxygen plasma (e.g. glass or silica).

Materials

An oxygen plasma cleaner (Femto plasma cleaner Electronic Diener Inc, Germany) was employed for the cleanliness of the polymer surfaces. A SYRINGE pump (NE-1010 higher pressure programmable PumpSystemsInc, United States) was employed for providing the solutions sensor with controlled flow, two PEEK tubes (Valco Instruments Co. Inc. JR-T-6009, Canada) of 250 µm of I.D. were affixed to each reservoir to complete the integration of microfluidics. A microfluidic valve (VICI valco Instriments, Canada) was used to inject the samples towards the sensor.

Bonding process

It is important to point out that a number of factors can avoid the contact between the surfaces and influence the quality the bond, including cleanliness of the bonding surfaces, the aspect ratio of the microfluidic channel, the roughness or defects of the PDMS lid. In particular, we combined the oxygen plasma to clean the surfaces with a partial curing of PDMS (25:1) for the bonding between the PDMS lid, and the polymer (310M, OG142-87) replica. The alignment between the surfaces is fast and easy, reducing the chances of damaging their topography and integrity. In this process, we cleaned the surfaces to remove any contamination that avoid the contact between the PDMS and polymer replica by oxygen plasma. The remains of the PDMS uncross-linked enough at the interfaces between layers form an effective bond at the low temperature (2h @ 75 ° C)[134,135].This method provides an inexpensive, rapid, non-cleanroom, permanent bonding for integrating the sensor.

To create the PDMS lid, the PDMS prepolymer and curing agent (DOW Sylgard 184) were thoroughly mixed in a volume ratio of 25:1 to create a smooth and adjustable lid to the channel surface, followed by a degassing for 10 min to remove the air bubbles. The degassed PDMS mixture was gently poured onto the poly(methacrylate) PMMA mold (Fig.3.11a). The PMMA piece was designed with two inlet holes for the reservoirs of the microchannels (Fig. 3.11b). Then, the PDMS was cured at 70°C for 2h on a hot-plate (KW-4AH, Chemat Technology Inc, United States). Finally, the cured PDMS was carefully removed from the mold manually

Two through holes were perforated on each reservoir with a biopsy punch (Harris Uni-CoreTM 1 mm I.D, United States) for external access of tubing connections (Fig.3.11c). As next step, the polymer replica and the PDMS lid were exposed to oxygen plasma to clean the surfaces at 50 W, with a flow 45% for 1 min (Fig.3.11d). Immediately, the PDMS lid was carefully taken and positioned above the replica, the inlets were used to visually monitor the alignment between the surfaces. Gentle pressure was applied atop the mold to allow the full coverage of the PDMS lid over the replica surface and also to get rid of trapped air bubbles (Fig.3.11e). When the alignment was completed, the complete sensor was cured at 75°C for 2h on a hot-plate (Fig.3.11f).

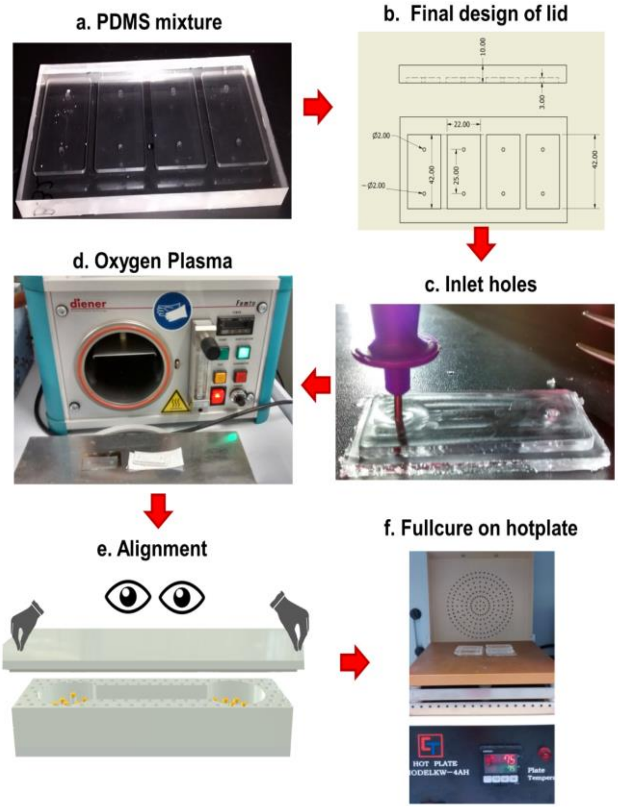

Figure 3.11. *Schematic illustration of the oxygen plasma bonding method.* **(a-b)** *PDMS lid at 25:1 ratio.* **(c)** *Activation of the surfaces by O_2 plasma* **(d)** *Holes perforated by a biopsy punch.* **(e)** *Visually alignment between the surfaces, and* **(g)** *Curing of the whole sensor device using temperature.*

3.5.1 Results and Discussion

Figs. 3.12 a-d show the photos of the flexible sensor devices achieved as a result of the bonding between the thin metallized polymer replica (thickness 279 ±25 μm) and the PDMS lid. Fig. 3.12e describes the experimental setup that includes a pump, with a syringe of 20 ml to assure a constant liquid flow through the microfluidics, thereby passing through a manual injection valve and the sensor. According to the dimensions of the microchannel (see Fig. 3.13a) the Reynolds number is 142.2 that corresponds to a laminar flow.

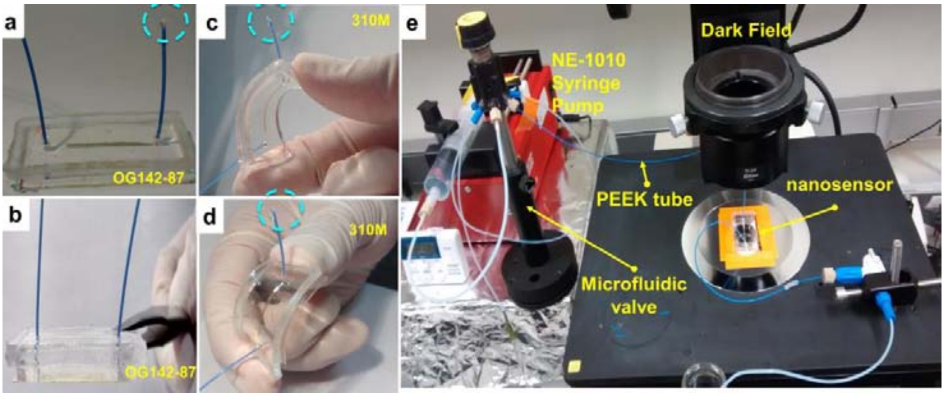

Figure 3.12. *Sensor with the microfluidic system.* **(a-d)** *Photos of the rigid* (OG142-87) *and soft* (310M) *sensors in contact with water.* **(e)** *Implemented experimental setup to test the pressure range of the sensor.*

Fig. 3.13b show a photograph of the soft (310M) sensor working with a solution of phenolphthalein which pink color helps to visualize the trajectory of the water from the microfluidic valve to the outlet of the sensor. Also, we can see the microscope images of the liquid flowing through the microchannel. Finally, four sensors of each material (OG142-87 and 310M) were fabricated to test the limit and reproducibility of the permanent bonding, the same flow rate was kept for 4 hours. Fig. 3.13c shows the graphic of the flow rate and pressure applied to the different sensors. According to the experimental results the permanent bonding of OG142-87 and 310M sensors work stably from 5 μl/min to 50 μl/min , but at 90 μl/min the bonding of both sensors (OG142-87 and 310M) breaks, producing water leakages.

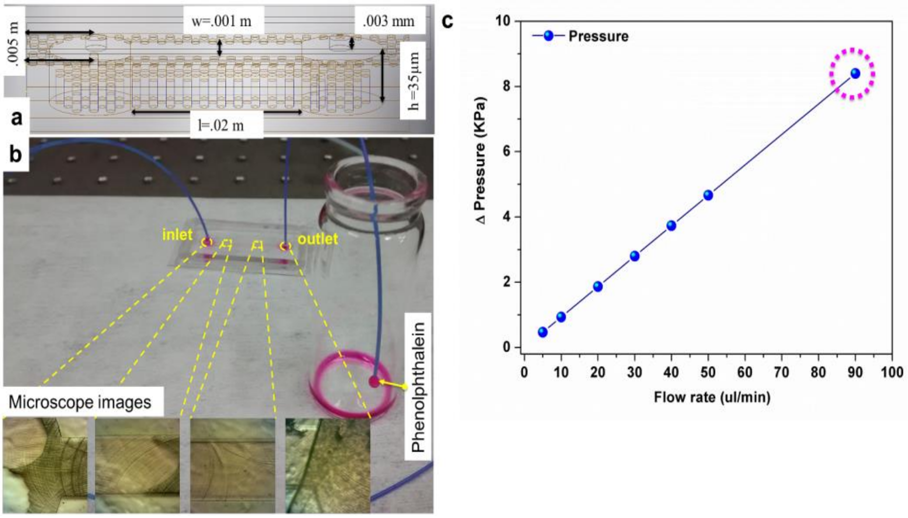

Figure 3.13. *Operation of the sensor.* **(a)** *Schematic view of the sensor dimensions.* **(b)** *310M sensor working with a phenolphthalein solution to indicate the water trajectory. The microscope imagens exhibit the flow through the canal.* **(c)** *Graph of the flow rate and pressures employed to test t the OG142-87 and 310M sensors.*

3.6 Conclusions

We have presented the fabrication of sensors formed by polymer nanopillars capped with gold nanodisks and integrated in a microfluidic channel using the replica molding technique. The controlled process to produce PDMS molds of nanoholes from the silicon master was described. The results showed the excellent combination of our protocol and the ability of the PDMS (Sylgard 184) to mold the Si nanostructures in the SU-8 channel to a large area. The use of PDMS molds is inexpensive and multiple copies can be replicated from the original master mold (around 25) without deformations, which make it attractive for effective and low cost sensor fabrication. The differences observed in the diameter values and the presence of defects can be explained by variations of the original master molds.

Different polymers with an increasing Young´s modulus were used to understand and investigate the replica molding limitations of polymer nanopillars when the gold nanodisks were placed on them. The results confirmed that the molding material and the aspect ratio play an important role in the success of the replica molding. We showed that the use of polymers

OG142-87 and 310M combined with our fabrication protocol were able to replicate the silicon nanopillars integrated in the SU-8 channel, with an aspect-ratio from 1.6 to 7.37. Spring constants from $9 \cdot 10^{-03}$ N/m to 2.5 N/m were approximately calculated to know both the mechanical stability (stiffness) of the polymer nanopillars to a shear stress, and the soft and rigid tissues that those spring constants could mimic according to the bibliography, if required. However, the height of the polymer nanopillars was lower than that of the silicon nanopillars due to distortions caused by incorporation of the gold nanodisks.

On the other hand, using the combination of the oxygen plasma with a partial curing of PDMS (25:1), the microfluidic integration of sensors with different heights, diameters and materials with an increasing Young´s modulus (OG142-87 and 310M) was possible. According to the dimensions of the microchannel and the water characteristics, the Reynolds number indicates a laminar flow. Experiments under different flow rates were carried out to test the pressure and duration of the permanent bonding. The permanent bonding was stable for a flow rate from 5 to 50 µl/min, breaking at 90 µl/min for both materials.

Finally, we expect that the mechanical characteristics (e.g., spring constant) of sensors can be useful not only to mimic biological structures but also to use as sensors with different mechanical sensitivity to shear stress. Thus the effect of a shearing force on the flexible nanopillars could cause changes in their orientation. Thereby, we expect this effect could also produce optical responses.

Chapter 4. Characterization of the sensor

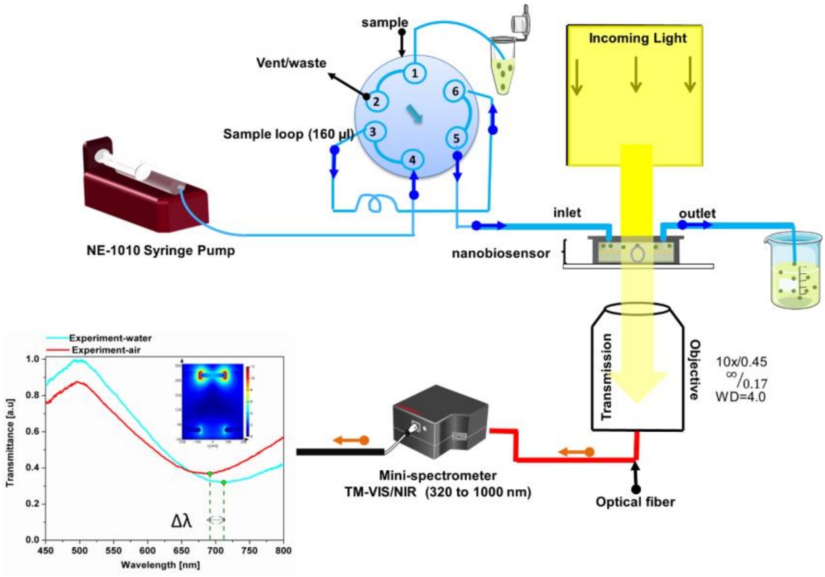

In this chapter: (i) *LSPR modes of a hexagonal array of the Au-capped polymer nanopillars (with and without perforated gold film) are simulated using FDTD calculations, and the results are verified experimentally*.(ii) *The bulk sensitivity of the sensors was examined by a set of serially diluted glycerol solutions with known RI.* (iii) *And the hydrophobicity of the sensors was evaluated by contact angle.*

4.1 Introduction

As mentioned in Chapter 3, we have developed a controlled methodology for the fabrication of sensors formed by Au-capped polymer nanopillars of different heights, diameters and materials (OG142-87 and 310M) with an increasing Young´s modulus, whose spring constants can range from 9E10^{-03} to 2.5 N/m. We believe that those characteristics could be used not only to mimic tissues but also to control the mechanical flexibility of the structures. In this chapter, we theoretically studied the LSPR properties, scattering, transmission spectra and the electric field distributions at normal incidence of the Au-capped polymer nanopillars with a gold film, using the 310M (S1b sensor) short nanopillars as model for finite-difference-time-domain (FDTD) calculations[136]. Following a step by step approach, LSPR modes of a hexagonal array of the Au-polymer nanopillars (with and without Au film) were simulated. Also, we theoretically studied the influences that diameter (±standard deviation) of Au nanodisks generate on the transmission measurement. Additionally, the theoretical spectra (air and water) were also verified experimentally by depositing a water droplet on the polymer nanopillars, to prove the optical operation of the sensor. The bulk sensitivity of different designed sensors was tested experimentally by set of serially diluted glycerol solutions with known RI. On the other hand, the sensor hydrophobicity and capillary forces were also tested by contact angle.

4.2 Sensors Design

Two new silicon master molds of arrays of Si nanopillars (SiNPs) with an increasing aspect ratio, integrated into the SU-8 channels, were specially fabricated to study the influence that the aspect-ratio of the structures and material have on the optical and mechanical properties. We bealive that after this study, it will be posibble to choose the most suitable design for the optomechanical sensor and its applications. The silicon master molds were designed with a similar diameter, varying the height, with a distance center to center of 400 nm. They were then replicated from the corresponding PDMS molds using the polymers epoxy 310M and OG142-87 by replica molding process. Gold nanodisks were placed on top of them by e-beam (For further details, we refer to Chapter 3). Table 4.1 compares the experimental aspect-ratio of the polymer nanopillars capped with gold nanodisks (thickness=25 nm), with their corresponding values of the silicon master. The average size parameters and standard deviations, extracted from the SEM images, are also included in Table 4.1. Moreover, Table 4.1 shows the spring constant (k) that the Au-capped polymer nanopillars produce according to their aspect ratio, and the Young´s Modulus of the material (See Annex A). As mentioned above, the size of the 310M (S1b sensor) short nanopillars was used to create the model for the FDTD simulation as they are the first in being fabricated.

Table 4.1. *Comparison of experimental results of aspect ratios of a hexagonal array of Au-capped polymer nanopillars embedded in the polymer microchannel with a center-to-center distance of 400 nm. Average and standard deviation* (a±b) *from sensors created using the Si masters and the 310M and OG142-87 polymers by replica molding protocol.*

	Silicon nanopillar d_{cc} =400 nm			**EPOTEK-310M (4.16 MPa) d_{cc} =400 nm**				**EPOTEK-OG142-87 (3.59 GPa) d_{cc} =400 nm**			
	dr^{a} (nm)	h (nm)	aspect ratio	d_{pnp} ^{a}(nm)	h (nm)	aspect ratio	Spring constant [N/m]	d_{pnp}^{a} (nm)	h (nm)	aspect ratio	Spring constant [N/m]
S1	167.5± 11.1	294.0 ± 46.2	1.75	160 ± 10.8$^{\mathbf{b}}$	320 ± 115.1	2.09	1.19 E-02 **Muscle**	185.8 ± 18.0$^{\mathbf{c}}$	490 ± 131.6	2.63	5.35 E+00 **bone**
S2	165.7± 11.5	588.6 ± 122.1	3.55	163.6 ± 13$^{\mathbf{b*}}$	468.7 ± 58.6	2.86	4.27 E-03 **liver**	195.6 ± 18.7$^{\mathbf{c*}}$	512.5 ± 67.6	2.61	5.75 E+00 **bone**

[a] Botton diameter from SEM images is used for calculation.
d_r reduced diameter of silicon nanopillar
d_{pnp} diameter of polymer nanopillar
d_{cc} center to center distance
b, 310M (S1b sensor) short nanopillars replica of the sample S1 with the polymer epoteck-310M, [c] OG142 (S1c sensor) short nanopillars replica of the sample S1 with the polymer epoteck-OG142-87
b*, 310M (S2b sensor) tall nanopillars replica of the sample S1 with the polymer epoteck-310M, [c*] OG142 (S2c sensor) tall nanopillars, replica of the sample S1 with the polymer epoteck-OG142-87

4.3 Theoretical study: optical simulation of the sensor

Simulation

Fig. 4.1a shows the geometry of the hexagonal array of polymer nanopillars (PNPs) in the FDTD model. As mentioned above, such geometry established according to the 310M (S1b sensor) short nanopillars with gold film observed in the SEM images, as shown in Figs. 4.1 (b) and (c). In the FDTD model, a cylinder with a d_{pnp}=160 nm and thickness of 25 nm were used to approximate the Au nanodisks (yellow) on the short polymer nanopillars (EPOTECK-310M) with a height h≈320 nm and with a center-to-center distance (d_{cc}) of 400 nm (green). Also, the yellow film was used to simulate the Au film (25 nm). Unless otherwise noted, values above of

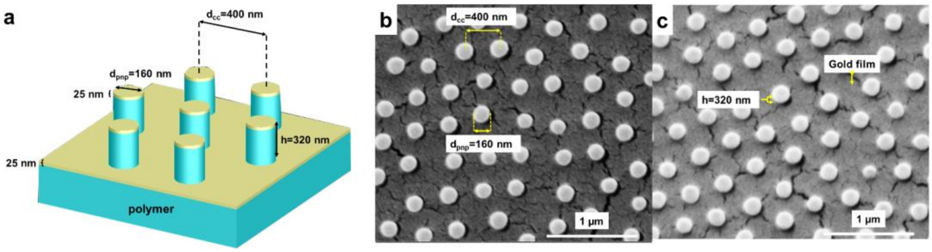

Figure 4.1. **(a)** *A modeled array of the Au polymer nanopillars: yellow represents Au metal, while green stands for polymer (n=1.49). A cylinder with a* d_{pnp}*=160 nm and thickness of 25 nm are used to approximate the Au nanodisk on the short polymer nanopillar with an h=320 nm, and with a center-to center- distance of 400 nm (dcc). These values are chosen referring to real PNPs observed in* **(b)** *and* **(c)** *of the sample named 310M short nanopillars(S1b), see* Table 4.1. *Top-view* **(b)** *and* **(c)** *15º tilt-view SEM images of Au polymer (EPOTECK-310M) nanopillars. The substrate is covered by a gold film with holes down the PNPs, whose diameters correspond to the diameter of the nanopillars; the deposition thickness of Au film is also 25 nm.*

the geometry parameters described in the caption of Fig. 4.1 of the 310M (S1b sensor) short nanopillars, used in the simulations of a hexagonal array of the Au-polymer nanopillars with and without gold film. Throughout all simulations, optical constants of Au reported by Johnson and Christy were used.

The polymer was modeled (green) by its complex refractive index (n=1.49). EM field profiles and scattering/transmission spectra are calculated with 1 nm mesh accuracy in air and water (n=1.3331). For transmission a polarized broadband light source (plane wave, 400-1000 nm) was placed above and in a normal direction through the nanopillars array. The detector was placed down the nanopillar array. For scattering measurements a polarized broadband light source (TFSF source, 400-1000 nm) was located above and in a normal direction through the nanopillars array. The detector was placed above the nanopillar array and the light source. Finally, the EM field distribution (cross-section) was only calculated for the central pillar of the hexagonal array to reduce the computational requirements .

4.3.1 LSPR of the array of Au capped polymer nanopillars in air

The real configuration of the optomechanical sensor is a hexagonal array of Au-capped polymer nanopillars with an Au film. This complex shape was divided in three cases to understand the contribution and effect on the scattering and transmission spectra: i) A hexagonal array of nanoholes formed in the base of the nanopillars (see Fig.4.2a). ii) A hexagonal array of Au-capped polymer nanopillars with the Au film (see Fig. 4.2b). And iii) a hexagonal array of Au-capped polymer nanopillars without the Au film. Those configurations were theoretically studied to investigate the positive or negative influence of the Au film on the optical properties (see Fig.4.2c).

First, scattering spectra are calculated not only for the array of nanoholes but also for Au-capped polymer nanopillars with and without gold film (in air). Results are shown in Fig. 4.2. For the array of nanoholes in the gold film, the LSPR peak appears at 840 nm (P2'), whereas it appears at 654 nm (P1') for the array of Au disks on the nanopillars but without gold film. The spectrum is blue-shifted when the array of nanopillars support the Au disks whereas it is red-shifted with nanohole configuration. Furthermore, it can be observed that the FWHM of the resonance peak of the array of PNPs without gold film (80 nm) is less than the array of nanoholes (108 nm), see Figs. 4.2a,c.

Next, we performed the scattering simulations for the structure that contains a hexagonal array of the Au-capped polymer nanopillar with a gold film, see Fig.4.2b. We can notice that there are two peaks and one dip. The simulations describe that the electric field distribution at P1 (706 nm) is localized around the Au nanodisks (Fig. 4.2h). The simulations for the array of Au nanopillars but without the gold film (Fig. 4.2c) exhibit a strong peak P1', which has nearly the same spectral position and field distribution (Fig.4.2k) as P1, confirming that P1 is the LSPR arising from the gold nanodisks. For the peak P2 (902 nm), the electric field is mainly distributed in the gold hole (Fig.4.2j). To confirm P2, we can see in Fig. 4.2a that in the scattering spectrum of the array of nanoholes there is a peak P2', which is caused by the LSPR of the gold nanohole (Fig. 4.2g). Finally, the dip D at 790 nm, in Fig. 4.2b can arise of the LSPR of the gold nanoholes and nanodisks as shown in the electric field distribution of Fig. 4.2i.

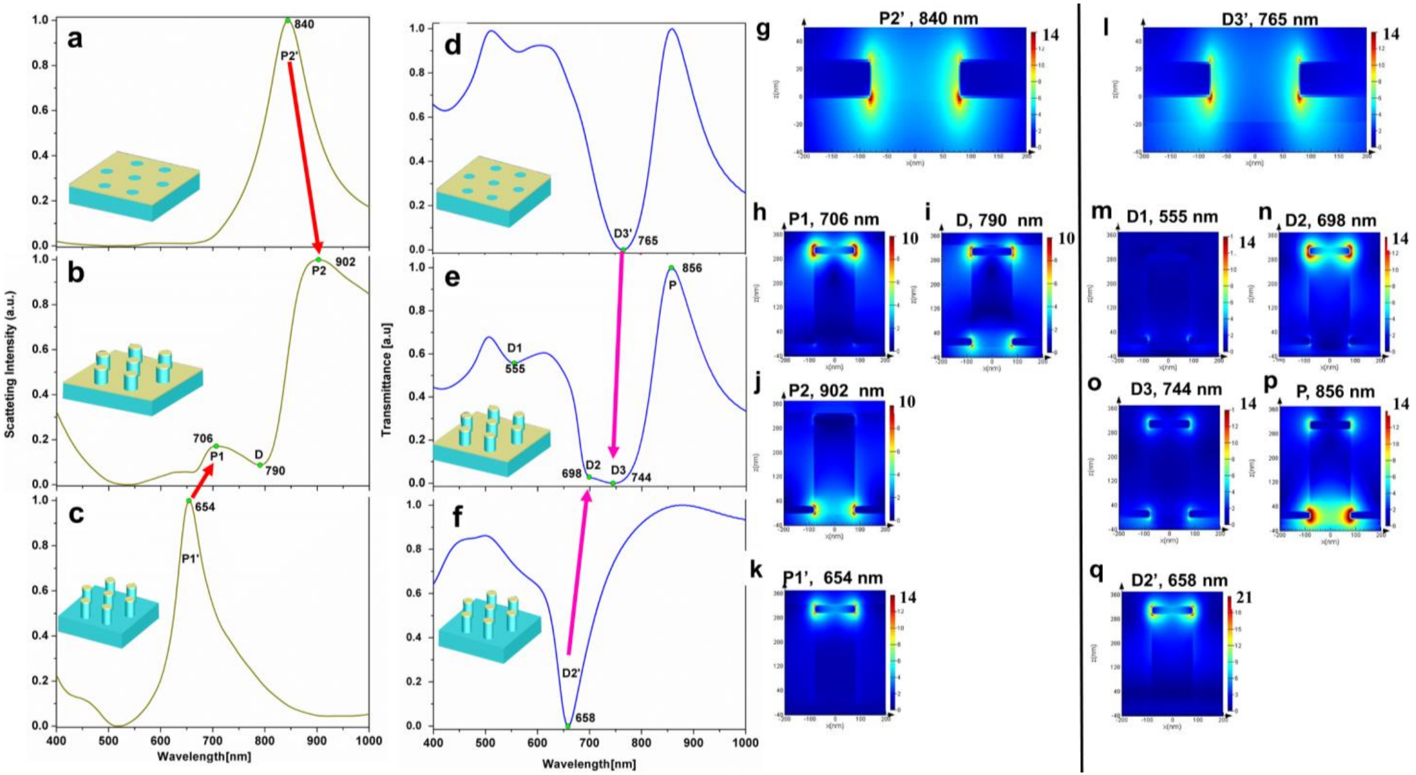

Figure 4.2. *Scattering, transmission and electric field distribution at normal incidence in air.* **(a)** *and* **(d)** *simulated scattering and transmission spectra for the structure composed of only an array of nanoholes in a gold film, the diameter of the nanoholes correspond to the diameter of the 310M short polymer nanopillar (dnpn=160 nm) and the thickness of the gold film is 25 nm.***(b)** *and* **(e)** *simulated scattering and transmission spectra for the structure composed of an array of polymer nanopillars with a gold film (dnpn=160 nm, h=320, Au thickness =25 nm).* **(c)** *and* **(f)** *calculated scattering and transmission for an array of gold capped polymer nanopillars but without gold film.***(g-q)** *Simulated electric field intensity distributions for the peaks and dips of the spectra, respectively. The insets in* **a-f** *show the schematics of the corresponding structures.*

To understand the resonant mode of the polymer nanopillars structures, we used the FDTD software to simulate the transmission spectra and the electric field distributions of the structures at normal incidence. The results of the simulations are shown in Figs.4.2d-f. We can see in Fig. 4.2e that there are three dips and one peak in the simulated spectrum. For the array of nanoholes (Fig. 4.2d), the LSPR peak appears at 765 nm (D3’), whereas it is at 658 nm (D2’) for the array of Au disks on the nanopillars without gold film (Fig. 4.2f). It can be observed that the FWHM of the resonance peak of the array of polymer nanopillars without gold film (88 nm) is less than for the array of nanoholes in the gold film (130 nm), see Figs. 4.2d and f.

Then, Fig. 4.2m shows the electric field distribution at dip D1 (555 nm). It is slightly distributed in the vicinity of the nanohole. Also, Fig. 4.2n shows the electric field distribution at D2 (698 nm), which is localized around the gold nanodisks. The simulations for the array of Au nanopillars but without the gold film (Fig. 4.2f) exhibits a strong dip D2’, which has nearly the same spectral position and field distribution (Fig.4.2q) as D2, confirming that D2 is the LSPR arising from the gold nanodisks.

Compared with D3’ (Fig. 4.2d), D3 of the Au-capped nanopillar with gold film (Fig. 4.2e) is shifted at 744 nm, which is believed to be caused by the LSPR of the Au nanodisks on the nanopillars. Then D3 is described as the LSPRs of the array of nanoholes and the Au nanodisks on the polymer nanopillars, as the electric field distribution in Fig. 4.2o shows. Also, it is observed that Fig. 4.2e exhibits a peak P at approximately 856 nm, which we try to identify by simulation. Fig. 4.2p shows the simulation result where a localized electric field distribution around the Au nanodisks and the nanohole is observed. P has field features similar to those of D3’ but has a larger hotspot region.

Then, the simulations not only show that the LSPR spectra are generated but also that the Au film (nanoholes) creates a complex spectrum. According to the simulations, in the real configuration of the sensor, the scattering, and the transmission, depending the wavelength, are dominated by both the Au-capped polymer nanopillars and the nanoholes formed in the gold film.

This means that the interpretation of any LSPR shift due to a change in the refractive index of the medium will be complex. A sensor configuration avoiding the Au film would be more suitable for the purpose of this thesis.

4.4 Experimental characterization of the optical properties of the sensor

4.4.1 Experimental set-up measuring scheme

DF microscopy in transmission mode offers a very reliable technique for the acquisition of scattering spectra of single nanoparticles. This method operates in a very similar way as a conventional microscope. The difference is hidden in the use of a dark-field (DF) condenser, which is placed between the excitation light source and the sample. The DF condenser forms a hollow cone of light focused on the sample. The only light that is scattered out of this cone reaches the objective (which must have a smaller numerical aperture than the condenser). Thus, the DF condenser blocks all the incoming light angles that otherwise would travel right into the objective. A diagram of the experimental arrangement is shown in Fig. 4.3a.

In our approach, we employed an inverted Nikon inspection microscope (Eclipse Ti-U, Fig. 4.3b), equipped with a halogen light source (100 W) and fiber-coupled (øF=1000 µm) to a mini-spectrometer (TM-VIS/NIR, Hamamatsu (320 to 1000 nm)). It was utilized to obtain scattering and also transmission spectra of the sensors, which are formed of gold capped polymer nanopillars with a gold film. DF condenser (Dry N.A. 0.95-0.80, Nikon) was employed to send light to the sensors (Fig. 4.3c). The transmission spectra are measured when the condenser is removed from the excitation light source and the sample (Fig. 4.3d). The sensor is placed as shown in Fig. 4.3e. It possesses an inlet and outlet that serves as connections for the fluidics they were employed to carry out the sensitivity measurements with microfluidics as shown in Figs. 4.3f and g. A microfluidic pump with adjustable pumping speed was used to assure a constant liquid flow through the microfluidics, thereby passing through (manually operated) an injection valve and to the sensor. A schematic drawing of the experimental setup, containing all the major components, can be observed in Fig. 4.4.

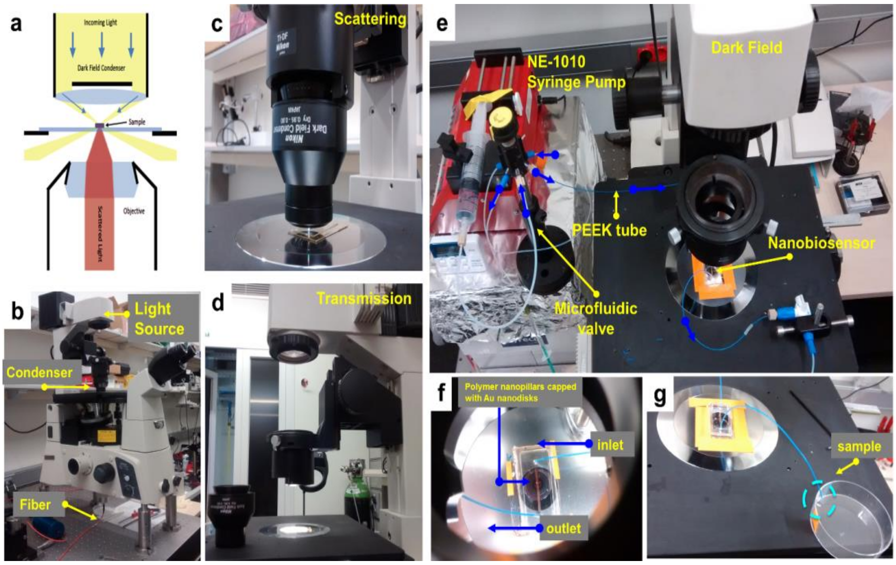

Figure 4.3. *Experimental arrangement for dark-field microscopy.* **(a)** *Schematic of an inverted dark-field transmission spectroscopy setup.* **(b)** *Photograph of the inverted Nikon Eclipse Ti-U microscope employed.* **(c)** *and* **(d)** *Configuration of the DF microscope for scattering and transmission measurements, respectively.* **(e)** *Top-view photograph of the experimental measuring scheme.* **(f)** *and* **(g)** *show a sensor with an inlet and outlet that serves as connections for the fluidics.*

The experiments were performed by first recording the LSPR spectra (area with a diameter of 100 µm (ca. 7500 um^2)) of scattering or transmission through an optical fiber (1000 µm) from the DF microscopy (objective 10x) to the spectrometer,as can be seen in Figs. 4.4a and b. For data acquisition, the commercial software, SpecEvaluationUSB2, supplied with the mini-spectrometer was used. Normalized scattering or transmission spectra (Is) were obtained by subtracting the previously stored dark spectrum (ds) from the data received from the mini-spectrometer, and dividing by a previously stored reference spectrum (Rs). The acquisition times for the spectra ranged from 2 s to 4 s with 500 spectral accumulations, depending on the sensor. The spectra were saved for analysis using Matlab and OriginLab software. Then, the spectral LSPR dip position (λLSPR) was carried out a posteriori. For this, a high-degree polynomial (N=20) was fitted to the previously acquired transmission spectra, using a home-made script in Matlab. The script calculates the minimum values of the spectra (λLSPR), and then are exported to be plotted as function of time in the OrigingLab software (see Annex B).

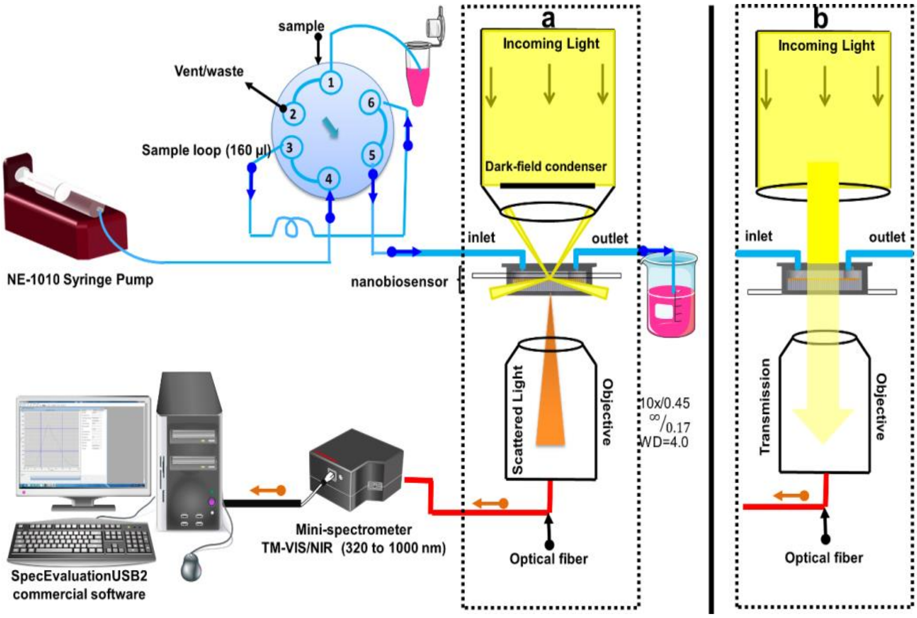

Figure 4.4. *Schematics of the employed experimental DFconfiguration.* **(a)** *Dark-field scattering experimental setup using a high-numerical aperture dark-field condenser and a low-numerical aperture microscope objective for scattering evaluation.* **(b)** *Schematic of the geometry for transmission evaluation.*

4.4.2 LSPR scattering and transmission spectra of sensor in air

The 310M (S1b sensor) short nanopillars were selected for the experimental studies because the previous FDTD simulations used them as model. As above described, the nanopillars have a diameter d_{pnp}≈160 nm and height of 320 nm, separated center to center 400 nm (see Fig. 4.1). Importantly, the experimental measurements were performed without the lid of the microfluidic channels (air).Then, the sensor was placed in the DF microscopy for scattering and transmission measurements as shown in Fig. 4.3c, and in Fig. 4.3d, respectively.

Fig. 4.5a and c show the calculated scattering and transmittance spectra for the 310M (S1b sensor) short nanopillars. We can see in the dashed rectangles the range of the wavelength employed to compare the experimental measurements as the Fig. 4.5b and d show, respectively. The range of the wavelength was delimited because the spectra are distorted by the noise (electronic) of the DF microscopy during the acquisition of the data.

For scattering spectra, Fig. 4.5b shows that the experimental spectrum is slightly red-shifted and broader. It can be seen that the P1 at 706 nm is red-shifted, according to the simulations of the electric field distribution, it corresponds to LSPR arising from the gold nanodisks (Fig. 4.2h). Therefore, both the dip D at 790 nm that corresponds to the LSPRs of the gold nanoholes and nanodisks (Fig. 4.2i), and the peak P2 (902 nm), that corresponds to LSPR of the gold holes (Fig.4.2j) are also red-shifted. One can attribute the red shift to the fabrication process, which inevitably would result in Au nanodisks on the nanopillars with different diameters, leading to a weak resonant frequency than in the case of perfect Au nanodisks on nanopillars.

For transmittance spectra, the spectrum of the simulation was in good agreement with the experimental transmittance spectrum obtained from the corresponding first peak and dip (D2) positions of the array of Au-capped polymer nanopillars with gold film as shown in Fig. 4.5d. In the graph, the experimental spectrum is distinctly broader (red curve). It is reasonable to think that this effect is due to the fabrication process. Also, we can notice that the dip D1

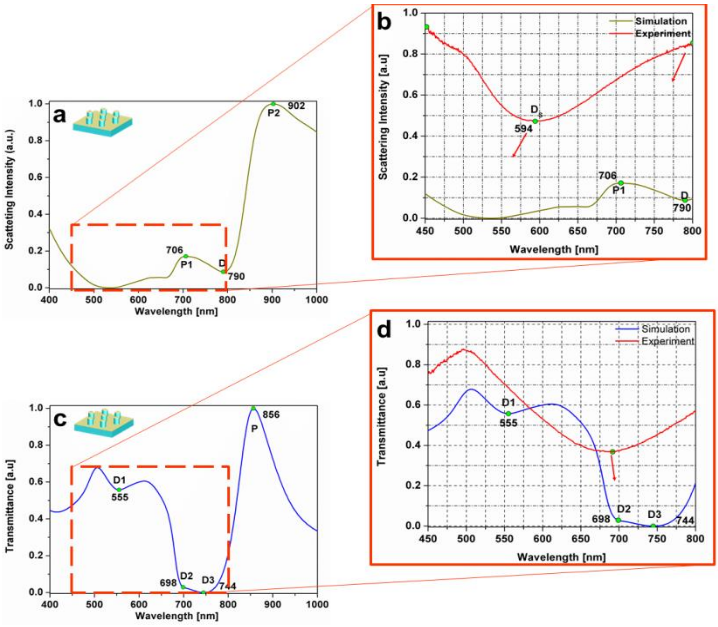

Figure 4.5. (a) *and* **(c)** *Scattering and transmission spectra at normal incidence in air for 310M (S1b sensor) short nanopillars.* **(b)** *Experimental (red) and calculated (green) scattering spectra of the 310M(S1b sensor)short nanopillars.* **(d)** *Experimental (red) and calculated (blue) transmission spectra of the 310M(S1b sensor) short nanopillars.*

(555nm) does not appear in the experimental spectrum, which according to the simulations of the electric field distribution, corresponds to a slight distribution of the electric field in the nanohole vicinity, as shown in Fig. 4.2m.

Then, the experimental spectrum exhibits a strong dip at 698 ±6.5 nm, which has the same spectral position as D2 (698 nm). The simulations confirm that D2 is the LSPR arising from the gold nanodisks with a slight contribution of nanoholes, as shown in Fig. 4.2n. We think that due to the quality of the fabrication process, the D3 (744 nm) does not appear in the experimental spectrum. Also, we can see that after D3, both the experimental and simulation spectra increase ,and according to the simulations of Fig, 4.5c, the transmission spectrum forms the peak P (Fig. 4.2p). However, the peak P was not possible to be observed experimentally due to the limitations of spectrometer.

4.4.3 Influence of the nanopillar diameter in the optical properties in air

Given the previous results of the scattering and transmission spectra, we considered necessary to confirm the significant impact of the deviation standard of the diameter of the Au nanodisks, on the optical properties, due to the methodology of fabrication. Our manufacturing process leads to two main distortions of the Au nanodisks on the polymer nanopillars: i) in the unmold step we observed that the polymer nanopillars adopt the orientation in which are separated from the PDMS mold. ii) the temperature, at which the different polymer nanopillars were exposed during the deposition of the gold nanodisks by e-beam (See Chapter 3). Then, using FDTD simulations, we demonstrate that the deviation standard (std) of the diameter of gold nanodisks is responsible for significant modifications of the LSPR properties. The SEM images reveal the different size of the diameters of the Au nanodisks, as can be seen in Fig. 4.1.

The scattering and transmission spectra were calculated, with the same conditions of the previous simulations. We continue using the 310M (S1b sensor) short nanopillars with a gold film whose diameter (d_{pnp}) is 160±10.8 nm, with a height of 320 nm, and a center to center distance (d_{cc}) of 400 nm. We keep the height and separation distance but a simulation used the diameter +std (170.8 nm), and the other used the diameter –std (149.2 nm).

Fig. 4.6a shows the scattering spectra for the different size of diameters (160±10.8 nm). It can be seen that the simulated spectrum using the +Std of the diameter of the nanopillars is slightly red-shifted and broader (orange curve). The peak P1 at 706 nm is shifted by +6 nm and the peak P2 at 902 is shifted by +17 nm. Also, we observed that the intensity of P1 slightly increases. On the contrary, the simulated spectrum using the -Std of the diameter is slightly blue-shifted and broader (pink curve). It is clearly shown that the P1 and P2 are shifted by -10 nm and -33 nm, respectively. In other words, with a large diameter of disk, the LSPR spectrum moves to the right and with a small diameter to the left.

Fig. 4.6b presents an interesting comparison between the scattering spectrum of the simulation using the diameter of 160 nm (green curve) and the average of the spectra of simulations using the diameters of ±std (black curve). It can be noticed that spectra agree well with each other in the prediction of the peak and the dip position. Therefore, it demonstrates not only the influence of the size of the diameter of the Au nanodisks over the LSPR position but also that the experimental scattering spectrum (Fig. 4.6b) is the result of an average of the size of the fabricated structures.

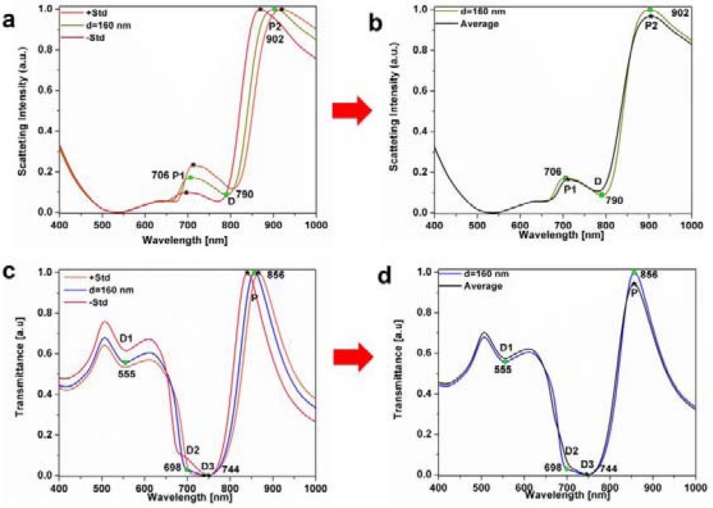

Figure 4.6 (a) *and* **(c)** *Scattering and transmission spectra of the average of the diameter of the 310M short polymer nanopillars (160 nm) and its ±standard deviations (sensor S1b).* **(b)** *and* **(d)** *Comparison between the scattering and transmission spectra from the simulation using the diameter of 160 nm, and the average of the simulations from diameter of ±Std.*

Fig. 4.6c shows the transmission spectra for the different diameters size (160±10.8 nm). Here, the spectrum using 170.8 nm of diameter moved to the right (orange curve). The peak P at 856 nm is shifted by +9 nm and the dip D3 at 744 nm is slightly shifted by +6 nm. Also, we observed that D2 does not appear. On the contrary, the spectrum from the simulation using the -Std of diameter (149.2 nm) moved to the left (pink curve). We can see that P and D3 are shifted by -16 nm and -5 nm, respectively. We also observed that D2 is shifted by -20 nm. Finally, for the case of D1, the position is not affected, only the intensity.

Fig. 4.6d presents the comparison between the transmission spectrum of the simulation using the diameter of 160 nm (blue curve), and the average of the simulations using ±Std of the diameter (black curve). We can notice that spectra agree well with each other in the prediction of the peak and the dip position. Also, we can see that D2 disappears thereby the dip D3 is best defined.

Then, the FDTD simulation demonstrates not only the influence of the size of the diameter of the Au nanodisks over the LSPR position and shape in the transmission spectrum but also that the transmission is less affected than scattering by the defects and the variations of size of the nanostructures of the complex configuration of the sensor.

4.4.4 LSPR scattering and transmission spectra of sensor in water

The study of the LSPR spectra of the sensor, when the medium changes from air to water, is crucial because it proves that the Au-capped polymer nanopillars work as a refractometric sensor. The study also provides information on the behavior of spectra and its sensitivity. The 310M (S1b sensor) short nanopillars are placed between the excitation light source and the objective of the DF microscope, as shown in Fig. 4.3c for scattering and in Fig. 4.3d for transmission. Next, a water droplet (5µl) is deposited on the polymer nanopillars (d_{npn}≈160 nm, h≈320) to examine the behavior of the spectra due to the change in the refractive index of the dielectric medium (Fig 4.7m).

Fig. 4.7a shows the simulated scattering in air (green, n=1) and water (dark cyan, n=1.3331) for the hexagonal array of 310M short nanopillars with the gold film. We can see that the P1 at 706 nm that corresponds to the LSPR arising from the gold nanodisks (Fig.4.2h) is significantly blue-shifted by -119 nm. The simulations show that the electric field distribution at 587 nm is slightly spread in the vicinity of the nanohole (Fig. 4.7d). Also, the dip D at 790 nm is red-shifted by +22 nm. The electric field distribution at 812 nm shows that it has a localized electric field distribution around the nanohole and also around the Au nanodisk, but with a larger hotspot region (Fig. 4.7e). The P2 at 902 nm that corresponds to LSPR of the nanoholes is red-shifted by +98 nm. Fig. 4.7f shows the electric field distribution at 1000 nm; which is localized around the nanohole and slightly around the nanodisk.

By comparing the simulation (black cyan) and the experimental (cyan) spectrum in water (n=1.3331) from 450 nm to 800 nm, we can infer that the spectra agree well with each other in the prediction of the dip and peak position, as shown the Fig. 4.7b. We can see that the peak at 587 nm is slightly blue-shifted. We can attribute the blue-shift to size differences of the fabricated structures. Finally, Fig. 4.7c shows the experimental spectra in air (red) and water (cyan).

A second phase of the study was the transmission analysis. Then, the Fig. 4.7g shows the simulated transmission in air (blue, n=1) and water (dark cyan, n=1.3331) for the hexagonal array of 310M short nanopillars with the gold film. We can see that the simulated spectrum for water (dark cyan) is slightly red-shifted and broader. Also, the D1 at 555 nm and D2 at 698 nm disappear.

LSPR scattering and transmission spectra of sensor in water

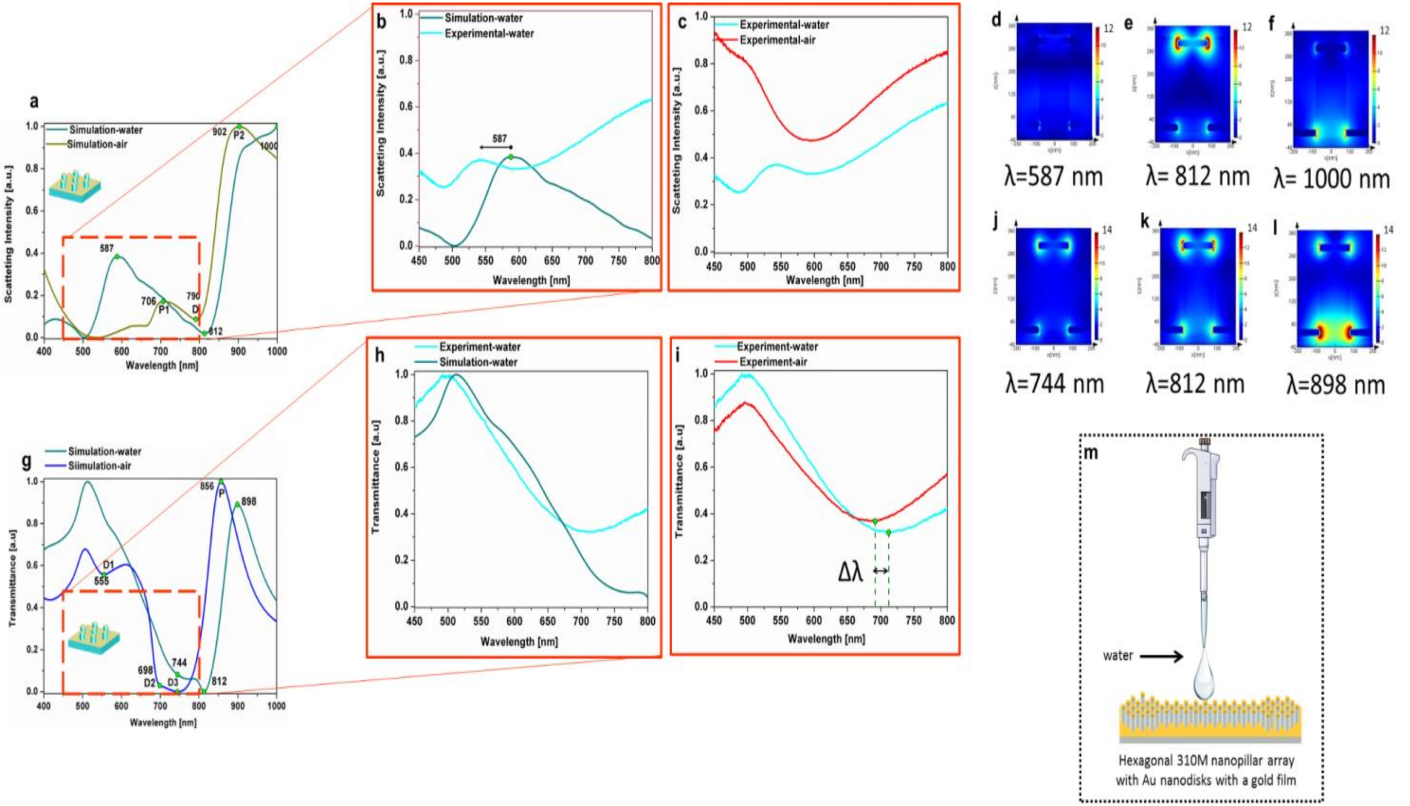

Figure 4.7. **(a)** *and* **(g)** *calculated scattering and transmission spectra, respectively for the structure composed of an array of polymer nanopillars with a gold film (dnpn=160 nm, h=320, Au thickness =25 nm) in air (n=1) and water (n=1.3331).* **(b)** *and* **(h)** *experimental (cyan) and simulated (dark cyan) scattering and transmission spectra in water, respectively.* (c) *and* (i) *experimental scattering and transmission spectra in air (red) and in (cyan).* **d-f,j-l** *Simulated electric field intensity distribution for the peak and dips, respectively. (m) Schematic showing the hexagonal array of polymer nanopillars with gold nanodisks on top, and the gold film, when a water drop is deposited on them to examine the spectra change.*

We calculated the electric field distribution at 744 nm (D3) to examine this change. According to the previous simulations in air, it is described to be due to the LSPRs of the array of nanoholes and the Au nanodisks on the polymer nanopillar (Fig. 4.2o). Now, the result in water describes a pattern similar to that of D3 but with a larger hotspot region in the gold nanodisk, as shown the Fig.4.7j. Interestingly, we can see that D3 is red-shifted at 812 nm by +68 nm, the simulation of the electric field also presents a pattern similar to D3 but with the largest hotspot region in the gold nanodisk as shown in Fig. 4.7k. The peak P at 856 nm is also red-shifted by +42 nm. The electric field at 898 nm has a pattern similar to P (Fig. 4.2p) but with a large hotspot region in the Au nanodisks (see Fig. 4.7l). This could be caused by the LSPR of the upper Au nanodisks and the nanoholes of the gold film.

Importantly, from those FDTD calculations in air and water, we can determine the theoretical sensitivity s_B defined as the ratio of resonant wavelength shift ($\partial\lambda_{res}\,[nm]$) to the variation of surrounding refractive index ($\partial n_s[RIU]$). Therefore, the sensitivity of 310M (S1b sensor) short nanopillars is given by $68\ /0.3331 = 204.14\, nm/RIU.$

Now, by the comparison of the simulation and experimental results in water (n=1.3331) one can infer that the experimental spectrum matches well in the range of wavelength that LSPR is arising from the array of nanoholes and the Au nanodisks on the polymer nanopillar (see Fig. 4.7h).

Finally, Fig. 4.7i shows the experimental spectra in air (λ_{LSPR} =691.61 nm) and water (λ_{LSPR} =711.84 nm), which is red-shifted by +20 nm. A slight increase in amplitude for the spectrum in water is also observed.

Taking the previous study into account, we verified that the experimental scattering and transmission spectra shifted by a change in the refractive index in the surrounding medium, demonstrating the operation the plasmonic sensor. In particular, the LSPR in the transmission spectra in air and water are useful for application in sensing, and then the theoretical sensitivity was calculated. In the case of the scattering measurements, this could be inaccurate due to the limitations of our spectrometer and the electronic noise of the DF microscopy, and then we need to measure in a wide range to see the whole spectrum.

4.4.5 Bulk sensitivity evaluation of the sensor

The evaluation of the bulk sensitivity is of paramount importance for knowing the performance of the device as a sensor. In order to evaluate the bulk sensitivity of a sensor device the standard procedure is to introduce successive solutions of known concentrations with different index values. After monitoring the sensor response to all the solutions, the data are plotted versus the concentration and fit by a linear regression to calculate the sensitivity of the sensor in nm/RIU. The sensitivity (S_B) is extracted from the slope of linear fits through the obtained data points $(\Delta\lambda_{\mathrm{LSPR}}\ vs.RI)$.

To examine the bulk sensitivity of the arrays of polymer nanopillars with gold nanodisks and film as a refractive index sensor, we performed transmittance measurements at normal incidence as shown in Fig. 4.4b. Three different sensors with different aspect ratio and spring constant were evaluated to find out the possible effect of their characteristics on the device sensitivity. The sensor were OG142 (S1c sensor) short nanopillars (d_{pnp}=185 nm, h=490 nm) with a spring constant of 5.35 E^{+00} [N/m], OG142 (S2c sensor) tall nanopillars (d_{pnp}=195 nm, h=512 nm) with a spring constant of 5.75 E^{+00} [N/m] , and 310M (S2b sensor) tall nanopillars (d_{pnp}=163 nm, h=468 nm) with a spring constant of 4.27 E^{-03}[N/m].

Four samples with different concentrations of glycerol were prepared and their refractive index was measured by a refractometer (ABBE model 315, UK). The samples were 2.5 % (Δn≈0.0032), 5 % (Δn≈0.0064), 7.5 % (Δn≈0.0096) and 10% (Δn≈0.0128) of glycerol. The serially diluted glycerol solutions with known RI were flowing over the sensors and the induced $\Delta\lambda_{\mathrm{LSPR}}$ was evaluated, while MilliQ water (n≈1.3331) was employed as a continuous running solution. All solutions were injected into the microfluidic system of the sensors at a speed of 10µL·min^{-1} as depicted in Fig. 4.4.

Fig. 4.8a,c, and e show the time-resolved responses of the sensors. As expected, all sensorgrams showed a stepwise increase in λLSPR response as the surrounding RI increase, which means the difference between the transmission light beams passing through the H_2O and the different solutions.

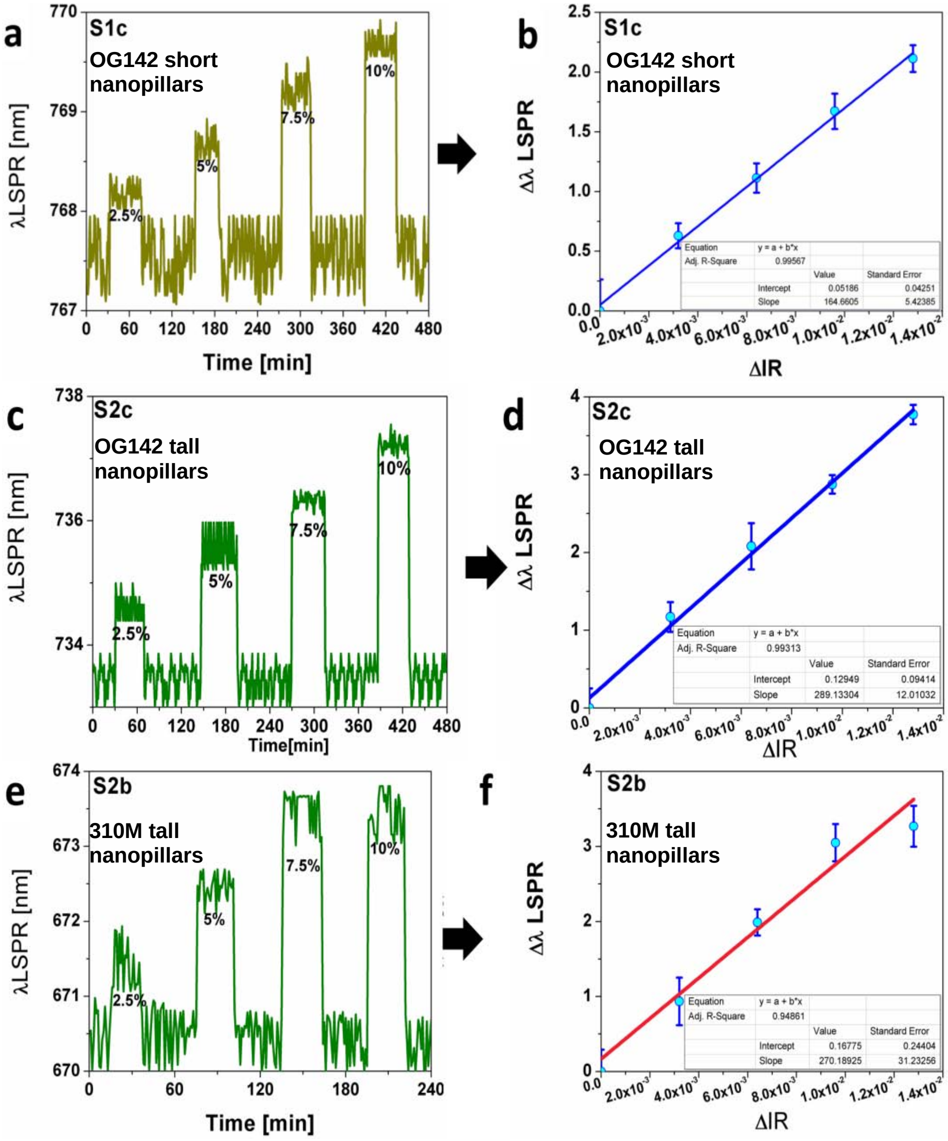

Figure 4.8. *Diluted glycerol experiments.* **(a), (c),** *and* **(e)** *Temporal sensors response to changes in the refractive index of the surrounding dielectric medium measured by transmission.* **(b), (d),** *and* **(f)** *Data plotted as a function of the RI variations* (Δn ≈ 0.0032 RIU) *showing linear dependence.*

Next, the values of λLSPR when the glycerol samples were in contact with the nanopillars were averaged and plotted as a function of the RI variations $(\Delta\lambda_{\mathrm{LSPR}}\ vs.RI)$ displaying a linear dependence as shown in Figs. 4.8b,d and f. Fitting to a linear regression function, we determined the (S_B) values for the sensors.

Figs. 4.8b,d and f describe the slope of effective sensitivities of the OG142 (S1c sensor) short nanopillars (164 nm/RIU), the OG142 (S2c sensor) tall nanopillars (289 nm/RIU) and the 310M (S2b sensor) tall nanopillars (270 nm/RIU), respectively (see Table 4.2).We intuit that the sensitivity of the OG142 (S1c sensor) short nanopillars is lowest due to the low height. On the other hand, the sensitivities of the OG142 (S2c sensor) and 310M (S2b sensor) tall nanopillars are higher than the S1c sensor, we believe that bulk sensitivities obtained are due to the high height and mechanical stability of the polymer structures. Those results suggest that the height of the nanopillars can help to expose the LSPR of the Au nanodisks to the dielectric environment and to access the glycerol molecules, thereby influencing on the sensitivity. Also, those values match with the some reported in the literature and have demonstrated to be useful for applications of sensing [30,109,114,137]. However, these values do not exceed the best sensitivity reported in the literature[112], see Table 4.2.

Table 4.2. *Comparison of sensitivity of the different sensors by changing the surrounding RI of the Au nanodisks of the polymer nanopillars with the gold film integrated into the microfluidic system.*

d_{cc}=400 nm	d_{pnp}^a (nm)	h (nm)	Aspect ratio	(S) (nm/RIU)	Material
Short (S1c)	185.8±18.0	490±131.6	2.63	164	OG142-87 (3.59 GPa)
Tall (S2c)	195.6±18.7	512.5±67.6	2.61	289	OG142-87 (3.59 GPa)
Tall (S2b)	163.6±13	468.7±58.6	2.86	270	310M (4.16 MPa)
Example	100	20	5	222	glass[109]
	230	150	1.5	375	Polymethyl methacrylate [114]
	285	510	.5	1000	Polymethyl methacrylate[112]

d_{pnp} diameter of polymer nanopillar
d_{cc} center to center distance

4.5 Contact angle of Au-capped polymer nanopillar arrays

The contact angle measurement is a good method to characterize surface wettability and is widely use for the study of hydrophobicity of surfaces. We evaluated the hydrophobicity of the sensors employed a contact angle apparatus (Kruss EasyDrop and the software Drop Shape Analysis). A single Mili-Q water droplet (5 µl) was deposited onto the surface of the 310M (S1b sensor) short nanopillars (d_{pnp}=160 nm, h=320 nm) and 310M (S2b sensor) tall nanopillars (d_{pnp}=163 nm, h=468 nm), and also on the OG142 (S1c sensor) short nanopillars (d_{pnp}=185 nm, h=490 nm) and OG142 (S2c sensor) tall nanopillars (d_{pnp}=195 nm, h=512 nm). A camera registers the droplet, and the software adjusts the shape of the drop to obtain the contact angle as shown in Fig.4.9a. Next, letting it evaporate also we can examine the effect of capillary forces on the Au-capped polymer nanopillar during the liquid drying step.

The contact angle data for the sensors are quoted in the SEM images of Figs. 4.9b-e. The contact angle of the 310M (S1b sensor) short nanopillars (34.3° ±.8) is larger than the 310M (S2b sensor) tall nanopillars (21.3° ±2). Similarly, the contact angle of the OG142 (S1c sensor) short nanopillars (90° ±.2) is larger than the OG142 (S2c sensor) tall nanopillars (76.7° ±2). One can infer that the large height of the 310M (S2b sensor) and OG142 (S2c sensor) tall nanopillars influences on the surface wettability of the polymer nanopillars. Then, they are considered hydrophilic and attractive for our purpose of sensing. Also, from SEM images it can be seen that after the evaporation of the water droplet on the nanopillars, the capillary forces caused that the gold-coated polymer nanopillars move the top part of their structure towards their nearest neighbors, as shown in Figs. 4.9b-e. We can notice that the 310M nanopillars (Figs.4.9 b-c) are more flexible and hydrophilic than the OG142 nanopillars (Figs. 4.9 d-e). The effect of the capillary forces generated between the vertical nanopillars and the liquid medium were larger for the samples of 310M (S1b sensor) short, 310M (S2b sensor) tall, and OG142 (S2c sensor) tall nanopillars than for the OG142 (S1c sensor) short nanopillars. The capillary-force induced structural deformation, especially for high-aspect-ratio nanopillars. For example, the sample of the 310M (S2b sensor) tall nanopillars was most deformed or bunched together as shown in Fig. 4.9c, whereas in OG142 (S1c sensor) short nanopillars, the structures are standing as shown in Fig. 4.9d.

Therefore, if we are able to prove a correlation between induced shear stress and the deformation experienced in the different polymer nanopillars and the variations on the optical response of the sensors this would prove their applicability as possible mechanical sensors.

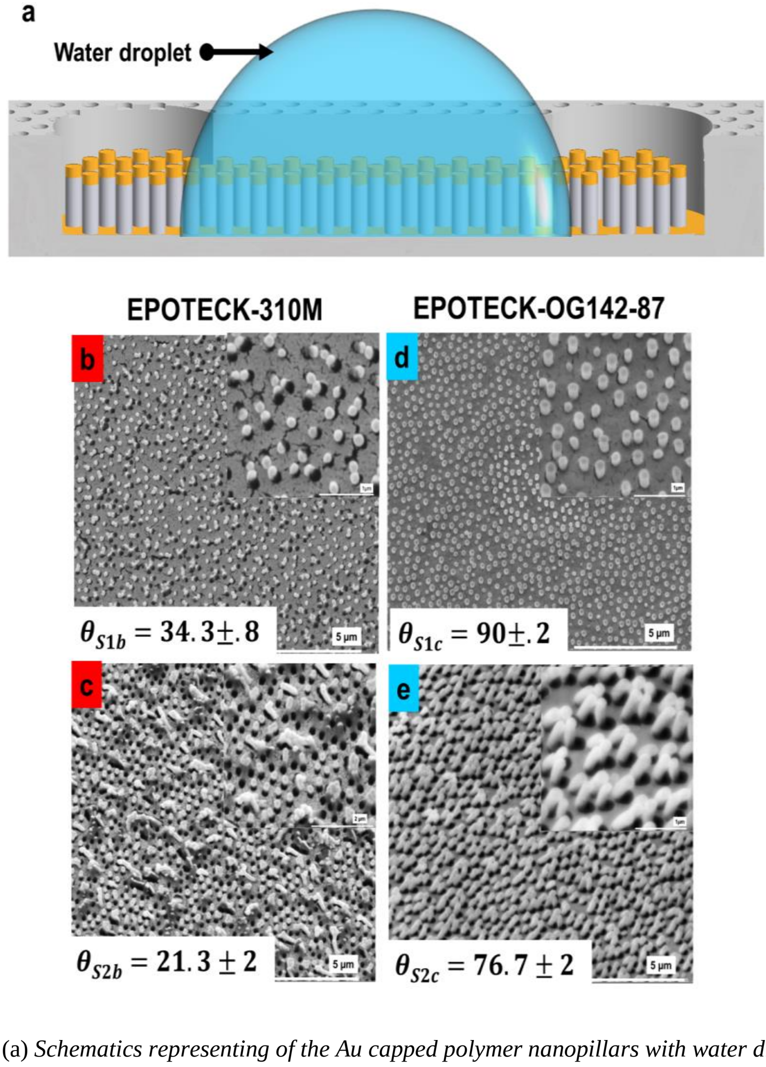

Figure 4.9. (a) *Schematics representing of the Au capped polymer nanopillars with water droplet.* (b-e) *Tilted SEM images (15°) of Au capped 310M nanopillars and OG142-87, after the water droplet test, respectively. The contact angle measurements are also shown in the SEM images, respectively.*

4.6 Conclusions

We have presented simulated scattering, transmission spectra and the electric field distributions at normal incidence of a hexagonal array of Au-polymer nanopillars (with and without perforated gold film). For the simulations of the hexagonal array of gold capped nanopillars with and without gold film, the results show not only that the LSPR spectra are generated in both scattering and transmission, but also that the Au film (nanoholes) create a complex spectrum. According to the simulations, in the real configuration of the sensor, the scattering, and transmission, depending on the wavelength, are dominated by the Au-capped polymer nanopillars and the nanoholes formed in the gold film. This result is not optimal because it means a difficult interpretation of the LSPR shift due to a change in the medium (sensing). As the simulations were based on the ideal geometrical model, the observed deviations in the measured transmission spectra can be attributed to the differences between the model and the real fabricated structures

Taking the previous results into account, we verified that the experimental scattering and transmission spectra shifted by a change in the refractive index of the medium, demonstrating the operation the sensor. In particular, the LSPR in the transmission spectra in air and water are useful for applying the devices for sensing. Also, by using those simulated transmission spectra, the theoretical sensitivity of the 310M (S1b sensor) short nanopillars was ($204.14\, nm/RIU$) approximately calculated. However, the scattering measurements could be inaccurate due to the limitations of our spectrometer and the effect of the electronic noise on the DF microscope.

The sensors have a bulk sensitivity of 270 nm/RIU for 310M (S2b sensor) tall nanopillars, 164 nm/RIU for OG142 (S1c sensor) short nanopillars, and 289 nm/RIU for OG142 (S2c sensor) tall nanopillars, that according to literature, the values of the bulk sensitivity not only match with other plasmonic sensors but also indicate that the sensors could be appropriate for sensing purpose. However, the values do not overcome the sensitivity of the state of art (1000 nm/ RIU)[112]

According to the contact angle, the 310M nanopillars are more flexible and hydrophilic than OG142 nanopillars. Finally, we hypothesized that the 310M (S1b sensor) and OG142 (S1c sensors) short nanopillars could be employed for a preliminary proof a concept of sensing of shear stress and this could be interesting to explore living cells interactions with substrates also. The cells will cause shear forces in the Au capped nanopillars, as reported in [96–100] and according to the experimental results here presented and a LSPR shift if the nanopillars design and material parameters are well chosen.

Chapter 5. Preliminary proof of concept of the sensor

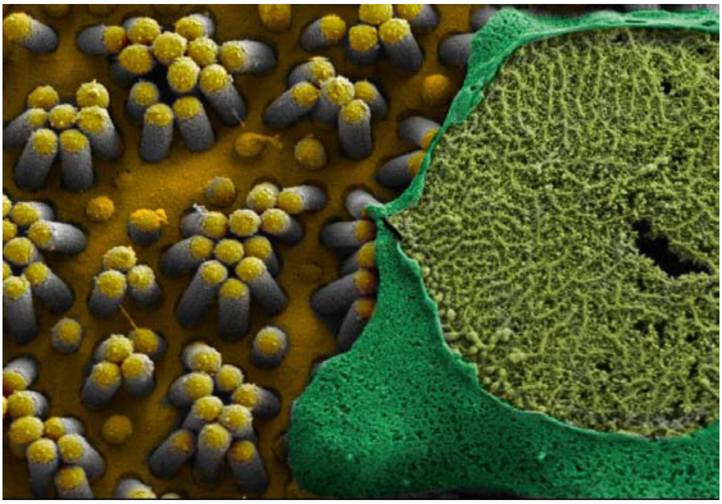

In this chapter, the sensors selection is presented. Also the feasibility of the use of the Au-capped polymer nanopillars for evaluating cell adhesion is shown. A preliminary proof of concept for the LSPR detection of fibroblasts onto the sensors is described. Finally, the general conclusions and future work are presented, focus on the main contribution of this Thesis and the future steps.

5.1 Introduction

As described in the Chapter 4, we hypothesized that the 310M (S1b sensor) and OG142 (S1c sensor) short nanopillars could be employed for a preliminary proof a concept of sensing of shear stress and this could be interesting to explore living cells interactions with substrates also. We believe that the cells could cause shear forces in the Au capped nanopillars, as reported in [96–100], and a LSPR shift if the nanopillars design and material parameters are well chosen. Also, we consider that the different spring constants (*k*) could be interesting parameters to test with living cells. However it is important to notice the complexity and heterogeneity of these interactions which limit the use of these optomechanical sensors in its current form as qualitative rather than quantitative.

In this chapter, we present a preliminary results using the 310M (S1b sensor) and the OG142 (S1c sensor) short nanopillars for cell studies. The first experiments were designed to test the biocompatibility of the sensor materials as the device will be employed as a cell culture substrate. It is necessary to know if living cells are able to make contact with the nanodevices. Also for the first time, we cultured fibroblasts on the sensors, for studying the cellular responses to changes of the nanopillar rigidity in the period of cell adhesion initiation, and their LSPR signature was followed for three hours[100]. The fibroblasts were chosen and donated by University of Barcelona (Department of Biochemistry and Molecular Biomedicine), whose group is specialized in their study.

5.2 Proposed sensors

According to state of the art, the cells not only have been able to excerted forces on microstructures but also on other types devices, those forces ranging from pN to nN. It is important to highlight that the reported forces depend on design detection device (e.g., materials, micro/nanostructures), the methodology of quantification and the cells, and therefore, the forces can vary. Table 5.1 shows some examples of different approaches to detect traction forces using different living cells. With this in mind, we hypothesized that the cells will be able to get close, interact and cause a shear forces in the Au-capped nanopillars, as reported in [96–100] and the Table 5.1, and a LSPR shift if the nanopillars design and material parameters are suitable. However, it is important to point out that the new sensors and the optical detection system can be employed**,** for a preliminary proof a concept of sensing of the aforementioned facts caused by living cells, in their current form as qualitative rather than quantitative.

We analyzed the advantages, limits, optical and mechanical properties of the 310M (S1b sensor) and OG142 (S1c sensor) short nanopillars to study the possibilities that could have to qualitatively detect the cell adhesion. From the point of view of fabrication, they come from the same silicon mold master, and only by changing the Young's modulus of the material the production of polymer structures (<25 samples) with spring constants (*k*) ranging from 10^{-02} N/m to 1 N/m were obtained. The estimated *k* can not only indicate the different mechanical sensitivity to a shear stress but also the soft or rigid mimicked tissue, if required.

Table 5.1 summarizes the characteristics, optical and mechanical properties that we have approximately estimated throughout the thesis. The bulk sensitivity of the 310M (S1b sensor) and OG142 (S1c sensor) short nanopillars were approximately of ≈204 nm/RIU and ≈164 nm/RIU, respectively (See Section 4.4.5). Those values match with the some reported in the literature and have demonstrated to be useful for applications of sensing [30,109,114,137].

The contact angle of the nanopillars were different for 310M short nanopillars (34.3° ±.8, (S1b sensor) and for OG142 short nanopillars (90° ±.2, (S1c sensor)), thus, the capillary forces caused that the Au-capped nanopillars moved the top part of their structure towards their nearest neighbors (See Section 4.5), then we expect something similar happens with the living cells.

Table 5.1 *Optical and mechanical properties of the optomechanical sensors.*

d_{cc}=400 nm	Material	d_{pnp}[a] (nm)	h (nm)	Spring constant (N/m)	(S_B) (nm/RIU)	Contact angle
Short (S1b)	OG142-87 (3.59 GPa)	160±10.8	320±115.1	1.19 E-02 **muscle**	204*	34.3°±.8
Short (S1c)	310M (4.16 MPa)	185.8±18.0	490±131.6	5.35E+00 **bone**	164	90°±.2

Traction forces exerted by cells with devices of the state of the art

Device	Biological system	Force range	cells
Micropillar array	Focal Adhesion	1-100 nN	Rat cardiac fibroblast[97], Bovine pulmonary muscle cells, mouse fibroblasts[96], fibroblast cells [138].
Microplates	Actin networks	10pN	bacteria[139]
	Single cell	Hundreds of nN	Myoblasts (muscle cells) [140]
Atomic force microscope	Actin networks	0.4 -4 nN	lipid vesicles[141]

d_{cc} center to center distance

[a] Botton diameter from SEM images is used for calculation.

*Theoretical bulk sensitivity

5.3 Preliminary proof of concept of the sensor

5.3.1 Materials and Methods

Materials

The fibroblasts are a type of cell that synthesizes the extracellular matrix and the collagen, they are large, flat, elongated (spindle-shaped) cells [142]. The cell line aliquots utilized in this preliminary proof of concept were provided by Dr. Francesc Villarroya specialized in their study, from the *Laboratory of Research in Genetics and Molecular Biology of Mitochondrial Proteins and Associated diseases,* at the University of Barcelona (Spain). The cells immortalized interscapular brown adipose tissue (mice) precursors that maintain the capacity to differentiate into brown adipocytes after induction with a hormonal cocktail[143,144]. It could be expected that a brown adipocyte may reach a diameter of ≈60 microns[145]. Although the elastic modulus of this concrete cell line has not been evaluated, the perivascular adipose tissue has been assessed by Vonavkova and co-workers[146]. They determined an initial elastic modulus of about 0.0170±0.0182 MPa. For our experiments we used $5x10^6$ pBAT cells in suspension, 45 mL pBAT growth media, 45 mL phosphate saline buffer (PBS), and 2.0 mL poly-L-Lysine of (Sigma-Aldrich, United States (0.1mg/mL)) for DMEM (Dulbecco’s modified Eagle's medium) and cell-pleating preparation[143,144].

The poly-L-Lysine is a positively charged amino acid polymer, which can be used to promote cell adhesion to solid substrates. Also, the poly-L-Lysine has amino groups (NH_2) that have an affinity to gold. Although, the amine/gold surface interactions are much weaker than the thiol/gold bond, on nanostructures or nanoparticles the amines form strong electrostatic interactions that have been shown to bind in a manner best described by a weak covalent bond[147,148]. This strategy is widely employed in surface chemistry in gold nanoparticle immobilization[149,150].

Eight samples were employed with different diameter, height, and polymer; including the 310M (S1b sensor) and OG142 (S1c sensor) short nanopillars, (see Table 5.2) to check if the fibroblasts adhere on the nanopillars (experiments done at University of Barcelona). Also, the 310M (d_{pnp}=160 nm, h=320 nm, S1b sensor) and the OG142 (d_{pnp}=185 nm, h=490 nm, S1c sensor) short nanopillars were used to perform cell culture experiments.

As a control, fibroblasts ($30x10^4$ cells/mL) were also seeded onto a commercial culture dish (Corning, Sigma-Aldrich, United States) for three hours. The seeding time of three hours was chosen according to the literature[100] and the experience of our collaborator as good enough to obtain an acceptable percentage of cells adherent to the structured arrays. The attached cells on the polymer nanopillars were also fixed for SEM analysis by using the UAB protocol (See Annex C). For the optical measurements, we employed the set-up described in the Section 4.4.1 and shown in Figs. 5.1a and b. The acquisition times for the spectra were 2 s with 500 spectral accumulations every 30 minutes for 3.0 h.

5.3.2 Cell culture process in the sensor

0.5 mL of poly-L-Lysine (0.1 mg/mL) flowed through the array of nanopillars by the microfluidic channel of the sensor (10µl/min), with an incubation time of 20 minutes. Then, 5 mL of phosphate buffered saline (PBS) passed through the microfluidic channel for 20 min to wash the excess of poly-L-Lysine. Next, 3 mL of growth media (DMEM **(**Dulbecco's Modified Eagle Medium**)**, 10% FBS, 1% antibiotics) was flowed for 10 minutes. Then, the flow was stopped for 20 minutes to discard the possible deformation of polymer nanopillars. After, the fibroblasts were passed through of the sensor. Thus, the flow ratio was stopped for 25 minutes. The outlet of the sensor was closed by a reservoir to avoid loss of the sample as shown in the Figs.5.1a and b. Next, the transmission spectrum acquired every 30 minutes for 3 hours as shown in the Fig.5.1a and b.

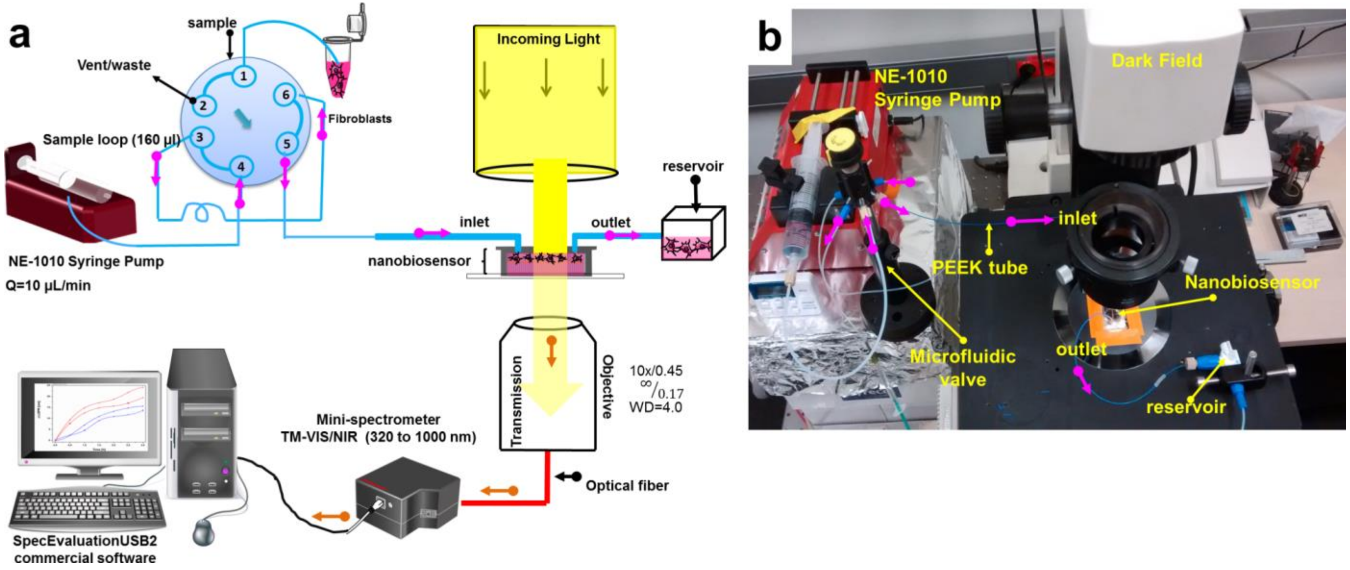

Figure 5.1. (a) *Experimental set-up.* **(b)** *Top-view photograph of set-up used for cell culture protocol for the sensors.*

5.4 Feasibility of Au-capped polymer nanopillars for cell adhesion

First of all, it is necessary to check that cells can adhere on the flexible nanopillars as they are different to the typical substrate used in cellular culture (plastic petri dish). For that a cell culture was performed for 3 hours[100] on arrays of gold capped polymer nanopillars. Before the experiments, the sensors were sterilized with UV light for 10 minutes, and then they were immersed in 2 mL of poly-L-Lysine (0.1 mg/mL) to functionalize the nanopillars, with an incubation time of 20 minutes. Then, the poly-L-Lysine was aspirated by vacuum (Figs.5.2a,b). The sensors were immersed in PBS (incubation time, 20 min) and aspirated by vacuum. We confirmed the density of cells using an automated cell counter (Fig.5.2d). The cells were seeded ($30x10^4$ cells/mL) on the nanopillars and the commercial culture dish (Fig.5.2e) and let growing for three hours in the culture medium at 37˚C with 7 % CO_2 in an incubator, as shown in Fig.5.2f. As the incubator cannot be open for very long time, only the OG142 (S1c sensor) short nanopillars and the commercial culture dish were observed by microscopy (20x objective) every 30 minutes (Fig.5.2g). Finally, after the three hours of incubation, the cells seeded on the sensors were fixed for SEM analysis (Fig.5.2h)

Table 5.2. *Characteristics of the sensors and the culture dish to seed fibroblasts* (*$30x10^4$ cells/mL*)

Sensor	EPOTECK 310M (4.16 MPa)	EPOTECK OG142-87 (3.59 GPa)		Commercial culture dish
	d_{cc}=400nm	d_{cc}=400nm		
M1	$h\approx800$nm, d_{pnp}=180 nm	M4	$h\approx1.3$ µm, d_{pnp}=180 nm	1 dish
M2	$h\approx470$nm, d_{pnp}=160 nm	M5	$h\approx750$nm, d_{pnp}=180 nm	-
M3	$h\approx400$ nm, d_{pnp}=160 nm	M6	$h\approx500$nm, d_{pnp}=180 nm	-
Short (S1b)	$h\approx320$nm, d_{pnp}=160 nm	Short (S1c)	$h\approx490$nm, d_{pnp}=185 nm	-

dcc, distance center to center of the nanopillars

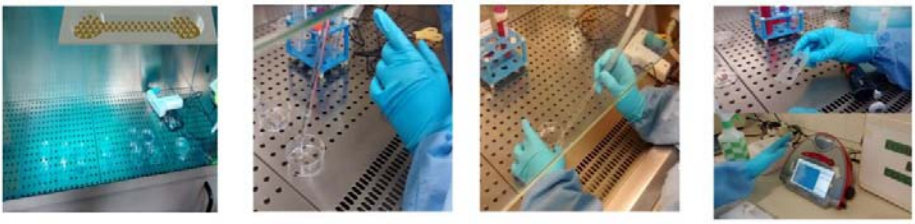

a. Sterilization UV (10 min) b. poly-L-lisina (20 min) c. Remove poly-L-lisina d. Cell counter

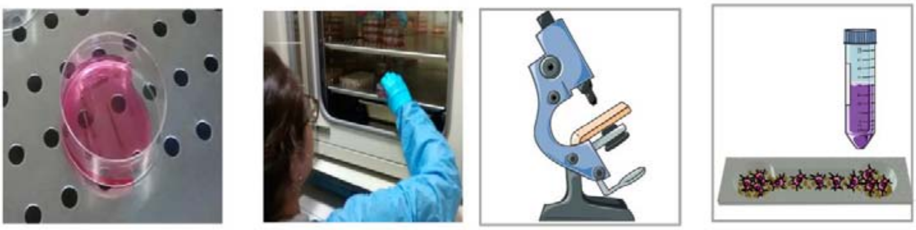

e. Cell culture on a nanobiosenor f. Incubator g. Microscopy every 30 min for 3 h h. Solution to fix the cells for SEM images

Figure 5.2. *Cell culture on arrays of gold capped polymer nanopillars within the microfluidic channel.* **(a-g)** *Cell culture protocol realized in the laboratory of the Univ. of Barcelona*.**(h)** *Solution to fix the cells on the polymer nanopillars for SEM analysis.*

5.4.1 Results and discussion

In Figs. 5.3a and b, we can observe fibroblasts attached on 310M nanopillars of the M1sample (h ≈800 nm, d_{pnp}≈180 nm) and also of the M2 sample (h ≈470 nm, d_{pnp}≈160 nm), respectively. We can observe that the fibroblasts spread on soft nanopillars with their filopodia projections, whose morphology and behavior on the nanopillars are similar with other works reported in the bibliography[97,99,100,138]. The filopodia lengths are ≈9.93 µm and ≈6.74 µm, respectively. We can also notice that the Au-capped polymer nanopillar moved by capillary forces during the liquid drying step of the protocol for fixing attached cells.

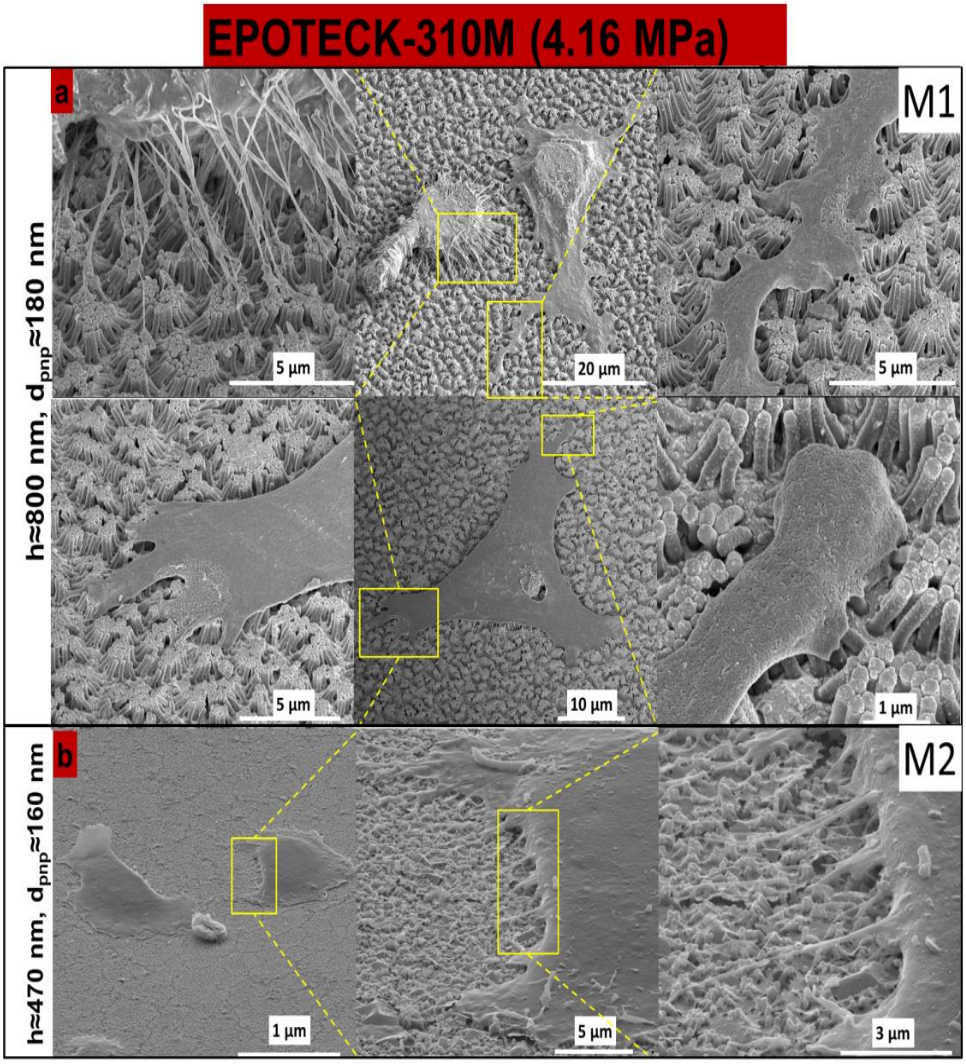

Figure 5.3. *SEM images showing the influence of nanopillars on the process of cell adhesion after 3 hours.* **(a)** *and* **(b)** *fibroblasts spread on 310M nanopillars substrates, h≈800 nm,* d_{pnp}*≈180 nm, and h≈470 nm,* d_{pnp}*≈160 nm, respectively.*

Fig. 5.4a exhibits the adherent cells could form dynamic extensions during the process of cellular adhesion and spreading, in the proposed time by the biologist specialist. It is also clear the cell-nanopillar interactions on 310M nanopillars of sample M3 (h ≈400 nm, d_{pnp}≈160 nm). The SEM images display cells with filopodial extensions of ≈12.49 μm that are similar with the literature[96,151]. The 310M (S1b sensor) short nanopillars used for this cell culture was experimentally contaminated and damaged during the cell culture. As a result, the gold film was lifted as shown in the Fig.5.4b.

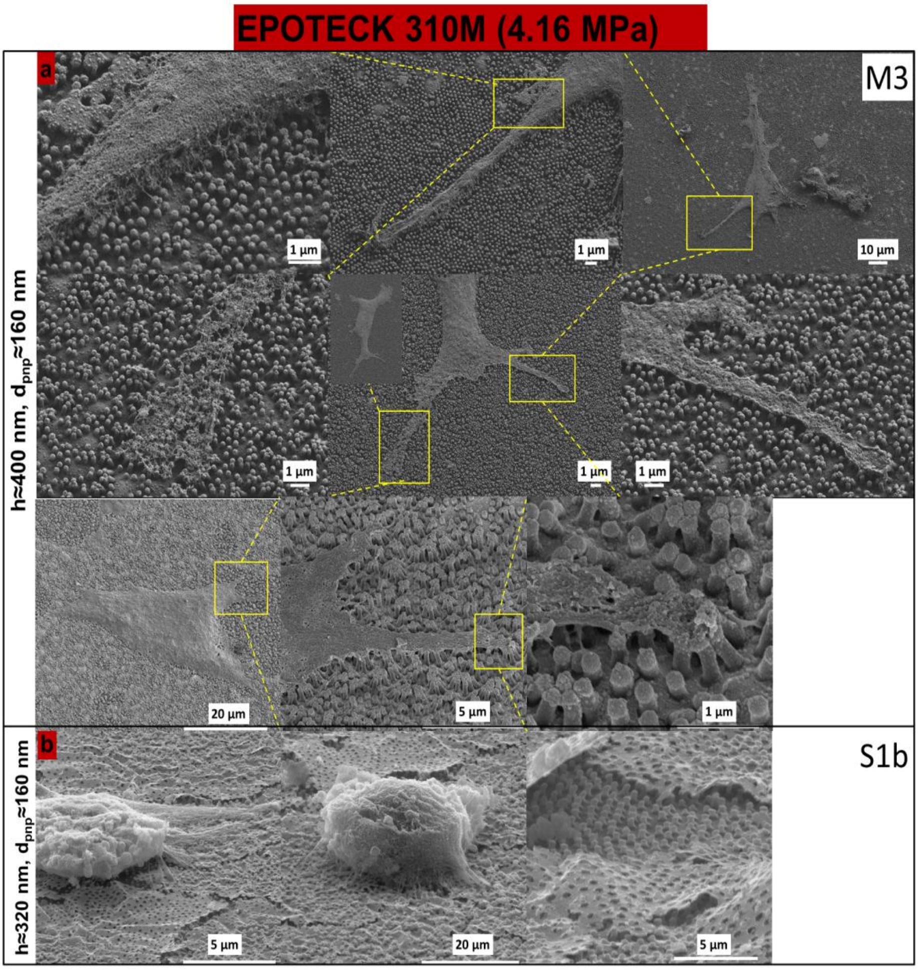

Figure 5.4. *SEM images showing the influence of nanopillars on the cell adhesion process after 3 hours.* **(a)** *and* **(b)** *fibroblasts spread on soft 310M nanopillars substrates, h≈400 nm, d_{pnp}≈160 nm, and h≈320 nm, d_{pnp}≈160 nm, respectively.*

The fibroblasts cultured on OG142 nanopillars of the M4 and M5 samples are shown in Figs.5.5a and b, respectively. We can see the sites of cell attachment to the rigid nanopillars forming their adhesions. Thereby, the cells could perceive the nanoscale topography through lateral scanning and protrusions events verifying to that reported in the literature[96,99,138,151]. The filopodia length of fibroblasts on OG142 nanopillars of the M4 and M5 samples are ≈20.81 µm and ≈24.85 µm, respectively.

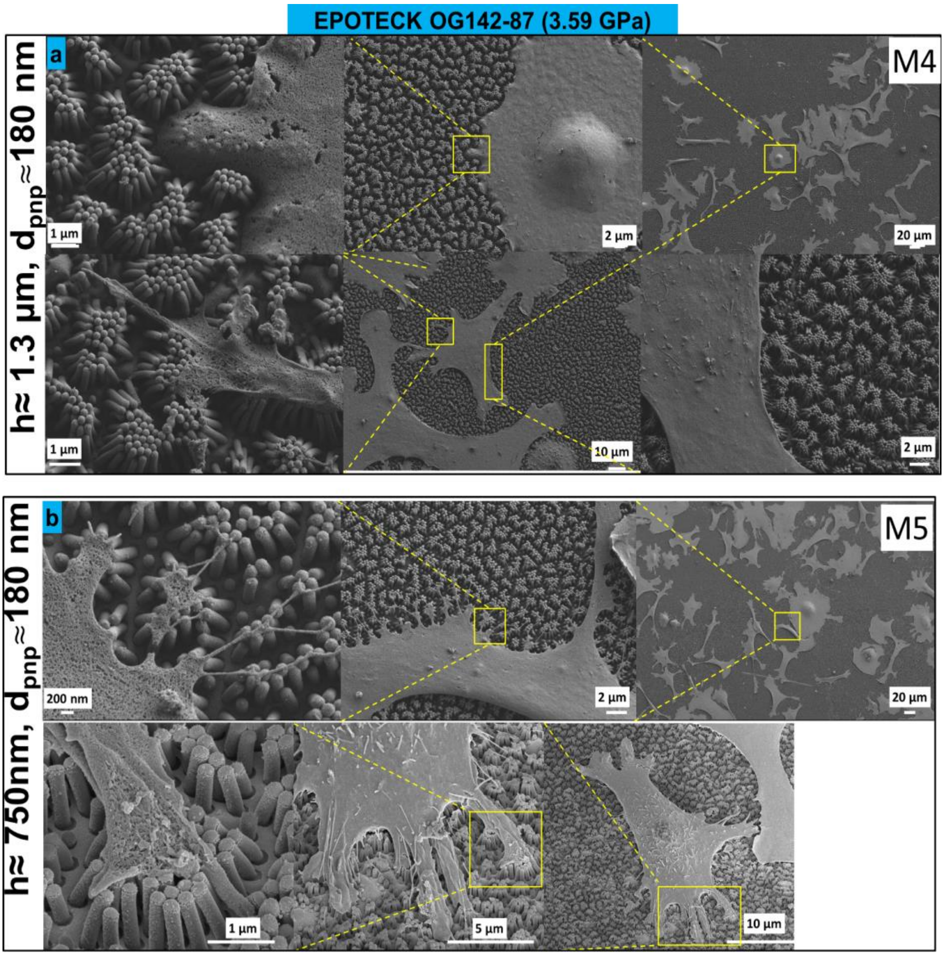

Figure 5.5. *Cell-nanopillar interactions and focal adhesion formations* **(a)** *and* **(b)** *adherent cells form filopodial extensions during the process of cellular adhesion and spreading, on OG142 nanopillars,* $h \approx 1.3\ \mu m$*,* $d_{pnp} \approx 180$ *nm, and* $h \approx 750$ *nm,* $d_{pnp} \approx 180$ *nm, respectively.*

In the SEM images of the OG142 nanopillars of the M6 and S1c sensors (Fig.5.6), the effect of the capillary forces during the liquid drying step was reduced by the mechanical stability due to the aspect-ratio of the rigid nanopillars. Thereby, the cell-nanopillar interactions on rigid nanopillars were easier to see. Moreover, we could notice that the fibroblasts spread on rigid nanopillars with their filopodia projections[99,100,151]. According to SEM images, the filopodia lengths are ≈32.23 µm and ≈33.3 µm, respectively. Therefore, these SEM images of fibroblasts were experimental indicators that cells were able to pull on both soft and rigid polymer nanopillars and, thereby, cause a shear stress. It is important to point out that the drying step of protocol for fixing cells does not happen in the LSPR detection of the fibroblasts on the sensors, in other words, the cells always are in DMEM liquid, and then, the capillary effect of the polymer nanopillars never happens.

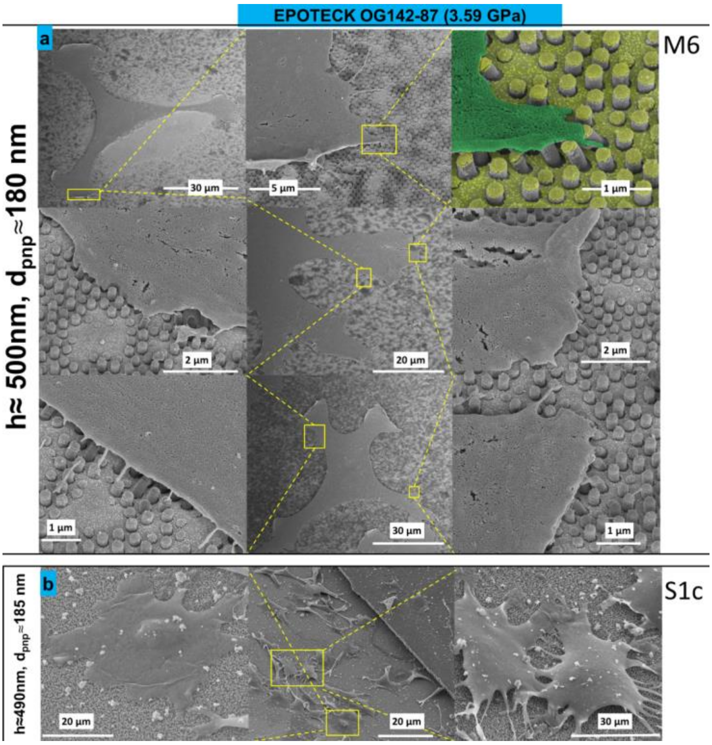

Figure 5.6. *Cell-nanopillar interactions and focal adhesion formations* **(a)** *and* **(b)** *adherent cells form filopodial extensions during the process of cellular adhesion and spreading, on rigid nanopillars, h≈500 nm,* d_{pnp}*≈180 nm, and h≈490 nm,* d_{pnp}*≈185 nm, respectively.*

5.5 LSPR detection of fibroblasts on the sensors

Once it has been proven that the cells could make contact with the 310M and OG142 nanopillars for three hours, we performed the measurement of the transmission spectra when the fibroblasts were on the different sensors to research the possible effect of the spring constants could have on cellular adhesion for 3.0 h[100]. Two new 310M (d_{pnp}=160 nm, h=320 nm, S1b sensor) and OG142 (d_{pnp}=185 nm, h=490 nm, S1c sensor) short nanopillars were used to perform cell culture experiments with an analytical spring constant of $1.19 \cdot 10^{-02}$ N/m and 5.35 N/m, respectively. By following the cell culture process (Section 5.3.3) onto the sensors 30×10^{4}cells/mL were passed for 25 minutes through the microchannel to be seeded. The outlet of the sensor was closed by a reservoir to avoid loss of the sample as shown in the Figs.5.1a and b. The cells were observed by DF microscopy to check their survival on the zone (100 µm), thereby LSPR transmission spectra were obtained every 30 minutes for 3 hours. A schematic and photo of the experimental setup, containing all the major components, can be observed in Fig. 5.1.

5.5.1 Results and discussion

Fig. 5.7a and b show the results of the LSPR responses due to cell culture on 310M (S1b sensor) and OG142 (S1c sensor) short nanopillars, respectively. The value of LSPR, at 0.0 h, corresponds to the DMEM solution (reference), then we hypothesized that the polymer nanopillars were in the equilibrium position. Also, we can notice that the λLSPR is red-shifted as time increases. We hypothesize that those significant LSPR responses could have been caused by the local changes of the refractive index caused by the cell-nanopillars interactions, according to the previous SEM analysis of the cells on 310M and OG142 nanopillars (Section 5.4.1). To examine the impact of the spring constant of the different sensors (310M and OG142) in the period of three hours, the $\Delta\lambda_{LSPR}$ was approximately calculated from the spectral resonance shift and the initial position of the LSPR at 0 h, as shown in Fig. 5.7c.

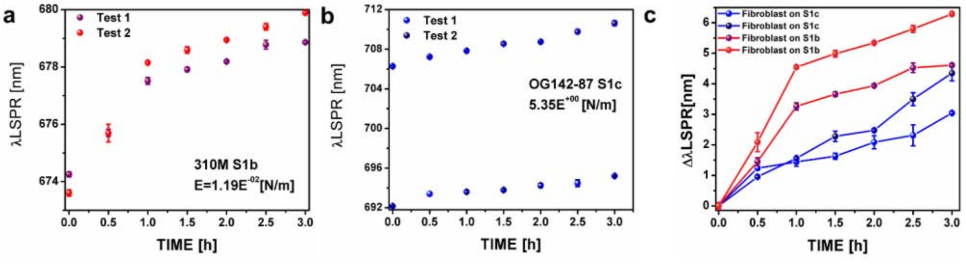

Figure 5.7. (a-b) *Experimental LSPR transmission spectra due to cells adhesion from 0 to 3 h on the 310M (S1b sensor) and OG142 (S1c sensors) short nanopillars, respectively.* **(c)** ΔλLSPR *calculated from the induced spectral resonance shift with respect to the initial position of the LSPR at 0 h for soft and rigid sensors.*

Microscope images comparing the cells seeded on OG142 (S1c sensor) short nanopillars with the standard culture dish are shown in Figs. 5.8, an observational method widely used in biological experimentation as suggested by the biology expert collaborators and widely reported in literature[152]. In Fig. 5.8a and b, we could notice how the fibroblasts in the Au-capped nanopillars looked similar to those in culture dish at 0 h. In both substrates, spherical cells were floating in the growth media however there were cells began to adhere on both substrates.

At 0.5 h, we could hypothesize in Fig.5.8 c and d (shown in dashed circle) the initial cell tethering and filopodia exploration which started faster on OG142 nanopillars than in the culture dish. This cell behavior coincides with other reported experiments in the bibliography[7,97].We checked with the SEM pictures that this occur in the sensors and, thereby, the red shift of LSPR at 0.5 h (see Fig. 5.7c) could be caused by the changes in the refractive index induced by the cells adhered on the array of nanopillars.

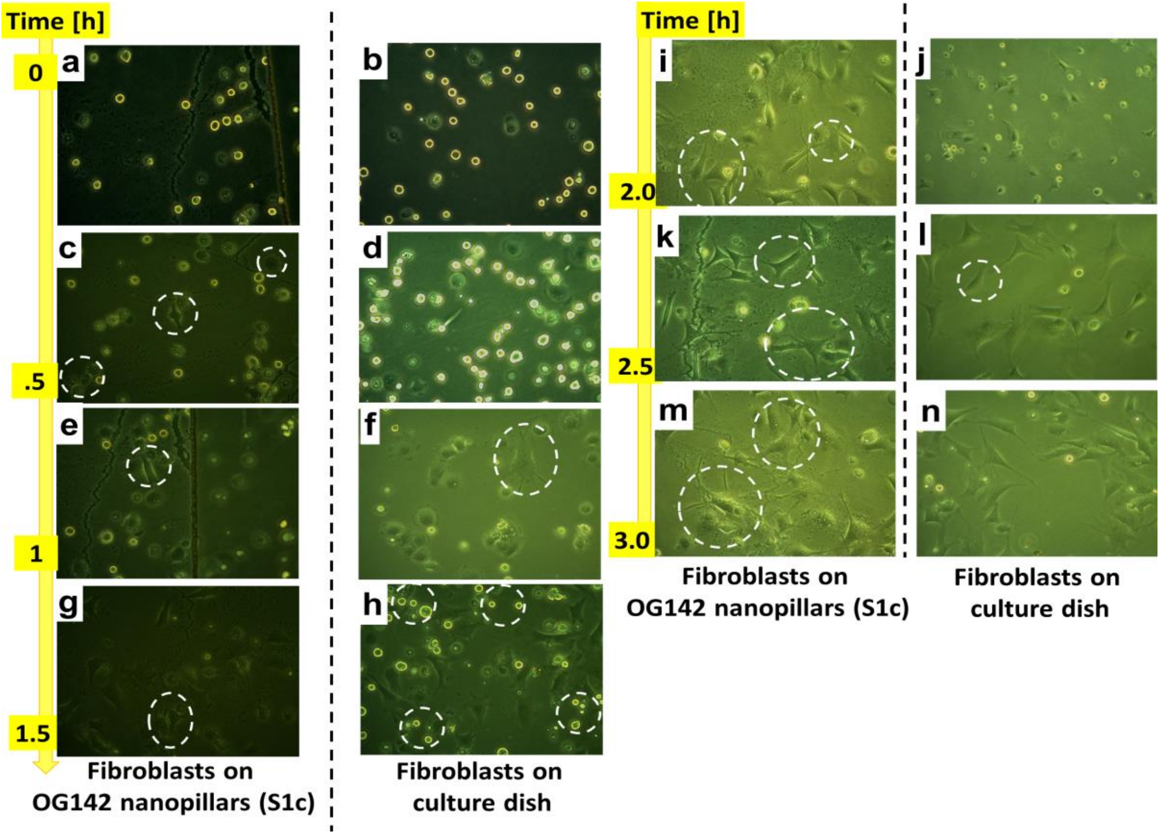

Figure 5.8.(a-b) *Experimental LSPR transmission spectra due to cells adhesion from 0 to 3 h on the S1b and S1c sensors, respectively.* **(c)** $\Delta\lambda$LSPR *calculated from the induced spectral resonance shift with respect to the initial position of the LSPR at 0 h for soft and rigid sensors.* **(d-q)** *Comparison of cell adhesion on OG142-87 nanopillars with a standard culture dish. Photos* (20x) *of fibroblasts cultured on the Au capped OG142-87 nanopillars within microchannel and on culture dish every 30 minutes for 3.0 h.*

The LSPR responses of the 310M (S1b sensor) and OG142 (S1c sensor) short nanopillars indicate a red shift at 1.0 h by ≈3.5 nm and by ≈1.4 nm, respectively. In that time, the microscope images (Figs.5.8 e and f.) showed that the number of attached fibroblasts on the nanopillars increased similarly to those on the culture dish at 1.0 h, also their morphologies match with other studies[7,153]. We hypothesized that the changes could have possibly been originated by the spread of cells on the array of nanopillars, as in Figs 5.8 e and f shown, and thereby, to provoke the additional LSPR shift.

The LSPR responses of sensors at 1.5 h (Fig.5.7c) showed a red shift by ≈4 nm and by ≈2 nm, respectively. Therefore, we hypothesize that the greatest contribution of LSPR changes could be caused by the living fibroblasts. As occurs at that time, in the experimental images fibroblasts (see Figs.5.8g and h). They were adhered on the nanopillars, whereas some spherical fibroblasts (shown in dashed circle) were still floating in the medium of the culture dish.

The photos from 2.0 h to 3.0 h (Figs. 5.8i-n) clearly suggest that most of the fibroblasts could not only adhere but also respond to the nanoscale topography, through cytoskeletal projections (filopodia) to explore the nanofabricated substrate, as SEM pictures shown (Section 5.4.1). Also, those results are similar with reported experiments in the literature[7,97,138,153]. We hypothesized that fibroblast could behave as the experimental SEM pictures and, thereby, caused those LSPR responses, as Fig.5.7c shown.

Finally, the previous results suggest that the fibroblasts could adhere to the flexible nanopillars as shown in photos and SEM pictures, causing displacements in the Au-capped nanopillars. Also, those pictures confirm the biocompatibility of the 310M and OG142-87 materials in the period of three hours. On other hand, we hypothesized that the significant LSPR changes detected by the 310M and OG142 sensors, with a slightly contribution of the culture medium, could be provoked by the fibroblasts adhesion and subsequently local increase of the refractive index in the vicinity of the plasmonic nanodisks. Unfortunately, the current optical system does not have the capacity to distinguish between the LSPR response due to shear stress in the nanopillars and local changes in the refractive index.

5.6 Conclusions

We have employed the 310M (S1b sensor) and OG142 (S1c sensor) short nanopillars as they come from the same silicon mold master, and only by changing the Young's modulus of the material, the production of polymer structures with spring constants (k) ranging from 10^{-02} N/m to 1N/m were obtained. The estimated *k* can not only indicate the different mechanical sensitivity to a shear stress but also the capacity to mimic soft or rigid tissue.

The previous results suggest that the fibroblasts could not only adhere but also respond to the nanoscale topography of the sensors, through cytoskeletal projections (filopodia). Also they could exert shear stress at the tip of the flexible nanopillars as shown in photos and SEM pictures, causing displacements in the Au-capped nanopillars. Those pictures confirm the biocompatibility of the 310M and OG142-87 materials for three hours. On other hand, we hypothesized that the significant LSPR changes detected by the sensors, with a slightly contribution of the culture medium, could have been provoked by refractive index increased caused by the fibroblasts adhesion, during the three hours. Unfortunately, the current optical system does not have the capacity to distinguish between the LSPR response due to a shear stress in nanopillars and change in the refractive index of medium.

General Conclusions

We have designed and implemented reproducible fabrication protocols to create a new prototype of a plasmo-mechanical sensor compatible with microfluidic technologies. The principal conclusions of this thesis that can be drawn from the experimental studies are the following:

*We described a reproducible and low-cost fabrication protocol of ordered arrays of silicon nanopillars (SiNPs) with integrated polymer microfluidics. With our fabrication strategy, the area, hexagonal arrangement, diameter, and height of the SiNPs within the microchannel are well controlled. In this process, it was shown that the diameter of the PS spheres (300 nm and 400 nm of diameter) was reduced by RIE treatment and these results were used to control the diameter of the SiNPs. Our investigation confirmed that the height of SiNPs increases as the etching time becomes longer. Moreover, the simple cleaning of the microchannels by UV/Ozone evidently affects the etching rate. Through our results, we demonstrate that the combination of reduced diameter (dr), and periodicity (dcc) of the catalytic gold mesh plays a key role in order to control the etching rate. We exploited the inert properties of the SU-8 polymer (e.g. resistant to HF/H_2O_2 solution) to outline a microfluidic channel. By using our protocol, we avoid the need to align the nanopillar structures with microfluidic devices, reducing the chances of damaging their topography and integrity. Finally, the integrated platform was used as a master mold for replica molding technique, for mass production of the plasmo-mechanical sensor (<25 samples).

*We presented an efficient fabrication of flexible sensors with modulated rigidity formed by polymer nanopillars capped with gold nanodisks integrated into a microfluidic channel using a replica molding technique. The controlled process to produce PDMS molds of nanoholes from the silicon master was described. Different polymers with an increasing Young´s modulus were used to understand and investigate the replica molding limitations of polymer nanopillars when the gold nanodisks were placed on them. The results confirmed that the molding material and the aspect ratio play a significant role in the success of the replica molding.

We showed that the use of polymers EPOTECK-OG142-87 and 310M combined with our fabrication protocol were able to replicate the SiNPs integrated into the SU-8 channel, with an aspect ratio from 1.6 to 7.37, whose estimated spring constants (*k*) can not only indicate the different mechanical sensitivity to a shear stress, but also mimic soft or rigid tissues. Experiments under different flow rates were carried out to test the pressure and duration of the permanent bonding of the flexible sensors. The permanent bonding was stable from 5 to 50 µl/min, breaking at 90 µl/min for both materials.

*The results of the simulation of the transmittance spectrum were in good agreement with the experimental one obtained from the corresponding peak and dip positions of the array of Au-capped polymer nanopillars with a gold film. This was a suitable approach to the evaluation of the LSPR spectra for characterization of the sensors. Furthermore, the sensors presented adequate bulk sensitivity ≈204 nm/RIU for 310M (S1b sensor), ≈270 nm/RIU for 310M (S2b sensor), ≈164 nm/RIU for OG142 (S1c sensor), and ≈289 nm/RIU for OG142 (S2c sensor).

*The results suggest that the fibroblasts could not only adhere but also respond to the nanoscale topography of the sensors, through cytoskeletal projections (filopodia). Also they could exert shear stress at the tip of the flexible nanopillars as shown in photos and SEM pictures, causing displacements in the Au-capped nanopillars. Those pictures confirm the biocompatibility of the 310M and OG142-87 materials for three hours. On other hand, we hypothesized that the significant LSPR changes detected by the 310M (S1b sensor) and OG142 (S1c sensor) short nanopillars, with a slightly contribution of the culture medium, could have been provoked by the fibroblasts adhesion due to the higher refractive index of cells during the cell culture of three hours.

Currently, the flexible optomechanical sensors have achieved a qualitative degree of advancement to study cell adhesion, however there is still additional work to be done to distinguish, locate and quantify the cellular traction forces. The optomechanical sensors are ready for a second phase of development aimed at overcoming their optical and mechanical limitations.

6.1 Future perspectives

Short term future work

In this Thesis we have developed the first prototypes of flexible optomechanical sensors for the study of living cells using low-cost and large-scale nanofabrication techniques. Future perspectives may be directed towards the improvement of the complete prototype of the sensor by using the study developed in this work.

*The design of the microfluidics channels has to be improved. The aspect ratio should be reduced by the modification of the size of the canal. Also, the design could be adapted according to any particular necessity to study the cells. Due to the well-controlled protocol to create the silicon nanopillars, the new model of the channels will not affect the quality of the structures.

*The configuration of the hexagonal array of Au-capped polymer nanopillars with the gold film on their base must be improved. The gold film must be removed by using as a guide the experiments proposed in this work. Then, the LSPR spectra measurements could be enhanced and as a consecuence also the sensitivity of the sensor will improve. Due to the well-controlled protocol to create the bonding of the microfluidics system, the new configuration of the sensor will not affect the quality of operation of the microfluidic channel.

*Optical and mechanical simulations could be performed in Comsol Multiphysics to study a real model of the sensor in order to propose a relation to the quantification of cellular traction forces. Also, florescent beads embedded into the polymer nanopillars could be used as marker to follow and check their deformation and to perform an image analysis of the cells.

Long term future work

*We considered necessary to replace the Darkfield microscope for an optical set-up to move the system to a biology specialized laboratory to perform the experiments of the cells under suitable conditions (e.g., temperature and CO_2). The optical set-up should be able to distinguish the LSPR spectra of vertical and bent nanopillars as well as the dielectric medium. Also, it should provide the number of the cells and the position of the traction forces.

The optical detection system could be based on the combination of the mechanical flexibility of the polymer nanopillars and the optical properties of the plasmonic gold nanodisks, to detect and identify the traction forces of the living cells. As described in the introduction, by analyzing the near-field interactions of the plasmonic nanodisks supported on top of the flexible nanopillars, the detection of the traction forces of the living cells could be possible, and then, by using the polarization of the light (parallel and perpendicular) the LSPR changes due to bent nanopillars and variations in the external dielectric medium could be distinguished.

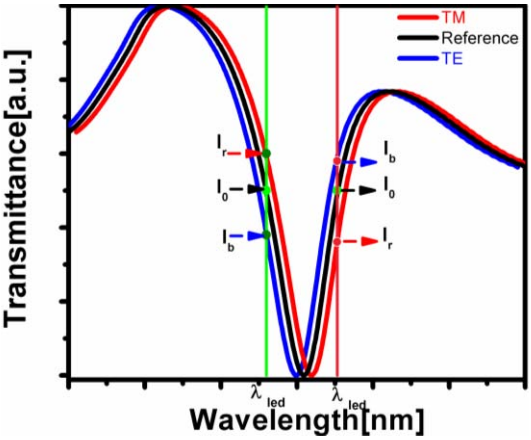

Fig. 6.1 *Representative LSPR spectra due to intensity changes by using both polarizations of the light.*

The proposed optical system should allow the following functions. Once we know the LSPR spectrum generated by Au nanodisks, we propose to use a LED with emission wavelength where the slope of the spectrum curve is greater (green and pink line), as shown in Fig. 6.1. The wavelength (λ_{led}) will provide a reference point with an initial intensity of the spectrum (I_0), as shown in Fig. 6.1. The optical system will take images of the area by using parallel (transversal magnetic-TM) and perpendicular (transversal electric-TE) light polarizations. As a result, we could observe intensity changes produced in each pixel of the images due to the spectral shifts towards red or towards blue. If the intensity of the reference point increases (green line) it will be attributed to a LSPR red-shift (I_r).

In contrast, if the intensity of the reference point decreases, it will be attributed to a LSPR blue-shift (I_b), see Fig. 6.1.Therefore, the spectral changes could be observed by the optical system as changes of intensities with time. Note that the above reasoning should be applied accordingly to the slope of the selected curve (pink line). Then, the images will show maps of intensity of the cellular traction forces and of the dielectric medium, and therefore, the study of the cellular adhesion with the time could be analyzed.

*This methodology of the fabrication allows the creation of a new design of sensor that contains soft and rigid nanopillars in the same microfluidic channel. Thereby, the study of the influence of the rigidity of the substrate on the traction forces could be performed at the same time. Also, the development of a cell culture substrate of rigid nanopillars could make possible to study also the cell movement and other cell functions. By using the LSPR of the Au nanodisks onto the nanopillars, the sensors could be employed to study for example, the cell signaling (*e.g*, protein secretions from the cells).

Finally, this Ph.D. Thesis represents a significant contribution to the progress in the development of new technologies to analysis cell function. This Thesis is a first step to getting sophisticated sensors whose capabilities can facilitate fundamental investigations in the Cells Biology Field.

Annex A

A. Approximate values the of spring constant of different tissues

The calculation of the required spring constant (k_{tissue}) of the polymer nanopillars to mimic the reported elastic modulus of different tissues[133] is extracted from reference[98]. In Table A, we see the different tissues with their elastic modulus and spring constants, represented in N/m. On other hand, the necessary nanopillars aspect ratio is extract from $k = \left(\frac{3}{4}\pi E\frac{r^4}{L^3}\right)$, where r is the nanopillar radius, by using the previous k_{tissue}, the aspect ratio of the nanopillars can be estimated and chosen to minimize the nanofabrication risks[69], as also shown in Table A.

Table A. Elastic Modulus of different tissues and their k_{tissue} in N/m. Approximated values of aspect ratio of nanopillars required to match the stiffness of the tissues.

Tissue type	Elastic Modulus of the tissues[133]	Spring Constant (k)[98] of the tissues	Aspect ratio of Nanopillars*
Brain	100Pa	$10^{-4}\ \frac{N}{m}$	≈5.4*
Liver	1kPa	$10^{-3}\ \frac{N}{m}$	≈2.2*
Muscle	10kPa	$10^{-2}\ \frac{N}{m}$	≈1.16*
Cartilage	100kPa	$10^{-1}\ \frac{N}{m}$	≈2.5**
bone	1MPa	$10\ \frac{N}{m}$	≈1.16**

Aspect ratio (height/diameter, L/D) of nanopillars with proposed diameter D=100 nm and a Young modulus (1MPa, 100MPa**) required to match the stiffness of different tissues.

Annex B

B. Script to calculate the high-degree polynomial to fit the experimental spectra

```
%Loading of the wavelength and spectrum data.
A1=load('Ex1.txt');
%Plotting the original data.
x= A1(:,1);
y= A1(:,2);
plot(x,y);
hold on
title('Original Spectrum Data')
xlabel('[nm]')
ylabel('[transmission %]')
xlim([xmin,xmax]);
ylim([0.46,0.5]);
%Creation of the polinomial of grade n =10 with a range
%from 450 to 800 nm.
lcolors= ['g','c','y','k','b','r','c','y','k','r'];
icolor =  1;
% Data loading and range to test
xmin=600;
xmax=750;
for n=5:10;
  m=n-1;
  pp=polyfit(x,y,m);
  %Derivate the interpolated polynomial to calculate maximums and
  %minimums by finding its roots.
  dp=polyder(pp);
  rp=roots(dp);
  %We take away the imaginary roots.
  r = rp(imag(rp)==0);
  %We limit the roots to the known range of our experiments (600 nm    to 750 nm)
  r=r(intersect(find(r>xmin),find(r<xmax)));
  % We find the corresponding values for the roots.
  yr=polyval(pp,r);
  % We find the global minimum value.
  [ymin,imin] = min(yr);
  wmin = r(imin);
  Ax  (n)= wmin;
  Ay(n)= ymin;
  % Plot the Interpolated Polinomial
  x2=450:1:800;
  y2=polyval(pp,x2);
  pg=plot(x2,y2,lcolors(icolor),'LineWidth',2);
  % Mark the minimum plot on the polynomial.
  plot(wmin,ymin,'ro','LineWidth',2);
  xlim([xmin,xmax]);
  ylim([0.46,0.5]);
  title('Fitted Spectrum Data')
  xlabel('[nm]')
  ylabel('[transmission %]')
  lb{icolor}=sprintf('n = %d, wmin = %.3f nm, ymin = %.3f',n,wmin,ymin);
  legend(pg,lb{icolor});
  icolor = icolor + 1;
  %sprintf('n = %d, wmin = %.3f nm, ymin = %.3f',n,wmin,ymin)
  %legend(sprintf('n = %d, wmin = %.3f nm, ymin = %.3f',n,wmin,ymin));
  pause
end

for i=1:icolor-1
  disp(lb{i})
end
```

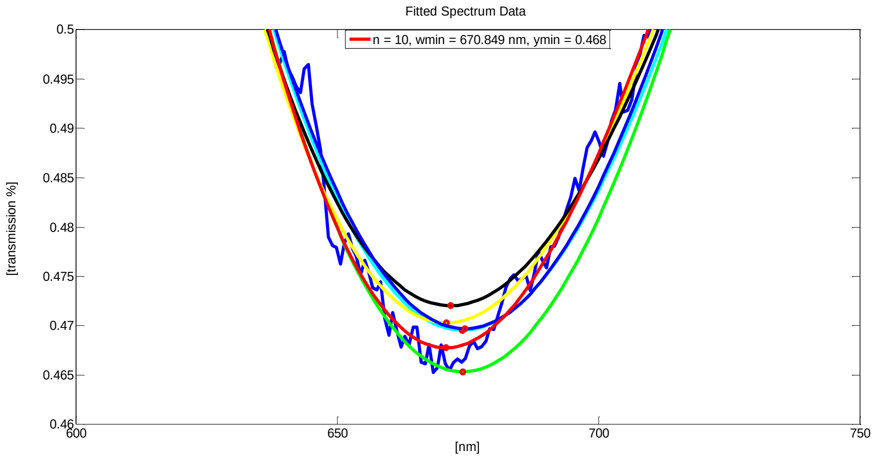

Fig. 1 *Example of the effect using different high-degree polynomials on an experimental spectrum*

The Fig. 1 shows the results when the different degree of polynomials (N=5 to 20) is used in a same experimental spectrum. Also, it can be seen the minimum values with their ***ymin.*** Green curve, n = 5, wmin = 674.018 nm, ymin = 0.465.Cyan curve, n = 6, wmin = 673.910 nm, ymin = 0.470. Yellow curve, n = 7, wmin = 670.921 nm, ymin = 0.470. **Black** curve, n = 8, wmin = 671.708 nm, ymin = 0.472. Blue curve, n = 9, wmin = 674.461 nm, ymin = 0.470. Red curve, n = 10, wmin = 670.849 nm, ymin = 0.468. According to results a high-degree polynomial adjusts well to the spectrum, then we teste a degree of 20. Fig. 2 shows the fitted and the original spectra.

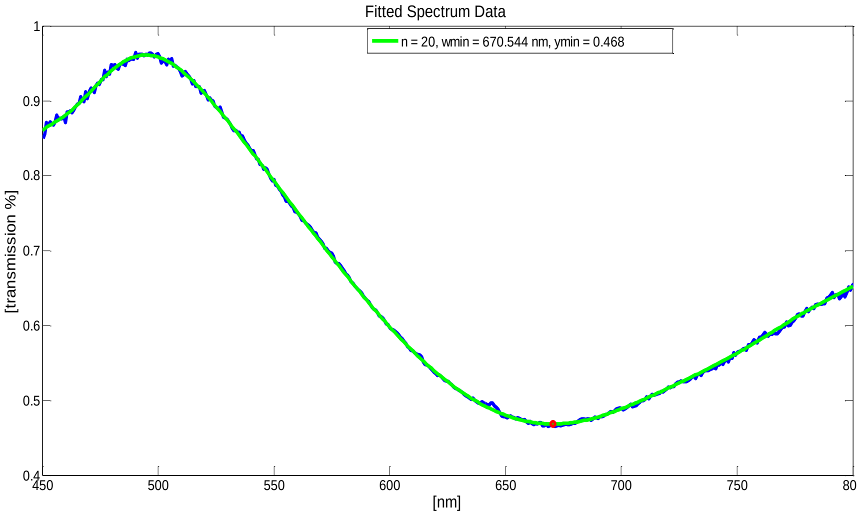

Fig.2 *Result of fitted spectrum using a polynomial of 20 degree.*

Annex C

C. Protocol for fixing Attached Cells in Paraformaldehyde

Ed Harlow and David Lane

This protocol was adapted from "Staining Cells," Chapter 5, in *Using Antibodies* by Ed Harlow and David Lane. Cold Spring Harbor Laboratory Press, Cold Spring Harbor, NY, USA, 1999.
Cite as: Cold Spring Harb. Protoc.; 2006; doi:10.1101/pdb.prot4294

Treating cells with paraformaldehyde leads to the establishment of chemical cross-links between free amino groups. When the cross-links join different molecules, a latticework of interactions occurs that holds the overall architecture of the cell together. Commercial formaldehyde solutions are not recommended, because they lack the advantages of using a variable-length polymer, and the cells will simultaneously be fixed with the alcohol (usually methanol) these solutions contain. For fixing attached cells in organic solvents, see Fixing Attached Cells in Organic Solvents. For fixing suspension cells with paraformaldehyde, see Fixing Suspension Cells with Paraformaldehyde.

MATERIALS

Reagents

Cells that have been attached to coverslips, slides, or tissue-culture dishes
Paraformaldehyde in PBS (4%, prepared fresh)
PBS
0.2% Triton X-100or NP-40 in PBS

Equipment

Racks or staining jars (Optional, see Step 2)

METHOD

1. Prepare a fresh solution of 4% paraformaldehyde in PBS.
2. Rinse the coverslip, slide, or tissue-culture dish once with PBS: For individual slides or coverslips, hold them with forceps and dip in a beaker of PBS. For batches of slides or coverslips, use commercially available racks. For plates, simply pour off the media and flood the plate with PBS.
3. Drain well, but do not allow the specimen to dry.
4. Fix the cells by incubating in 4% paraformaldehyde in PBS for 10 minutes at room temperature.
5. Wash the cells twice with PBS.
6. Paraformaldehyde fixation is not stable. Excessively long incubations in aqueous buffers will reverse the cross-linking and should be avoided.
7. Permeabilize the fixed cells by incubating in 0.2% Triton X-100 or NP-40 in PBS for 2 minutes at room temperature. Some preparations may need as long as 15 minutes; check access of the antibody to the specimen for each antigen.
8. Rinse gently in PBS with four changes over 5 minutes.
9. Samples are now ready for the application of antibodies (see Indirect Detection Using Horseradish Peroxidase-Labeled Reagents and Indirect Detection Using Fluorochrome-Labeled Reagents).

TROUBLESHOOTING

Problem: Antigenicity of cell components is reduced
Solution: Fixation in protein cross-linking reagents such as paraformaldehyde preserves cell structure better than organic solvents but may reduce the antigenicity of some cell components. Any antibody that binds to a free amino group may be unable to recognize the antigen after paraformaldehyde treatment. If antibodies work well in other procedures but fail to work in cell staining, try titrating the levels of paraformaldehyde to lower concentrations. This may result in a lower level of cross-linking, but the cell architecture will be maintained and the antibody will have access to at least some of the antigen-binding domains.

Paraformaldehyde

Paraformaldehyde is highly toxic and may be fatal. It may be a carcinogen. It is readily absorbed through the skin and is extremely destructive to the skin, eyes, mucous membranes, and upper respiratory tract. Avoid breathing the dust or vapor. Wear appropriate gloves and safety glasses and use in a chemical fume hood. Keep away from heat, sparks, and open flame.

Triton X-100

Triton X-100 causes severe eye irritation and burns. It may be harmful by inhalation, ingestion, or skin absorption. Wear appropriate gloves and safety goggles.

Paraformaldehyde in PBS

Paraformaldehyde, EM grade
PBS (10X)
NaOH (1 M)
HCl (1 M)

For a 4% paraformaldehyde solution, add 4 g of EM grade paraformaldehyde to 50 mL of $H2O$. Add 1 mL of 1 M
NaOH and stir gently on a heating block at ~60°C until the paraformaldehyde is dissolved. Add 10 mL of 10X PBS and allow the mixture to cool to room temperature. Adjust the pH to 7.4 with 1 M HCl (~1 mL), then adjust the final volume to 100 mL with $H2O$. Filter the solution through a 0.45-µm membrane filter to remove any particulate matter. Make the paraformaldehyde solution fresh prior to use, or store in aliquots at –20°C for several months. Avoid repeated freeze/thawing.

Phosphate-buffered saline (PBS)

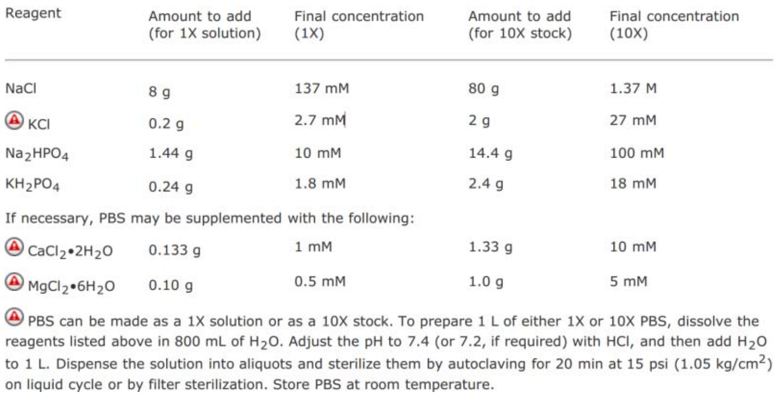

Reagent	Amount to add (for 1X solution)	Final concentration (1X)	Amount to add (for 10X stock)	Final concentration (10X)
NaCl	8 g	137 mM	80 g	1.37 M
⚠ KCl	0.2 g	2.7 mM	2 g	27 mM
Na_2HPO_4	1.44 g	10 mM	14.4 g	100 mM
KH_2PO_4	0.24 g	1.8 mM	2.4 g	18 mM
If necessary, PBS may be supplemented with the following:				
⚠ $CaCl_2 \cdot 2H_2O$	0.133 g	1 mM	1.33 g	10 mM
⚠ $MgCl_2 \cdot 6H_2O$	0.10 g	0.5 mM	1.0 g	5 mM

⚠ PBS can be made as a 1X solution or as a 10X stock. To prepare 1 L of either 1X or 10X PBS, dissolve the reagents listed above in 800 mL of H_2O. Adjust the pH to 7.4 (or 7.2, if required) with HCl, and then add H_2O to 1 L. Dispense the solution into aliquots and sterilize them by autoclaving for 20 min at 15 psi (1.05 kg/cm^2) on liquid cycle or by filter sterilization. Store PBS at room temperature.

Copyright © 2006 by Cold Spring Harbor Laboratory Press. Online ISSN: 1559-6095 Terms of Service All rights reserved. Anyone using the procedures outlined in these protocols does so at their own risk. Cold Spring Harbor Laboratory makes no representations or warranties with respect to the material set forth in these protocols and has no liability in connection with their use. All materials used in these protocols, but not limited to those highlighted with the Warning icon, may be considered hazardous and should be used with caution. For a full listing of cautions, click here.
All rights reserved. No part of these pages, either text or images, may be used for any reason other than personal use. Reproduction, modification, storage in a retrieval system or retransmission, in any form or by any means-electronic, mechanical, or otherwise-for reasons other than personal use is strictly prohibited without prior written permission.

References

1. TutorVista.com. Available at: http://images.tutorvista.com/cms/images/38/plasma-membrane.png.
2. Ladoux, B. & Nicolas, A. Physically based principles of cell adhesion mechanosensitivity in tissues. *Rep. Prog. Phys.* **75,** 116601 (2012).
3. Eberly College. Cell Structure and Function. *PennState Eberly Collage of Science* Available at: https://online.science.psu.edu/biol141_wc/node/7511.
4. Rogers, Kara. *The Cell (Biochemistry, Cells, and Life)*. (2011).
5. Tay, C. Y., Irvine, S. A., Boey, F. Y., Tan, L. P. & Venkatraman, S. Micro-/nano-engineered cellular responses for soft tissue engineering and biomedical applications. *Small* **7,** 1361–1378 (2011).
6. Liu, W. F. Mechanical regulation of cellular phenotype: implications for vascular tissue regeneration. *Cardiovasc. Res.* **95,** 215–222 (2012).
7. Lo, C.-M., Wang, H.-B., Dembo, M. & Wang, Y. Cell Movement Is Guided by the Rigidity of the Substrate. *Biophys. J.* **79,** 144–152 (2000).
8. Murphy, W. L., McDevitt, T. C. & Engler, A. J. Materials as stem cell regulators. *Nat. Mater.* **13,** 547–557 (2014).
9. Harris, A. K., Wild, P. & Stopak, D. Silicone rubber substrata: a new wrinkle in the study of cell locomotion. *Science* **208,** 177–179 (1980).
10. Schwarz, U. Soft matters in cell adhesion: rigidity sensing on soft elastic substrates. *Soft Matter* **3,** 263–266 (2007).
11. Dembo, M., Oliver, T., Ishihara, A. & Jacobson, K. Imaging the traction stresses exerted by locomoting cells with the elastic substratum method. *Biophys. J.* **70,** 2008–2022 (1996).
12. Dembo, M. & Wang, Y. L. Stresses at the cell-to-substrate interface during locomotion of fibroblasts. *Biophys. J.* **76,** 2307–2316 (1999).
13. Galbraith, C. G. & Sheetz, M. P. A micromachined device provides a new bend on fibroblast traction forces. *Proc. Natl. Acad. Sci.* **94,** 9114–9118 (1997).
14. Petronis, S., Gold, J. & Kasemo, B. Microfabricated force-sensitive elastic substrates for investigation of mechanical cell–substrate interactions. *J. Micromechanics Microengineering* **13,** 900 (2003).
15. Delanoë-Ayari, H. 4D Traction Force Microscopy Reveals Asymmetric Cortical Forces in Migrating *Dictyostelium* Cells. *Phys. Rev. Lett.* **105,** (2010).
16. Maruthamuthu, V., Sabass, B., Schwarz, U. S. & Gardel, M. L. Cell-ECM traction force modulates endogenous tension at cell-cell contacts. *Proc. Natl. Acad. Sci.* **108,** 4708–4713 (2011).
17. Fu, J. *et al.* Mechanical regulation of cell function with geometrically modulated elastomeric substrates. *Nat. Methods* **7,** 733–736 (2010).
18. Trepat, X. *et al.* Physical forces during collective cell migration. *Nat. Phys.* **5,** 426–430 (2009).
19. Wang, W., Wang, S., Liu, Q., Wu, J. & Tao, N. Mapping Single-Cell–Substrate Interactions by Surface Plasmon Resonance Microscopy. *Langmuir* **28,** 13373–13379 (2012).

20. Jaeger, A. A. *et al.* Microfabricated polymeric vessel mimetics for 3-D cancer cell culture. *Biomaterials* **34,** 8301–8313 (2013).
21. Kissinger, P. T. Biosensors—a perspective. *Biosens. Bioelectron.* **20,** 2512–2516 (2005).
22. Mendes, P. M. Cellular nanotechnology: making biological interfaces smarter. *Chem. Soc. Rev.* **42,** 9207 (2013).
23. Ivnitski, D., Abdel-Hamid, I., Atanasov, P. & Wilkins, E. Biosensors for detection of pathogenic bacteria. *Biosens. Bioelectron.* **14,** 599–624 (1999).
24. Thévenot, D. R., Toth, K., Durst, R. A. & Wilson, G. S. Electrochemical biosensors: recommended definitions and classification. *Biosens. Bioelectron.* **16,** 121–131 (2001).
25. Abadian, P. N., Kelley, C. P. & Goluch, E. D. Cellular Analysis and Detection Using Surface Plasmon Resonance Techniques. *Anal. Chem.* **86,** 2799–2812 (2014).
26. Fan, X. *et al.* Sensitive optical biosensors for unlabeled targets: A review. *Anal. Chim. Acta* **620,** 8–26 (2008).
27. Sepúlveda, B., Angelomé, P. C., Lechuga, L. M. & Liz-Marzán, L. M. LSPR-based nanobiosensors. *Nano Today* **4,** 244–251 (2009).
28. Fredriksson, H. *et al.* Hole-Mask Colloidal Lithography. *Adv. Mater.* **19,** 4297–4302 (2007).
29. Otte, M. A. *et al.* Improved Biosensing Capability with Novel Suspended Nanodisks. *J. Phys. Chem. C* **115,** 5344–5351 (2011).
30. Chung, T., Lee, S.-Y., Song, E. Y., Chun, H. & Lee, B. Plasmonic Nanostructures for Nano-Scale Bio-Sensing. *Sensors* **11,** 10907–10929 (2011).
31. Lu, X., Rycenga, M., Skrabalak, S. E., Wiley, B. & Xia, Y. Chemical Synthesis of Novel Plasmonic Nanoparticles. *Annu. Rev. Phys. Chem.* **60,** 167–192 (2009).
32. Willets, K. A. & Van Duyne, R. P. Localized Surface Plasmon Resonance Spectroscopy and Sensing. *Annu. Rev. Phys. Chem.* **58,** 267–297 (2007).
33. Unser, S., Bruzas, I., He, J. & Sagle, L. Localized Surface Plasmon Resonance Biosensing: Current Challenges and Approaches. *Sensors* **15,** 15684–15716 (2015).
34. Brolo, A. G. Plasmonics for future biosensors. *Nat. Photonics* **6,** 709–713 (2012).
35. McFarland, A. D. & Van Duyne, R. P. Single Silver Nanoparticles as Real-Time Optical Sensors with Zeptomole Sensitivity. *Nano Lett.* **3,** 1057–1062 (2003).
36. Myers, F. B. & Lee, L. P. Innovations in optical microfluidic technologies for point-of-care diagnostics. *Lab. Chip* **8,** 2015–2031 (2008).
37. Mayer, K. M. & Hafner, J. H. Localized Surface Plasmon Resonance Sensors. *Chem. Rev.* **111,** 3828–3857 (2011).
38. Otte, M. A. *et al.* Identification of the Optimal Spectral Region for Plasmonic and Nanoplasmonic Sensing. *ACS Nano* **4,** 349–357 (2010).
39. Haes, A. J. & Van Duyne, R. P. A Nanoscale Optical Biosensor: Sensitivity and Selectivity of an Approach Based on the Localized Surface Plasmon Resonance Spectroscopy of Triangular Silver Nanoparticles. *J. Am. Chem. Soc.* **124,** 10596–10604 (2002).
40. Mitchell, P. Microfluidics—downsizing large-scale biology. *Nat. Biotechnol.* **19,** 717–721 (2001).
41. Beebe, D. J., Mensing, G. A. & Walker, G. M. Physics and Applications of Microfluidics in Biology. *Annu. Rev. Biomed. Eng.* **4,** 261–286 (2002).
42. Tanyeri, M., Ranka, M., Sittipolkul, N. & Schroeder, C. M. A microfluidic-based hydrodynamic trap: design and implementation. *Lab. Chip* **11,** 1786–1794 (2011).

43. Sia, S. K. & Whitesides, G. M. Microfluidic devices fabricated in Poly(dimethylsiloxane) for biological studies. *ELECTROPHORESIS* **24,** 3563–3576 (2003).
44. Ariga, K. *et al.* Challenges and breakthroughs in recent research on self-assembly. *Sci. Technol. Adv. Mater.* **9,** 14109 (2008).
45. Gates, B. D. *et al.* New Approaches to Nanofabrication: Molding, Printing, and Other Techniques. *Chem. Rev.* **105,** 1171–1196 (2005).
46. Mailly, D. Nanofabrication techniques. *Eur. Phys. J. Spec. Top.* **172,** 333–342 (2009).
47. Benjamin Fry, K. K. *Nanotechnology-Enabled Sensors*. (Springer Science & Business Media, 2008).
48. Ito, T. & Okazaki, S. Pushing the limits of lithography. *Nature* **406,** 1027–1031 (2000).
49. Otte, M. A. *et al.* Tailored Height Gradients in Vertical Nanowire Arrays via Mechanical and Electronic Modulation of Metal-Assisted Chemical Etching. *Small* (2015). doi:10.1002/smll.201500175
50. Sato, H., Houshi, Y. & Shoji, S. Three-dimensional micro-structures consisting of high aspect ratio inclined micro-pillars fabricated by simple photolithography. *Microsyst. Technol.* **10,** 440–443 (2004).
51. Fujita, J. *et al.* Growth of three-dimensional nano-structures using FIB-CVD and its mechanical properties. *Nucl. Instrum. Methods Phys. Res. Sect. B Beam Interact. Mater. At.* **206,** 472–477 (2003).
52. Westwater, J. Growth of silicon nanowires via gold/silane vapor–liquid–solid reaction. *J. Vac. Sci. Technol. B Microelectron. Nanometer Struct.* **15,** 554 (1997).
53. Schubert, L. *et al.* Silicon nanowhiskers grown on 〈111〉 Si substrates by molecular-beam epitaxy. *Appl. Phys. Lett.* **84,** 4968 (2004).
54. Bauer, J. *et al.* Electrical properties of nominally undoped silicon nanowires grown by molecular-beam epitaxy. *Appl. Phys. Lett.* **90,** 12105 (2007).
55. Liu, J. L., Cai, S. J., Jin, G. L., Thomas, S. G. & Wang, K. L. Growth of Si whiskers on Au/Si(1 1 1) substrate by gas source molecular beam epitaxy (MBE). *J. Cryst. Growth* **200,** 106–111 (1999).
56. Yang, Y.-H., Wu, S.-J., Chiu, H.-S., Lin, P.-I. & Chen, Y.-T. Catalytic Growth of Silicon Nanowires Assisted by Laser Ablation. *J. Phys. Chem. B* **108,** 846–852 (2004).
57. Tien, L. C., Pearton, S. J., Norton, D. P. & Ren, F. Synthesis and microstructure of vertically aligned ZnO nanowires grown by high-pressure-assisted pulsed-laser deposition. *J. Mater. Sci.* **43,** 6925–6932 (2008).
58. Umar, A. & Hahn, Y. B. Aligned hexagonal coaxial-shaped ZnO nanocolumns on steel alloy by thermal evaporation. *Appl. Phys. Lett.* **88,** 173120 (2006).
59. Chang, Y.-F., Chou, Q.-R., Lin, J.-Y. & Lee, C.-H. Fabrication of high-aspect-ratio silicon nanopillar arrays with the conventional reactive ion etching technique. *Appl. Phys. A* **86,** 193–196 (2006).
60. Zhang, J., Li, Y., Zhang, X. & Yang, B. Colloidal Self-Assembly Meets Nanofabrication: From Two-Dimensional Colloidal Crystals to Nanostructure Arrays. *Adv. Mater.* **22,** 4249–4269 (2010).
61. Geyer, N. *et al.* Model for the mass transport during metal-assisted chemical etching with contiguous metal films as catalysts. *J Phys Chem C* (2012). doi:10.1021/jp3034227
62. Kugel, V. & Ji, H.-F. Nanopillars for Sensing. *J. Nanosci. Nanotechnol.* **14,** 6469–6477 (2014).

63. Chang, Y.-F., Chou, Q.-R., Lin, J.-Y. & Lee, C.-H. Fabrication of high-aspect-ratio silicon nanopillar arrays with the conventional reactive ion etching technique. *Appl. Phys. A* **86,** 193–196 (2006).
64. Otte, M. A. *et al.* Tailored Height Gradients in Vertical Nanowire Arrays via Mechanical and Electronic Modulation of Metal-Assisted Chemical Etching. *Small* n/a-n/a (2015). doi:10.1002/smll.201500175
65. Geyer, N. *et al.* Model for the Mass Transport during Metal-Assisted Chemical Etching with Contiguous Metal Films As Catalysts. *J. Phys. Chem. C* **116,** 13446–13451 (2012).
66. Li, L. *et al.* Polystyrene sphere-assisted one-dimensional nanostructure arrays: synthesis and applications. *J. Mater. Chem.* **21,** 40–56 (2010).
67. Kosiorek, A., Kandulski, W., Chudzinski, P., Kempa, K. & Giersig, M. Shadow Nanosphere Lithography: Simulation and Experiment. *Nano Lett.* **4,** 1359–1363 (2004).
68. Lipomi, D. J. *et al.* Fabrication and Replication of Arrays of Single- or Multicomponent Nanostructures by Replica Molding and Mechanical Sectioning. *ACS Nano* **4,** 4017–4026 (2010).
69. Solis-Tinoco, V., Sepulveda, B. & Lechuga, L. M. Novel nanoplasmonic biosensor integrated in a microfluidic channel. in **9519,** 95190T–95190T–9 (2015).
70. Huang, Z., Geyer, N., Werner, P., de Boor, J. & Gösele, U. Metal-Assisted Chemical Etching of Silicon: A Review. *Adv. Mater.* **23,** 285–308 (2011).
71. Jiang, P. & McFarland, M. J. Large-Scale Fabrication of Wafer-Size Colloidal Crystals, Macroporous Polymers and Nanocomposites by Spin-Coating. *J. Am. Chem. Soc.* **126,** 13778–13786 (2004).
72. Hayward, R. C., Saville, D. A. & Aksay, I. A. Electrophoretic assembly of colloidal crystals with optically tunable micropatterns. *Nature* **404,** 56–59 (2000).
73. Duffel, B. van, Ras, R. H. A., Schryver, F. C. D. & Schoonheydt, R. A. Langmuir–Blodgett deposition and optical diffraction of two-dimensional opal. *J. Mater. Chem.* **11,** 3333–3336 (2001).
74. Retsch, M. *et al.* Fabrication of Large-Area, Transferable Colloidal Monolayers Utilizing Self-Assembly at the Air/Water Interface. *Macromol. Chem. Phys.* **210,** 230–241 (2009).
75. Kosiorek, A., Kandulski, W., Glaczynska, H. & Giersig, M. Fabrication of Nanoscale Rings, Dots, and Rods by Combining Shadow Nanosphere Lithography and Annealed Polystyrene Nanosphere Masks. *Small* **1,** 439–444 (2005).
76. Zhou, C. M. & Gall, D. Branched Ta nanocolumns grown by glancing angle deposition. *Appl. Phys. Lett.* **88,** 203117 (2006).
77. Li, Y., Sasaki, T., Shimizu, Y. & Koshizaki, N. Hexagonal-Close-Packed, Hierarchical Amorphous TiO2 Nanocolumn Arrays: Transferability, Enhanced Photocatalytic Activity, and Superamphiphilicity without UV Irradiation. *J. Am. Chem. Soc.* **130,** 14755–14762 (2008).
78. Jansen, H., Gardeniers, H., Boer, M. de, Elwenspoek, M. & Fluitman, J. A survey on the reactive ion etching of silicon in microtechnology. *J. Micromechanics Microengineering* **6,** 14 (1996).
79. Bondur, J. A. Dry process technology (reactive ion etching). *J. Vac. Sci. Technol.* **13,** 1023 (1976).
80. Fu, Y. Q. *et al.* Deep reactive ion etching as a tool for nanostructure fabrication. *J. Vac. Sci. Technol. B Microelectron. Nanometer Struct.* **27,** 1520 (2009).

81. Ogawa, R., Ogawa, H., Oki, A., Hashioka, S. & Horiike, Y. Fabrication of nano-pillar chips by a plasma etching technique for fast DNA separation. *Thin Solid Films* **515,** 5167–5171 (2007).
82. Dai, Z. R., Pan, Z. W. & Wang, Z. L. Novel Nanostructures of Functional Oxides Synthesized by Thermal Evaporation. *Adv. Funct. Mater.* **13,** 9–24 (2003).
83. Chartier, C., Bastide, S. & Lévy-Clément, C. Metal-assisted chemical etching of silicon in HF–H2O2. *Electrochimica Acta* **53,** 5509–5516 (2008).
84. Huang, Z., Geyer, N., Werner, P., de Boor, J. & Gösele, U. Metal-Assisted Chemical Etching of Silicon: A Review. *Adv. Mater.* **23,** 285–308 (2011).
85. Geyer, N. *et al.* Model for the Mass Transport during Metal-Assisted Chemical Etching with Contiguous Metal Films As Catalysts. *J. Phys. Chem. C* **116,** 13446–13451 (2012).
86. Gates, B. D., Xu, Q., Love, J. C., Wolfe, D. B. & Whitesides, G. M. Unconventional Nanofabrication. *Annu. Rev. Mater. Res.* **34,** 339–372 (2004).
87. Qin, D., Xia, Y. & Whitesides, G. M. Soft lithography for micro- and nanoscale patterning. *Nat. Protoc.* **5,** 491–502 (2010).
88. Colburn, M. *et al.* Step and flash imprint lithography: a new approach to high-resolution patterning</title> in (ed. Vladimirsky, Y.) 379–389 (1999). doi:10.1117/12.351155
89. Xia, Y. & Whitesides, G. M. Soft Lithography. *Annu. Rev. Mater. Sci.* **28,** 153–184 (1998).
90. Zhao, X.-M., Xia, Y. & Whitesides, G. M. Fabrication of three-dimensional micro-structures: Microtransfer molding. *Adv. Mater.* **8,** 837–840 (1996).
91. Kim, E., Xia, Y. & Whitesides, G. M. Polymer microstructures formed by moulding in capillaries. *Nature* **376,** 581–584 (1995).
92. Chou, S. Y., Krauss, P. R. & Renstrom, P. J. Imprint of sub-25 nm vias and trenches in polymers. *Appl. Phys. Lett.* **67,** 3114 (1995).
93. Chou, S. Y. Nanoimprint lithography. *J. Vac. Sci. Technol. B Microelectron. Nanometer Struct.* **14,** 4129 (1996).
94. Chou, S. Y. Sub-10 nm imprint lithography and applications. *J. Vac. Sci. Technol. B Microelectron. Nanometer Struct.* **15,** 2897 (1997).
95. King, E., Xia, Y., Zhao, X.-M. & Whitesides, G. M. Solvent-assisted microcontact molding: A convenient method for fabricating three-dimensional structures on surfaces of polymers. *Adv. Mater.* **9,** 651–654 (1997).
96. Tan, J. L. *et al.* Cells lying on a bed of microneedles: An approach to isolate mechanical force. *Proc. Natl. Acad. Sci.* **100,** 1484–1489 (2003).
97. Balaban, N. Q. *et al.* Force and focal adhesion assembly: a close relationship studied using elastic micropatterned substrates. *Nat. Cell Biol.* **3,** 466–472 (2001).
98. Ghibaudo, M. *et al.* Traction forces and rigidity sensing regulate cell functions. *Soft Matter* **4,** 1836–1843 (2008).
99. Digabel, J. le, Ghibaudo, M., Trichet, L., Richert, A. & Ladoux, B. Microfabricated substrates as a tool to study cell mechanotransduction. *Med. Biol. Eng. Comput.* **48,** 965–976 (2010).
100. Yang, M. T., Fu, J., Wang, Y.-K., Desai, R. A. & Chen, C. S. Assaying stem cell mechanobiology on microfabricated elastomeric substrates with geometrically modulated rigidity. *Nat. Protoc.* **6,** 187–213 (2011).
101. Gin, A., Movaghar, B., Razeghi, M. & Brown, G. J. Infrared detection from GaInAs/InP nanopillar arrays. *Nanotechnology* **16,** 1814–1820 (2005).

102. Bie, L.-J., Yan, X.-N., Yin, J., Duan, Y.-Q. & Yuan, Z.-H. Nanopillar ZnO gas sensor for hydrogen and ethanol. *Sens. Actuators B Chem.* **126,** 604–608 (2007).

103. Anandan, V., Yang, X., Kim, E., Rao, Y. L. & Zhang, G. Role of reaction kinetics and mass transport in glucose sensing with nanopillar array electrodes. *J. Biol. Eng.* **1,** 5 (2007).

104. Wang, C. *et al.* Highly sensitive thermal detection of thrombin using aptamer-functionalized phase change nanoparticles. *Biosens. Bioelectron.* **26,** 437–443 (2010).

105. Suzuki, Y. & Yokoyama, K. Construction of a more sensitive fluorescence sensing material for the detection of vascular endothelial growth factor, a biomarker for angiogenesis, prepared by combining a fluorescent peptide and a nanopillar substrate. *Biosens. Bioelectron.* **26,** 3696–3699 (2011).

106. Holgado, M. *et al.* Label-free biosensing by means of periodic lattices of high aspect ratio SU-8 nano-pillars. *Biosens. Bioelectron.* **25,** 2553–2558 (2010).

107. Wasisto, H. S. *et al.* Femtogram Mass Measurement of Airborne Engineered Nanoparticles using Silicon Nanopillar Resonators. *Procedia Eng.* **47,** 289–292 (2012).

108. Anandan, V., Rao, Y. L. & Zhang, G. Nanopillar array structures for enhancing biosensing performance. *Int. J. Nanomedicine* **1,** 73–79 (2006).

109. Otte, M. A. *et al.* Improved Biosensing Capability with Novel Suspended Nanodisks. *J. Phys. Chem. C* **115,** 5344–5351 (2011).

110. Dmitriev, A. *et al.* Enhanced Nanoplasmonic Optical Sensors with Reduced Substrate Effect. *Nano Lett.* **8,** 3893–3898 (2008).

111. Knoben, W., Brongersma, S. H. & Crego-Calama, M. Plasmonic Au islands on polymer nanopillars. *Nanotechnology* **22,** 295303 (2011).

112. Shen, Y. *et al.* Plasmonic gold mushroom arrays with refractive index sensing figures of merit approaching the theoretical limit. *Nat. Commun.* **4,** (2013).

113. Saito, M. *et al.* Novel Gold-Capped Nanopillars Imprinted on a Polymer Film for Highly Sensitive Plasmonic Biosensing. *Anal. Chem.* **84,** 5494–5500 (2012).

114. Yang, S.-C. *et al.* Synthesis of multifunctional plasmonic nanopillar array using soft thermal nanoimprint lithography for highly sensitive refractive index sensing. *Nanoscale* **7,** 5760–5766 (2015).

115. Zheng, H. *et al.* Morphological Design of Gold Nanopillar Arrays and Their Optical Properties. *J. Phys. Chem. C* (2015). doi:10.1021/acs.jpcc.5b09188

116. Si, G., Jiang, X., Lv, J., Gu, Q. & Wang, F. Fabrication and characterization of well-aligned plasmonic nanopillars with ultrasmall separations. *Nanoscale Res. Lett.* **9,** 299 (2014).

117. Wang, K. & Crozier, K. B. Plasmonic Trapping with a Gold Nanopillar. *ChemPhysChem* **13,** 2639–2648 (2012).

118. Çetin, A. E. *et al.* Monopole antenna arrays for optical trapping, spectroscopy, and sensing. *Appl. Phys. Lett.* **98,** 111110 (2011).

119. Kubo, W. & Fujikawa, S. Au double nanopillars with nanogap for plasmonic sensor. *Nano Lett.* **11,** 8–15 (2011).

120. Schmidt, M. S., Hübner, J. & Boisen, A. Large Area Fabrication of Leaning Silicon Nanopillars for Surface Enhanced Raman Spectroscopy. *Adv. Mater.* **24,** OP11-OP18 (2012).

121. Caldwell, J. D. *et al.* Plasmonic Nanopillar Arrays for Large-Area, High-Enhancement Surface-Enhanced Raman Scattering Sensors. *ACS Nano* **5,** 4046–4055 (2011).

122. Kaiyu Wu, T. R. Plasmon resonances of Ag capped Si nanopillars fabricated using mask-less lithography. *Opt. Express* **23,** 12965–12978 (2015).
123. Estevez, M.-C., Otte, M. A., Sepulveda, B. & Lechuga, L. M. Trends and challenges of refractometric nanoplasmonic biosensors: A review. *Anal. Chim. Acta* **806,** 55–73 (2014).
124. Yasui, T. *et al.* Electroosmotic Flow in Microchannels with Nanostructures. *ACS Nano* **5,** 7775–7780 (2011).
125. Wang, T. *et al.* Anisotropic Janus Si nanopillar arrays as a microfluidic one-way valve for gas–liquid separation. *Nanoscale* **6,** 3846–3853 (2014).
126. Gina S, F. & T. Chiu, D. Disposable microfluidic devices: fabrication, function, and application. *BioTecniques* **38,** (2005).
127. Gonzalez, C., Collins, S. D. & Smith, R. L. Fluidic interconnects for modular assembly of chemical microsystems. in , *1997 International Conference on Solid State Sensors and Actuators, 1997. TRANSDUCERS '97 Chicago* **1,** 527–530 vol.1 (1997).
128. Zhang, B., Dong, Q., Korman, C. E., Li, Z. & Zaghloul, M. E. Flexible packaging of solid-state integrated circuit chips with elastomeric microfluidics. *Sci. Rep.* **3,** (2013).
129. King, D. E. Oxidation of gold by ultraviolet light and ozone at 25 °C. *J. Vac. Sci. Technol. A* **13,** 1247–1253 (1995).
130. Chartier, C., Bastide, S. & Lévy-Clément, C. Metal-assisted chemical etching of silicon in HF–H2O2. *Electrochimica Acta* **53,** 5509–5516 (2008).
131. Hui, C. Y., Jagota, A., Lin, Y. Y. & Kramer, E. J. Constraints on Microcontact Printing Imposed by Stamp Deformation. *Langmuir* **18,** 1394–1407 (2002).
132. Sharp, K. G., Blackman, G. S., Glassmaker, N. J., Jagota, A. & Hui, C.-Y. Effect of Stamp Deformation on the Quality of Microcontact Printing: Theory and Experiment. *Langmuir* **20,** 6430–6438 (2004).
133. Levental, I., Georges, P. C. & Janmey, P. A. Soft biological materials and their impact on cell function. *Soft Matter* **3,** 299–306 (2007).
134. Eddings, M. A., Johnson, M. A. & Gale, B. K. Determining the optimal PDMS–PDMS bonding technique for microfluidic devices. *J. Micromechanics Microengineering* **18,** 67001 (2008).
135. Gajasinghe, R. W. R. L. *et al.* Experimental study of PDMS bonding to various substrates for monolithic microfluidic applications. *J. Micromechanics Microengineering* **24,** 75010 (2014).
136. Sullivan, D. M. *Electromagnetic Simulation Using the FDTD Method*. (Wiley-IEEE Press, 2000).
137. Soler, M., Estevez, M.-C., Villar-Vazquez, R., Casal, J. I. & Lechuga, L. M. Label-free nanoplasmonic sensing of tumor-associate autoantibodies for early diagnosis of colorectal cancer. *Anal. Chim. Acta* **930,** 31–38 (2016).
138. Trichet, L. *et al.* Evidence of a large-scale mechanosensing mechanism for cellular adaptation to substrate stiffness. *Proc. Natl. Acad. Sci. U. S. A.* **109,** 6933–6938 (2012).
139. Noireaux, V. *et al.* Growing an Actin Gel on Spherical Surfaces. *Biophys. J.* **78,** 1643–1654 (2000).
140. Mitrossilis, D. *et al.* Single-cell response to stiffness exhibits muscle-like behavior. *Proc. Natl. Acad. Sci. U. S. A.* **106,** 18243–18248 (2009).
141. Giardini, P. A., Fletcher, D. A. & Theriot, J. A. Compression forces generated by actin comet tails on lipid vesicles. *Proc. Natl. Acad. Sci.* **100,** 6493–6498 (2003).

142. Dembo, M. & Wang, Y.-L. Stresses at the Cell-to-Substrate Interface during Locomotion of Fibroblasts. *Biophys. J.* **76,** 2307–2316 (1999).
143. Alvarez, R. *et al.* A Novel Regulatory Pathway of Brown Fat Thermogenesis RETINOIC ACID IS A TRANSCRIPTIONAL ACTIVATOR OF THE MITOCHONDRIAL UNCOUPLING PROTEIN GENE. *J. Biol. Chem.* **270,** 5666–5673 (1995).
144. Whittle, A. J. *et al.* BMP8B Increases Brown Adipose Tissue Thermogenesis through Both Central and Peripheral Actions. *Cell* **149,** 871–885 (2012).
145. Hirsch, J. & Gallian, E. Methods for the determination of adipose cell size in man and animals. *J. Lipid Res.* **9,** 110–119 (1968).
146. Rudolf Žitný, Kulvajtová, M. & Tereza Voňavková. Uniaxial Tensile Test of Perivascular Adipose Tissue. *Bulletin of Applied Mechanics* **10(36),** 11–14 (2014).
147. Leff, D. V., Brandt, L. & Heath, J. R. Synthesis and Characterization of Hydrophobic, Organically-Soluble Gold Nanocrystals Functionalized with Primary Amines. *Langmuir* **12,** 4723–4730 (1996).
148. Ooka, A. A., Kuhar, K. A., Cho, N. & Garrell, R. L. Surface interactions of a homologous series of alpha,omega-amino acids on colloidal silver and gold. *Biospectroscopy* **5,** 9–17 (1999).
149. Haddada, M. B. *et al.* Optimizing the immobilization of gold nanoparticles on functionalized silicon surfaces: amine- vs thiol-terminated silane. *Gold Bull.* **46,** 335–341 (2013).
150. Biosensors elaborated on gold nanoparticles, a PM-IRRAS characterisation of the IgG binding efficiency. Available at: http://www.sciencedirect.com/science/article/pii/S0039914011001597. (Accessed: 18th September 2016)
151. M.T, Y., N.J, S. & C.S, C. Geometric Considerations of Micro- to Nanoscale Elastomeric Post Arrays to Study Cellular Traction Forces. *Adv. Mater.* 3119–3123 (2007).
152. Alberts, B. *et al. Essential Cell Biology, Fourth Edition*. (Garland Science, 2013).
153. Dalby, M. J. Cellular response to low adhesion nanotopographies. *Int. J. Nanomedicine* **2,** 373–381 (2007).